

11-7-2011

# Fast start of oscillations in a short-pulse relativistic magnetron driven by a transparent cathode.

Sarita Prasad

Follow this and additional works at: [https://digitalrepository.unm.edu/ece\\_etds](https://digitalrepository.unm.edu/ece_etds)

---

## Recommended Citation

Prasad, Sarita. "Fast start of oscillations in a short-pulse relativistic magnetron driven by a transparent cathode.." (2011).  
[https://digitalrepository.unm.edu/ece\\_etds/209](https://digitalrepository.unm.edu/ece_etds/209)

This Dissertation is brought to you for free and open access by the Engineering ETDs at UNM Digital Repository. It has been accepted for inclusion in Electrical and Computer Engineering ETDs by an authorized administrator of UNM Digital Repository. For more information, please contact [disc@unm.edu](mailto:disc@unm.edu).

**Sarita Prasad**

*Candidate*

**ELECTRICAL AND COMPUTER ENGINEERING**

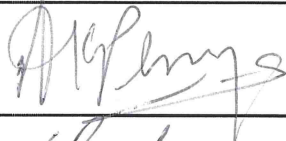
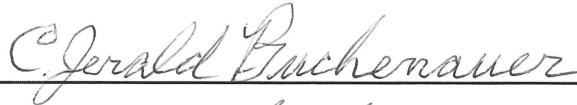
*Department*

This dissertation is approved, and it is acceptable in quality and form for publication:

*Approved by the Dissertation Committee:*



, Chairperson



**FAST START OF OSCILLATIONS IN A SHORT-PULSE  
RELATIVISTIC MAGNETRON DRIVEN BY A  
TRANSPARENT CATHODE**

**BY**

**SARITA PRASAD**

B.S., Electrical Engineering, Nagaoka University of Technology,  
Nagaoka City, Niigata, Japan, 1999

M.S., Electrical Engineering, Nagaoka University of Technology,  
Nagaoka City, Niigata, Japan, 2003

DISSERTATION

Submitted in Partial Fulfillment of the  
Requirements for the Degree of

**Doctor of Philosophy  
Engineering**

The University of New Mexico  
Albuquerque, New Mexico

**December, 2010**

## **DEDICATION**

I dedicate this dissertation to the Universe Divine.

## ACKNOWLEDGMENTS

First and foremost I would like to extend my sincere gratitude to my committee chair and advisor, Prof. Edl Schamiloglu without whose support over the past 7 years, I could not have realized the biggest dream of my life. His guidance and professional style will remain with me as I continue my career.

I gratefully acknowledge the assistance of my dissertation committee members: Prof. Mikhail Fuks, Prof. C. Jerald Buchenauer, Prof. Christos Christodoulou, Prof. Mark Gilmore, and Prof. Anil Prinja. The transparent cathode that was investigated in this dissertation and finally received its patent was Prof. Fuks' ingenious invention. I sincerely thank Prof. Fuks for the time and effort he dedicated in educating me on the subject of relativistic magnetrons. I am greatly indebted to Prof. Buchenauer (one of my best friends, my counselor, and my "guru" in the experimental world) for his patience and the many hours he spent help me prepare for the experiments. I owe my success in my experiments to him.

I would also like to extend my sincere gratitude to the great Engineer Kenneth Prestwich whose in-depth knowledge on particle beam accelerators helped me design a very efficient, low inductance vacuum chamber that worked without failure the first time.

I would like to give my hearty thanks to Ralph Lee Terry our building manager and Frank Mercer from the computer support group for all their help and support.

To my work colleagues Ralph Kelly, Melcoy Pablo and Marvin Roybal, thank you for all your help and hard work in helping me prepare for the experiments.

I would like thank Prof. Weihua Jiang of the Nagaoka University of Technology my Master's thesis advisor who recommended me to for my doctoral studies to Prof. Edl Schamiloglu.

To my Mum, Sunita Prasad, my brother, Anand Raj and my cat, Whiskey, many thanks for your moral support and encouragement.

And finally to my colleague and my sweetheart, Chris Leach, I thank you for helping me get through my writer's block, and your love and support.

**FAST START OF OSCILLATIONS IN A SHORT-PULSE  
RELATIVISTIC MAGNETRON DRIVEN BY A  
TRANSPARENT CATHODE**

**BY**

**SARITA PRASAD**

ABSTRACT OF DISSERTATION

Submitted in Partial Fulfillment of the  
Requirements for the Degree of

**Doctor of Philosophy**

**Engineering**

The University of New Mexico  
Albuquerque, New Mexico

**December, 2010**

**Fast Start of Oscillations in a Short-Pulse Relativistic Magnetron Driven by a  
Transparent Cathode**

by

**Sarita Prasad**

**B.S., Electrical Engineering, Nagaoka University of Technology, Nagaoka City,  
Niigata, Japan, 1999**

**M.S., Electrical Engineering, Nagaoka University of Technology, Nagaoka City,  
Niigata, Japan, 2003**

**Ph.D., Engineering, University of New Mexico, 2010**

**ABSTRACT**

The magnetron has been a major component of radar systems since its introduction in World War II. The newer radar techniques require high peak power (GW) and short microwave pulses (few ns). To serve as a microwave source for short-pulse applications it is imperative that the magnetron needs to have both fast start and fast rate of build-up of oscillations. Both of these factors are contingent on the cathode geometry.

The transparent cathode was invented at the University of New Mexico in an endeavor to improve the start time and increase the rate of build-up of oscillations in short-pulse relativistic magnetrons. The construction of the transparent cathode involves the removal of longitudinal strips of material from a hollow cathode. The resultant geometry has manifold advantages the first and the foremost of which is that it makes the cathode transparent to  $E_0$ , thereby greatly increasing its amplitude where electrons are emitted. Hence one would expect faster rate of build-up of oscillations. Secondly, this geometry simultaneously gives rise to several different forms of priming: cathode priming, electrostatic priming and magnetic priming. The number of cathode strips is chosen so that it would excite a particular mode of interest (e.g. 6 strips would favor the formation of 6 spokes). The cathode strips may be oriented azimuthally in a manner that the electron bunches from the cathode strips would be released into the favorable phase



of the mode of interest where efficient exchange of energy between the electrons and the RF fields could take place.

The highlights of this dissertation are proof-of-concept computer simulations demonstrating the benefits of the transparent cathode in an A6 magnetron driven by a transparent cathode that have validated the simulations.

## TABLE OF CONTENTS

<b>DEDICATION.....</b>	<b>iii</b>
<b>ACKNOWLEDGEMENT.....</b>	<b>iv</b>
<b>ABSTRACT.....</b>	<b>vii</b>
<b>TABLE OF CONTENTS .....</b>	<b>ix</b>
<b>LIST OF FIGURES .....</b>	<b>xiv</b>
<b>LIST OF FIGURES .....</b>	<b>xxi</b>
<b>CHAPTER 1 INTRODUCTION.....</b>	<b>1</b>
1-1 Historical Background.....	1
1-2 Modern Sources for Radar and Communications Systems .....	2
1-2-1 Short-Pulse Radars .....	2
1-2-1 High Peak Power Sources .....	3
1-3 Basic Principle of Operation and Start of Oscillations.....	3
1-3-1 Basic Principle of Operation .....	3
1-3-2 Start of Oscillations.....	5
1-4 Concept of Priming.....	6
1-5 Work Conducted at University of Michigan to Improve Start of Oscillations.....	7
1-5-1 UM Cathode Priming .....	7
1-5-2 UM Magnetic Priming .....	8
1-5-3 UM RF Priming.....	8
1-6 Efforts Undertaken at UNM to Improve Start Conditions in Magnetrons .....	10
1-7 The Air Force Research Laboratory (AFRL) Shaped Cathode .....	11

1-8 Scope of Dissertation and Chapter Organization .....	12
<b>CHAPTER 2 Theoretical Considerations.....</b>	<b>14</b>
2-1 Principles of Magnetron Operation .....	14
2-2 General Properties of Periodic Structures .....	16
2-3 Motion and Bunching of Electrons in RF fields of a Synchronous Wave .....	18
2-4 The RF Field Solutions.....	19
2-5 Growth of Oscillations.....	22
2-6 The Transparent Cathode.....	25
2-6-1 Rate of Buildup of Oscillations.....	26
2-6-2 Cathode Priming in a Transparent Cathode .....	27
2-6-3 Magnetic Priming in a Transparent Cathode.....	29
2-6-4 Electrostatic Priming in a Transparent Cathode.....	32
2-6-5 Other Merits of the Transparent Cathode.....	33
2-7 Efficiency Estimate of a Magnetron.....	35
<b>CHAPTER 3 Simulation Results.....</b>	<b>36</b>
3-1 The A6 Magnetron.....	36
3-2 Endcaps.....	38
3-3 The RF Field Configuration in the A6 Magnetron .....	38
3-4 A6 Magnetron Dispersion Characteristics.....	40
3-5 Description of MAGIC and Simulation Setup .....	43
3-6 Comparison of the Solid Cathode and the Transparent Cathode for Palevsky's A6 Magnetron Setup.....	45
3-7 Effect of voltage Rise Time on Magnetron Output Characteristics .....	48

3-8 Heuristic Explanations for the Behaviour Depicted by the Transparent Cathode	51
3-8-1 Startup Phase	52
3-8-2 Oscillatory Phase	53
3-9 Simulations with the SINUS-6 Voltage Waveform	54
3-10 Optimization of Microwave Radial Extraction	57
<b>CHAPTER 4 Experimental Setup</b>	<b>58</b>
4-1-1 Description of SINUS-6 Electron Beam Accelerator	58
4-1-2 Modifications Made to the SINUS-6	60
4-1-3 The Transmission Line	60
4-1-4 Pulsed Magnetic Field Producing System	60
4-1-5 Vacuum Chamber	61
4-1-6 Load Diagnostics	61
4-1-7 SINUS-6 Control System	63
4-1-8 Pulse stretcher circuit	65
4-2-1 Requirements on the Coils	66
4-2-2 Helmholtz Coils	66
4-2-3 Basic Parameter Selection	67
4-2-4 Coil Fabrication Procedure	69
4-2-5 Pulsed Magnetic Circuit	72
4-3-1 Vacuum Chamber and the Oil-Vacuum Interface	75
4-3-2 The Breakdown Process of an Insulator	75
4-3-3 The 45° Insulator	76
4-3-4 Design of Vacuum Chamber	82
4-4 Diagnostics	88

4-4-1 Voltage Diagnostic: Capacitive Divider Probe Concept of Operation .....	88
4-4-2 Calibration Procedure.....	89
4-4-3 Current Diagnostic: Rogowski Coil .....	92
4-4-4 Concept of Operation .....	92
4-4-5 Construction .....	94
4-4-6 Calibration Procedure.....	97
4-4-7 Directional Coupler for Microwave Power Measurements.....	99
4-4-8 Principle of Operation of the Loop Coupler.....	99
4-4-9 WR 229 Dual Monitor Directional Coupler.....	100
4-4-10 Microwave Frequency.....	101
<b>CHAPTER 5 Experimental Results .....</b>	<b>102</b>
5-1 Experimental Setup and Procedure.....	102
5-2 Experimental Results .....	106
5-3 Supplementary MAGIC Simulations.....	112
<b>CHAPTER 6 Conclusions .....</b>	<b>116</b>
6-1 Conclusions .....	116
6-2 Recommendations for Future Work .....	118
<b>APPENDIX 1 Design of Pulsed Magnetic Coils .....</b>	<b>119</b>
A1-1 Forces Between Coils .....	119
A1-2 Temperature Rise in Coil, $\Delta T_{\max}$ .....	120

<b>APPENDIX 2 List of Formulas for Calculating Coil Parameters.....</b>	<b>121</b>
A2-1 Self Inductance .....	121
A2-2 Mutual Inductance .....	123
A2-3 Total Inductance .....	123
<b>APPENDIX 3 Time -Frequency Analysis of Experimental Data .....</b>	<b>125</b>
<b>APPENDIX 4 Calibration Data.....</b>	<b>127</b>
A4-1 Calibration Data for the Directional Coupler .....	127
A4-2 Calibration Data for the RG 213 Cables.....	128
<b>REFERENCES.....</b>	<b>129</b>

## LIST OF FIGURES

### CHAPTER 1

Figure 1-1 Direction of electric and magnetic fields in a crossed-field device of cylindrical geometry. ....	3
Figure 1-2 General features of magnetron operation domain .....	5
Figure 1-3 Elementary interaction space concepts in a planar magnetron [5]. Here the applied axial B-field points into the page. ....	7
Figure 1-4 Schematic of a Cathode with discrete emission region for cathode priming [20]. ....	9
Figure 1-5 Magnets arranged around the azimuth to create prebunching of electrons for magnetic priming [22]. ....	10
Figure 1-6 Photograph of a graphite transparent cathode .....	10
Figure 1-7 Magnetron with shaped cathode.....	12

### CHAPTER 2

Figure 2-1 6-cavity magnetron geometry. ....	14
Figure 2-2 RF electric field distribution of the $\pi$ -mode in the interaction space.....	18
Figure 2-3 (Left) Photograph of a transparent cathode made of graphite, (right) cathode strips perpendicular to the direction of $E_0$ . ....	25

Figure 2-4 Dependence of the azimuthal electric field of the synchronous wave on radial position for a transparent cathode versus a solid cathode. Here $r_a$ , $r_c$ and $\Delta$ are anode radius, cathode radius and the electron hub height, respectively.....	26
Figure 2-5 (Left) Solid ring of electrons around the solid cathode. (Right) Electron prebunching in the transparent cathode.. .....	27
Figure 2-6 Magnetic field $B_\theta$ resulting from the current through each strip. ....	29
Figure 2-7 Magnetic flux distribution as a result of axial current through each cathode strip. ....	30
Figure 2-8 Electric field enhancement near cathode strips.....	32
Figure 2-9 Electric field lines for a planar magnetron with solid cathode.....	33
Figure 2-10 Plasma flow in magnetron with solid cathode (left) and transparent cathode (right). ....	35

### CHAPTER 3

Figure 3-1 The A6 magnetron geometry in the $r-\theta$ plane. ....	37
Figure 3-2 The A6 magnetron geometry in the $r-z$ plane taken at the azimuthal center of the cavity.. .....	37
Figure 3-3 The A6 magnetron geometry in the $r-z$ plane taken at the azimuthal center of the vane. ... .....	37
Figure 3-4 RF electric field for A6 magnetron for narrow A-K gap (left), for large A-K gap (right) [7]. .. .....	39
Figure 3-5 Dispersion diagram for the A6 magnetron using a solid cathode and transparent cathode [31].. ..	40



Figure 3-6 B-H and the Hull cutoff curves for the A6 magnetron with solid cathode... ..	42
Figure 3-7 B-H and the Hull cutoff curves for the A6 magnetron with transparent cathode. ....	42
Figure 3-8 Off-center placement of the cathode strips... ..	45
Figure 3-9 Progress in the formation of spokes for Solid Cathode (top), Transparent Cathode (bottom)... ..	46
Figure 3-10 Output power for the Solid Cathode (top) and Transparent Cathode (bottom). .....	47
Figure 3-11 Microwave output power dependence on applied magnetic field. .	47
Figure 3-12 (Left) Instant turn-on: $t_U < t_s$ ; (Right) Slow turn-on: $t_U > t_s$ . ....	48
Figure 3-13 Magnetic field dependence on microwave output power with an applied voltage of rise time 1ns. ....	49
Figure 3-14 Appearance of stable operating modes in the A6 magnetron with Solid Cathode (top) and Transparent Cathode (bottom). ....	50
Figure 3-15 Direction of DC electric field around the cathode strip at its optimal position. .....	51
Figure 3-16 Particle plot and their direction of drift in the favorable phase. ....	53
Figure 3-17 Particle plot and their direction of drift in the unfavorable phase. ....	53
Figure 3-18 The SINUS-6 voltage waveform.. ....	54
Figure 3-19 Dependence of magnetic field on microwave power.. ....	55
Figure 3-20 Microwave signal obtained at the optimum magnetic field. ....	56

Figure 3-21 The FFT of the RF signal showing single frequency operation for the transparent cathode, while slight mode competition is observed in the case of the solid cathode. ....	56
Figure 3-22 Comparison of microwave output power with the 20° extraction and the 10° extraction schemes. ....	57

## CHAPTER 4

Figure 4-1 Principle elements of the SINUS-6 accelerator. ....	58
Figure 4-2 Equivalent circuit of the SINUS-6 electron beam accelerator.. ....	59
Figure 4-3 Schematic of the SINUS-6 electron beam accelerator before modification. .	62
Figure 4-4 Schematic of the SINUS-6 electron beam accelerator after modification.. ....	62
Figure 4-5 Details of the SINUS-6 control system.. ....	64
Figure 4-6 Equivalent circuit of the pulse stretcher. ....	65
Figure 4-7 The physical dimensions of the optimized coil design.. ....	68
Figure 4-8 Magnetic field uniformity along the length of the magnetron, and between the A-K gap. ....	68
Figure 4-9 Photograph of the manufactured Helmholtz Coils. ....	70
Figure 4-10 Magnetic field distribution of the manufactured Helmholtz coils. ....	70
Figure 4-11 The RLC circuit diagram for the pulsed magnets. ....	72
Figure 4-12 Current waveform when the capacitor is discharged into the coils ....	73
Figure 4-13 Discharge voltage of the capacitor. ....	73
Figure 4-14 Flashover strength versus angle of insulator for Lucite between parallel plate electrodes [51]. ....	77

Figure 4-15 Insulator stack with parallel plate grading ring. ....	78
Figure 4-16 Electron trajectories at the cathode triple point in the absence of applied axial magnetic field. ....	79
Figure 4-17 Equipotential lines generated by MAGIC showing weakening of the radial electric field at the triple junction of the 45° insulator. ....	80
Figure 4-18 The radial electric field measured along the surface of the insulator. ....	81
Figure 4-19 Vacuum chamber section showing parameters D, R and L that had to be optimized. ....	82
Figure 4-20 Possible scenarios of leakage electrons in the upstream direction depending on the length L, of the section shown in Fig 4-18. ....	84
Figure 4-21 Magnetic field lines predicting the electron trajectories defined by the coils using FEMM. ....	85
Figure 4-22 Particle trajectories from MAGIC simulation showing that the leakage electrons are trapped by the dome. ....	85
Figure 4-23 P-SPICE model of the SINUS-6 accelerator to estimate final voltage rise-time at the magnetron load. ....	87
Figure 4-24 Voltage traces at the source and the load from the PSPICE simulation. ....	87
Figure 4-25 Equivalent circuit of the capacitive divider probe on SINUS-6. ....	89
Figure 4-26 Calibration setup for the capacitive divider probe. ....	90
Figure 4-27 Equivalent circuit of the calibration setup. ....	90
Figure 4-28 (top) Full trace of the capacitive divider probe response (bottom) zoom-in on the full trace to determine voltage response more accurately. ....	91
Figure 4-29 Basic structure of a Rogowski coil [64]. ....	92

Figure 4-30 Equivalent circuit of an integrating Rogowski coil [44].	93
Figure 4-31 Photograph of the fabricated Rogowski coil.	95
Figure 4-32 Schematic of coil calibration setup.	97
Figure 4-33 Rogowski coil response versus the response of a Tektronix current transformer.	98
Figure 4-34 Cross-sectional view of a typical loop directional coupler [70].	100
Figure 4-35 RF signal picked up by the directional coupler.	101

## CHAPTER 5

Figure 5-1 Photographs of a) transparent cathode, b) solid cathode and c) A6 magnetron manufactured at UNM.	103
Figure 5-2 Trigger timings and current in the RLC circuit.	103
Figure 5-3 A schematic of the experimental setup.	105
Figure 5-4 Voltage and current measurements with respect to magnetic field for the transparent cathode.	107
Figure 5-5 Voltage and current measurements with respect to the magnetic field for the solid cathode.	107
Figure 5-6 Average RMS power as function of magnetic field for the transparent cathode.	108
Figure 5-7 Average RMS power as function of magnetic field for the solid cathode.	108
Figure 5-8 Average RF envelopes for the A6 magnetron driven using a transparent and solid cathode.	109

Figure 5-9 FFT of the RF signal for the A6 magnetron driven by a transparent cathode (top) and a solid cathode (bottom). .....110

Figure 5-10 Synchronized voltage, current, and microwave signals for the transparent cathode. ....111

Figure 5-11 The r- $\theta$  view of the distorted magnetron modeled in MAGIC. ....113

Figure 5-12 Time evolution of spoke formation in the distorted magnetron. ....113

Figure 5-13 Anode current as a function of axial magnetic field.. .....114

Figure 5-14 Average microwave power as a function of axial magnetic field. ....114

Figure 5-13 Anode current as a function of axial magnetic field.. .....114

Figure 5-14 Average microwave power as a function of axial magnetic field. ....114

**APPENDICES**

Figure A-1 Discharge voltage of the capacitor bank into the coil. ....120

Figure A2-1 Dimensions required fro calculating self inductance. ....121

Figure A2-2 The self-inductance factor plotted against  $\alpha$  and  $\beta$  [73]. ....122

Figure A2-3 Dimensions required for calculating the mutual inductance. ....123

Figure A2-4 Values for factor f [73]. . ....124

Figure A3-1 Time frequency analysis of experimental data for solid cathode. ....125

Figure A3-2 Time frequency analysis of experimental data for transparent cathode. ....126

Figure A4-1 Calibration data for Port 1 of the E-band directional coupler. Port 1 was tuned for 70 dB attenuation at 3.6 GHz. ....127

Figure A4-2 Calibration data for port 2 of the E-band directional coupler. Port 2 was  
tuned for 70 dB attenuation at 4.0 GHz. ....127

Figure A4-3 Calibration data for the RG213 Cable .....128

## LIST OF TABLES

Table 3.1 Spatial grid resolution of the interaction space. ....	43
Table 4.1 Comparison of the calculated and measured electrical parameters of the coil	71
Table 4.2 Summary of the LCR circuit parameters .....	74
Table 4.3 Maximum radial electric fields along the insulator surface.....	80
Table 4.4 Equivalent impedance and electrical lengths of the transmission line model	.86
Table 4.5 Rogowski coil's physical parameters .....	96
Table 5.1 Comparison of results predicted by simulations and observed experimentally	
Comparison of the calculated and measured electrical parameters of the coil .....	112

# Chapter1

## Introduction

### **1-1 Historical Background**

Magnetrons played a major role in the outcome of World War II, more so than the atomic bomb [1-6]. The first magnetron was designed by Sir Arthur Hull in 1912, and it had a smooth bore anode block. This magnetron was flimsy and had very little output power and efficiency. In the quest for finding a reliable microwave source during the invention of early radar systems, klystrons and magnetrons were the two main candidates. Inspired from the study of klystrons, a slow wave (cavity) structure was added to the magnetron anode block by Harry Boot and John Randall [3].

Even though the klystron was a frequency-stable microwave source it did not perform as well as the magnetron in terms of output power. By May 1940, an experimental radar containing a pulsed 10-cm magnetron was in operation, and by September 1940 a submarine periscope could be detected at a range of 7 miles [3].

After WW II, the cavity magnetron became very popular as a result of its robust, powerful performance in radar systems, and a plethora of research avenues were funded and opened. For example, it was applied in industrial processes, household microwave ovens, and civilian radar systems. Research was also performed to solve the problem of mode competition at MIT and other institutions. Mode competition occurs because the RF circuit of a magnetron consists of many resonators coupled together. Consequently a magnetron may have several modes of oscillation which depend upon the coupling between cavities. Several different magnetron geometries such as the rising sun, the strapped magnetron, the coaxial magnetron and the inverted magnetron were developed and studied in order to prevent mode competition and increase the electronic efficiency [6].

Another widely studied area is the “theory of magnetron operation”. To-date there is no text available that can fully explain the physics of magnetrons. However, a comprehensive discussion on this matter can be found in [2, 5, 6].



Furthermore, as modern pulsed power technology became available in the late 1960's the magnetron was explored in the relativistic regime, i.e. with applied voltages in 100's kV range. The first significant relativistic magnetron was designed and built by a team of researchers at MIT [7 - 9]. Among their various designs, the so called A6 magnetron (with 6 cavities) produced microwave power levels exceeding 900 MW in S-band with an applied voltage of 400 kV. This result stirred a lot of interest in the field of relativistic magnetrons and since has been studied by many researchers.

Recently, considerable attention has been given to improving the start time of oscillations in magnetrons, which is critical for modern radar operation.

## **1-2 Modern Sources for Radar and Communications Systems**

Radar systems locate and characterize distant objects by radiating electromagnetic energy from an antenna in the direction of the objects and detecting and measuring the reflected signals. While many of the advances in radar systems over the past 50 years relate to the improved processing of the returned signal, some of the more recent advances in radars are based on the development of two classes of high power microwave (HPM) sources: high peak power and short-pulse sources [1].

### **1-2-1 Short Pulse Radars**

The principle advantage of short-pulse radars is in range resolution. Conventional radars achieve range resolution using long microwave pulses by radiating a pulse with a frequency chirp,  $\Delta f$ , and using digital pulse compression of the received signal to provide an effective pulsewidth of approximately  $1/\Delta f$ . However, the signal processing of the received signal introduces temporal side lobes that can mix signals from nearby range cells. As a result, the received signal from a large cross-section object can conceal signals from smaller targets in its proximity. This problem does not occur with short pulse radars, because the received signal does not require pulse compression. Since radiation propagates 30 cm in 1 ns, it is evident that the operation of radars with a few nanoseconds pulse duration can provide 1-m range resolution directly. This can help detect small cross section moving objects in the presence of substantial radar clutter [1, 10].

Another advantage to nanosecond radars follows from the fact that the radar receiver must be turned off during the pulse duration of the high-power transmitter in order to protect the receiver electronics. In short pulse radars this “dead time” is small. Note that in some cases, to provide the required average power, short-pulse radars must operate at high repetition rates.

### **1-2-2 High Peak Power Sources**

High peak power sources are generally single-shot microwave sources. In addition to peak power, another important figure of merit for high peak-power sources is the energy contained in a single pulse. The magnetron is a device that has been extrapolated with great success to high peak-powers [1, 11]. However, it is not well suited to short-pulse applications because of the very slow start of microwave oscillations.

### **1-3 Basic Principle of Operation and Start of Oscillations**

A brief discussion of the basic principles of magnetron operation that will eventually lead to the reason for slow start of oscillations is outlined in this section.

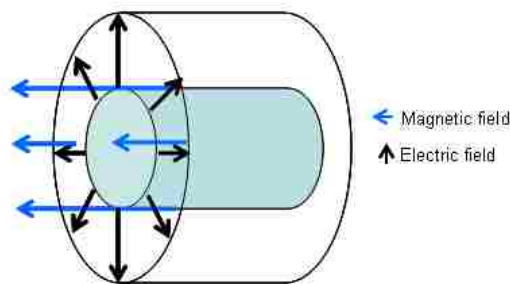


Figure 1-1. Direction of electric and magnetic fields in a crossed-field device of cylindrical geometry.

#### **1-3-1 Basic Principle of Operation**

A magnetron is a crossed-field device. The characteristic feature of a crossed-field device is the use of two parallel conductors, between which a DC electric field,  $E$ , and an

orthogonal DC magnetic field,  $\mathbf{B}$ , that is parallel to the surfaces of the conductors, are applied. When a high voltage is applied across the anode-cathode (A-K) gap the cathode material undergoes explosive emission. This creates a layer of plasma around the cathode from which electrons are extracted. Prior to magnetron oscillation this electron cloud (sheath) circles about the cathode with an  $\mathbf{E} \times \mathbf{B}$  drift. As an increasing anode voltage is applied to a magnetron when it is turned on, the radius of this space-charge cloud grows. (Please note that the applied voltages that provide the radial “DC” electric fields in these problems are pulsed and therefore have finite rise times). As a result both the radius and angular velocity of the space charge cloud surrounding the cathode increase. There is an infinite number of electron velocities that can excite any given mode, in addition to the modes that are supported by the anode vanes or cavity. Furthermore, because of fluctuations in the emission process and noise amplifying effects in the space-charge cloud, electron velocities and charge density in the rotating space-charge cloud fluctuate randomly with time. The frequency of the fluctuations varies over such a wide range that the noise is referred to as “white noise”, which implies fluctuations over an infinite frequency range [3]. The frequency range of fluctuations is rich in components in the microwave range, and so there are components present to initiate any of the frequencies (plasma modes) that may be supported by the cavity structure of a magnetron. The RF fields are select modes which grow from these instabilities.

It is noteworthy that during the initial phase of magnetron research, the diocotron instability was the first plasma instability ever to be discovered [2]. Since then, there has been much discussion to explain these instabilities, and in particular two models have been proposed:

1. double stream instability, in which the particles have cycloidal motion,
2. single stream instability, in which the electrons have a laminar flow, also known as the Brillouin flow [2].

Neither of these models can fully explain the physics that occurs in the electron sheath. However, the latter is the generally accepted model. Despite the complexity of these models, basic magnetron operation can be defined by two equations, namely the Hull cutoff and the Buneman-Hartree (B-H) conditions. The Hull cutoff condition gives the minimum magnetic field that prevents an electron from reaching the anode. The B-H

condition is a synchronous condition that requires an electron to be trapped in the moving frame of reference when it grazes the anode. These two equations govern the basics of magnetron operation to date, even for more complicated and relativistic magnetron designs. Figure 1-2 shows the universal Hull cutoff and B-H curves. For a particular applied voltage the magnetron will oscillate only if the applied DC magnetic field is bound between the two curves.

The Hull cutoff condition and the B-H condition have traditionally been derived from the single particle orbit in crossed electric and magnetic fields in a planar geometry [2, 12]. They have also been studied using the Brillouin flow model [12]. While the Hull cutoff condition has been found to be identical for both the single-particle and the Brillouin flow models, irrespective of the geometry (planar or circular) and the gap voltage (relativistic or nonrelativistic), the B-H condition yields the same results only in the limit of the planar magnetron.

There has been a recent study by Y. Y. Lau et al. that shows that the difference between the two models for the B-H magnetic field is strong for any applied voltage in the cylindrical geometry when the ratio of the anode cathode radii,  $b/a$  is equal to 1.3 and becomes severe as the ratio increases [13, 14]. For example when  $b/a = 4$ , the B-H magnetic field exceeds four times that in the single particle model at a given voltage.

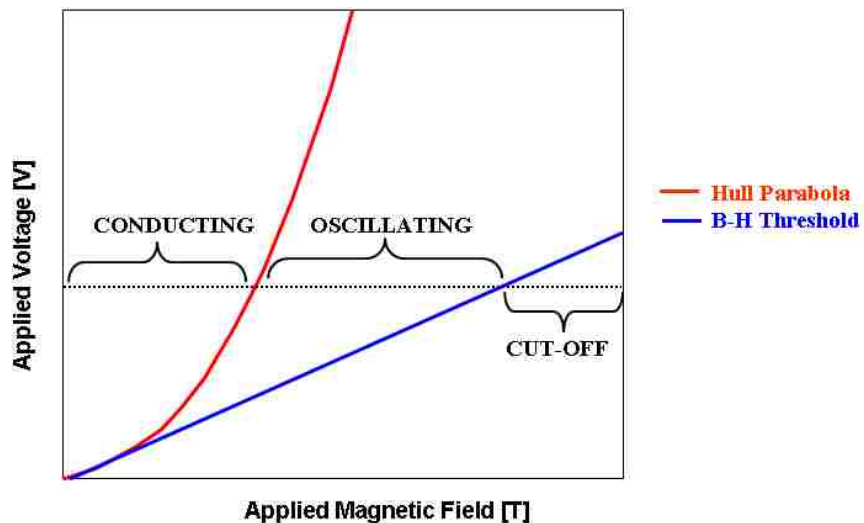


Figure 1-2 General features of magnetron operation domain.

### **1-3-2 Start of Oscillations**

For a magnetron with uniform electron emission (as from a solid cathode), the initial noise described in the preceding section determines the start conditions for the development of instabilities in the electron sheath. The typical level of noise is about  $10^{-10}$  that of the energy of electrons [5]. The time necessary for the development of instability in the electron flow from the initial noise leading to the disruption of the symmetrical electron sheath is at least many 10's of cyclotron periods. Because the anode slow wave structure consists of several resonators, it can support different RF modes. All these modes are present in the electron sheath with different amplitudes. Of all the modes that are possible, the applied DC electric and magnetic field would favor one of the modes. When the RF field associated with that particular mode reaches sufficient amplitude, it will cause periodic swelling of the electron sheath, also known as electron bunching, as indicated in Fig. 1-3. Note that the discrete number of electron bunches is equal to the RF mode number of interest.

The modulated electron cloud is such that some electrons fall in the favorable phase (decelerating RF electric field) and some fall in the unfavorable phase (accelerating RF electric field) as depicted in Fig. 1-3. Those electrons in the unfavorable phase hit the cathode and cause secondary electron emission and act as an electron source while those in the favorable phase get captured into spoke like formations. These electrons lose all their potential energy to the RF fields as they get absorbed in the anode block and hence the RF field grows. This process repeats thereby causing magnetron oscillation. For magnetron oscillations starting in this manner (where the electron bunches are formed due to the interaction of RF fields with the electron sheath) start of oscillations is slow, making them unattractive for short-pulse applications [18]. The following section will describe some recent developments in the area of improving the start-up of oscillations in magnetrons.

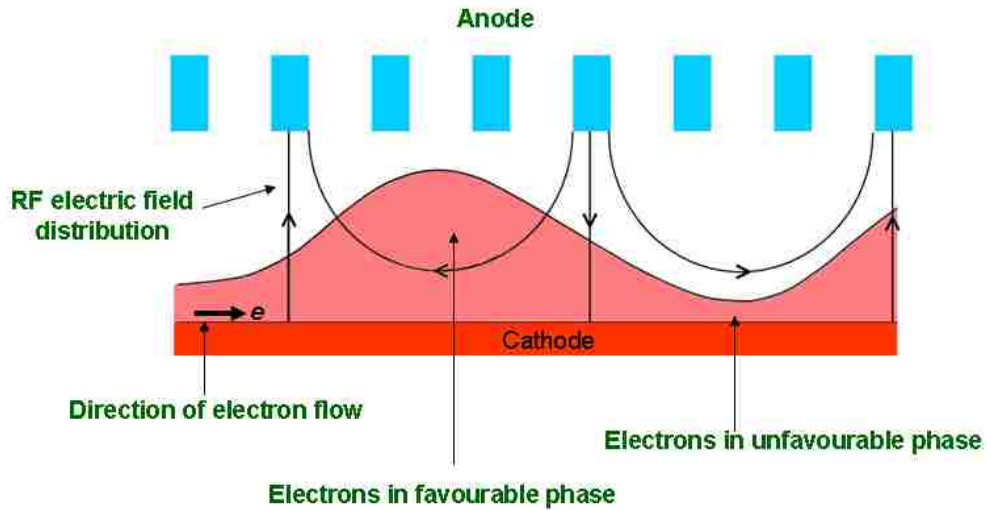


Figure 1-3 Elementary interaction space concepts in a planar magnetron [5]. Here the applied axial B-field points into the page.

#### 1-4 The Concept of Priming

Priming is a technique whereby electrons are prebunched into the desired number of rotating electron spokes. The earliest form of priming to improve startup of oscillations in magnetrons known as RF priming was explored at the US Naval Research Laboratories (NRL), led by Parker et al. [19]. RF priming injects a signal from one source into another oscillator to accelerate the build up of the oscillation of the second (driven) source. This method did not prove to be successful because the input power of the RF source caused arcing at the insulation in the vacuum feedthrough.

Recently, at the University of Michigan (UM) two innovative priming techniques, namely cathode priming and magnetic priming, were explored [20-25]. Both of these techniques will be described in detail in the sections to follow. Electric priming was also explored by Kim et al. where the shape of the anode block was modified in order to allow DC electric field enhancement on the electron sheath [26-28].

The transparent cathode was invented at UNM to address the issue of the slow startup of oscillations in relativistic magnetrons. The design of the transparent cathode was based on the fact that the start time of oscillations is determined by two factors: (1) the start conditions, which give initial impetus to the development of dynamic processes, and (2) the rate of build-up of oscillations [18, 30, 31]. The rate of build-up of

oscillations determines how quickly the microwave oscillations reach saturation and is dependent on the radial velocity,  $v_r$ , of electrons. The radial velocity is in turn dependent on the azimuthal RF electric field,  $E_\theta$ . The structure of the transparent cathode to be described in detail in section 1-6 not only provides a large amplitude of  $E_\theta$  on the electron sheath around the cathode that leads to fast rate of build-up of oscillations, but also offers several different forms of priming.

The concept of the AFRL shaped cathode was extracted from the transparent cathode in an attempt to gain a deeper understanding of the physics of the transparent cathode and will be discussed briefly in section 1-7.

## **1-5 Work conducted at University of Michigan to Improve Start of Oscillations**

To improve conditions for fast start of oscillations, intensive and successful efforts have been undertaken at the University of Michigan. Techniques in RF priming, cathode priming and magnetic priming were proposed. Each of these techniques will be discussed briefly.

### **1-5-1 UM Cathode Priming**

The cathode priming technique uses discrete regions of electron emission periodically arranged along the azimuth of a solid cathode surface. A schematic of this is shown in Fig. 1-4 in the  $r$ - $\theta$  plane [20]. Emission from these discrete regions leads to an azimuthal drift of electron bunches in the crossed fields, which means that the RF current starts practically simultaneously with electron emission. Thus, the RF current appears even earlier than when the solid electron sheath is formed, and the resultant drifting bunches lead to a rotating modulation of the electron sheath. In this process there is no requirement for initial noise level. Furthermore, when the applied voltage exceeds the B-H threshold for the operating wave, bunches in the electron sheath, whose radial excursions exceed the average thickness of the sheath, are picked up by the stronger synchronous RF electric field.

Therefore, use of cathode priming leads to a more rapid start of the microwave oscillations, owing to the rapid formation of the RF current and the capturing of the electrons to the anode by the stronger electromagnetic field.

### **1-5-2 UM Magnetic Priming**

The magnetic priming technique uses an azimuthally modulated magnetic field, which also leads to modulation of electron sheath over the solid cathode surface and amplification of this modulation when the sheath is moving in the periodic magnetic field. Figure 1-5 shows the arrangement of permanent magnets for a 6-cavity magnetron to produce  $\pi$  mode [22] oscillations.

### **1-5-3 UM RF Priming**

RF priming injects a signal from one source into another oscillator to accelerate the build up of the oscillation of the second (driven) source. RF priming is a more general case of phase-locking in which the frequency and phase of two oscillators are locked together for the duration of the microwave output pulse [29].

However, RF priming requires the use of an external source and the associated inefficiencies, cost, weight and volume makes it rather less attractive than cathode or magnetic priming. Of all the priming techniques outlined, cathode priming is the most effective and simplest to implement.

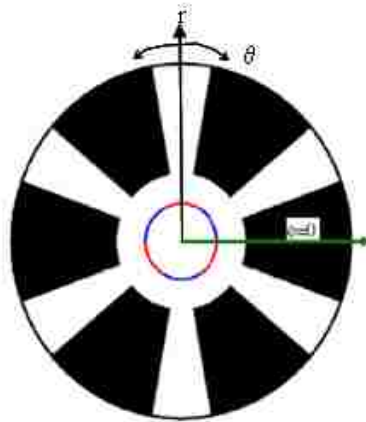


**Figure 1-4 Schematic of a Cathode with discrete emission region for cathode priming [20].**



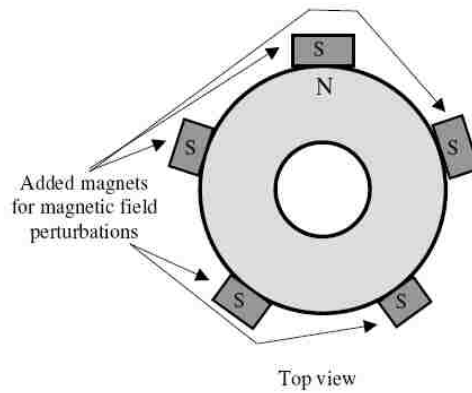


**Figure 1-5 Magnets arranged around the azimuth to create prebunching of electrons for magnetic priming [22].**

### **1-6 Efforts Undertaken at UNM to Improve Start Conditions in Magnetrons**

Priming promotes fast start of the RF current that excites microwave oscillations, but it does not improve the rate of growth of RF oscillations. The velocity of the electrons moving to the anode, which is associated with the rate of conversion of electron energy into electromagnetic energy, remains reasonably low because of the small azimuthal RF electric field,  $E_{\theta}$ , near the cathode.

At the University of New Mexico (UNM) we have proposed the so-called transparent cathode, which not only provides faster start and growth of oscillations, but also shows significant improvement in the output characteristics of a short-pulse magnetron [18, 30, 31]. The structure of the transparent cathode is very simple, in which longitudinal strips of material are removed from a thin-walled tubular cathode. Figure 1-6 is a photograph of a graphite transparent cathode manufactured at UNM.



**Figure 1- 6 Photograph of a graphite transparent cathode.**

The rate of energy transfer between the electrons and the electromagnetic wave determines the rate of growth of oscillations in cross-field devices. This rate depends on the radial drift velocity of the electrons and is denoted by Eq. (1):

$$v_r = \frac{E_\theta}{B_z} \quad (1)$$

Here  $v_r$  is the radial velocity,  $E_\theta$  is the azimuthal component of the RF electric field and  $B_z$  is the applied axial magnetic field. In relativistic magnetrons that implement the solid cathode with uniform electron emission, the amplitude of  $E_\theta$  on the electron flow is very small. This stems from the fact that the boundary conditions force the tangential electric field to go to zero at the surface of the cathode. This may be alleviated by removing longitudinal strips from a thin-walled tubular cathode to make the cathode “transparent” to the azimuthal electric field. This provides a larger amplitude of  $E_\theta$  in the electron sheath region, resulting in faster growth-of-oscillations.

In addition to rapid delivery of electrons to the anode due to the redistribution of the electromagnetic fields, the transparent cathode also provides fast formation of RF current owing to the effects of various forms of priming, e.g. cathode priming, magnetic priming and electrostatic priming, to be elaborated on in Chapter 2. To verify the theory and the concept of the transparent cathode, intense computer simulations were performed on the well known A6 magnetron.

### **1-7 The Air Force Research Laboratory (AFRL) Shaped Cathode**

The transparent cathode geometry provides all of the priming techniques attempted by UM all at once, as well as increasing  $E_\theta$  acting on the electron sheath. The AFRL shaped cathode was created to discern the relative magnitude of influence between UM’s cathode priming techniques and UNM’s improved radial transport through improved  $E_\theta$  [32-34]. Figure 1-7 is a schematic of the AFRL A63 magnetron shaped cathode. The geometry of the shaped cathode marks out certain areas of the smooth-cylindrical cathode in order to enhance explosive emission plasma formation at those

regions. It was discussed in one of AFRL's recent publications that the electrostatic priming played the dominant role in the improvement of microwave output characteristics; however, it must be noted that the shaped cathode geometry still allows  $E_0$  penetration on the electron sheath [34].

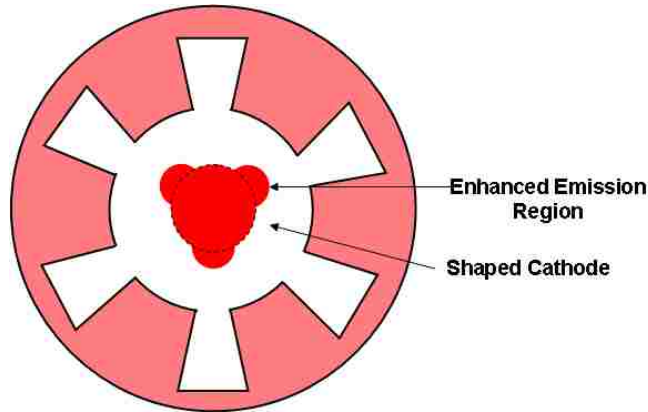


**Figure 1-7 Magnetron with shaped cathode.**

## **1-8 Scope of Dissertation and Chapter Organization**

This dissertation outlines the concept of the transparent cathode and its influence on the output characteristics of a short-pulse relativistic magnetron. Results from computer simulations and proof-of-principle experiments are presented. The remainder of this dissertation is organized as follows:

### **Chapter 2: Theoretical Considerations**

Chapter 2 presents the theory of magnetron operation. The Hull cutoff and Buneman-Hartree conditions, and the physics of spoke formation are discussed. A conceptual study of the growth of oscillations will be explained, followed by a review of the transparent cathode.

### **Chapter 3: Computer Simulations**

Chapter 3 contains a brief description of MAGIC, the three dimensional particle-in-cell (PIC) code that was used to validate the concept of the transparent cathode. Simulations were carried out on the A6 magnetron with the transparent cathode and the traditional solid cathode. The simulations immediately confirmed the superiority of the transparent

cathode, showing high output powers and efficiencies and, single mode operation over a wide range of magnetic field. Further optimization was made, in particular on the effect of voltage rise time on magnetron operation and the waveguide angle for microwave extraction for the mode of interest. And lastly, in order to verify the simulation results experimentally, MAGIC simulations were performed using the voltage characteristics of the SINUS-6 electron beam accelerator.

#### **Chapter 4: Experimental Configuration and Diagnostics**

A major part of this dissertation research was preparation for the experiments. UNM's SINUS-6 accelerator had to undergo several modifications in order for the magnetron experiments to be conducted. Embedded in this chapter is a discussion of the many changes that were introduced to SINUS-6, including design of a new transmission line, vacuum chamber, oil-vacuum interface, pulsed electromagnets, load diagnostics (voltage and current), and microwave diagnostics (power and frequency). The construction and calibration procedure of each diagnostic is included.

#### **Chapter 5: Experimental Results**

This chapter presents the experimental results. The features of the transparent cathode shown in the simulations have been verified experimentally. The transparent cathode showed stable single-frequency operation over a wide range of magnetic field with high output powers. It must be mentioned that the magnetron was slightly distorted during the fabrication process. Despite this, it was fortunate that the transparent cathode outperformed the solid cathode. Because of the distortion in the geometry, the magnetron operated in the  $\pi$ -mode at a frequency of 2.9 GHz. The distorted magnetron geometry was recreated and simulated in MAGIC and the experimental results and mode of operation were verified.

#### **Chapter 6: Conclusion**

The final chapter concludes the dissertation and presents recommended future work.

#### **Chapter 7: Appendix**

The information contained in the appendices are an important part of this dissertation and were not included in the main body of the dissertation to avoid information overload, but are pieces of information that complete this work.

## Chapter 2

### Theoretical Considerations

#### 2.1 Principles of Magnetron Operation

The relativistic magnetron is an M-type crossed-field device. Crossed-field tubes are referred to as “M-type” tubes after the French TPOM, which in English means “tubes for propagation of waves in a magnetic field” [3]. The characteristic feature of crossed-field devices is the use of two parallel conductors between which a DC electric field,  $\mathbf{E}$ , and an orthogonal DC magnetic field,  $\mathbf{B}$ , parallel to the surfaces of the conductors are applied. The theory of magnetron operation is based on the motion of electrons under the combined influence of the electric and magnetic fields, and the interaction of these electrons with the RF fields supported by the slow wave structure of the anode block [2].

In the absence of an electric field, an electron with initial velocity  $U_o$  will follow a circular trajectory of radius  $U_o / \omega_c$  and will rotate at the cyclotron frequency  $\omega_c$ . When an electric field is applied, the electron velocity changes but the frequency of rotation remains fixed at  $\omega_c$ . An electron acquires an average velocity component perpendicular to both the electric field and magnetic field. There is a critical combination of magnetic field and electric fields known as the Hull cut-off condition at which the electrons just touch the outer electrode.

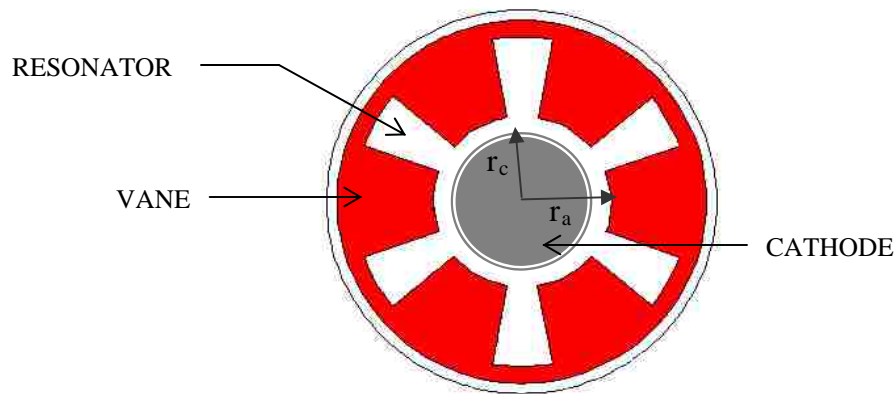


Figure 2-1 6-cavity magnetron geometry.

The cavity magnetron geometry is shown in Fig. 2-1. The cathode is surrounded by an anode cavity structure consisting of identical resonators separated by vanes. When a high voltage is applied across the A-K gap, the cathode surface undergoes explosive electron emission. Almost any surface exhibits microscopic protrusions or whiskers. When exposed to high voltages, electric field enhancement at the whiskers can cause significant high-field emission, overcoming the work function of the material. Subsequently, the whisker may dissipate due to joule heating, resulting in the formation of plasma on the cathode surface. This surface plasma will typically “emit” under the influence of the applied electric field, with the species extracted from the plasma being determined by the direction of the field. These electrons are accelerated towards the anode under the influence of the DC electric field. The DC magnetic field that is orthogonal to the electric field inhibits electron propagation across the gap, which leads to the first condition of magnetron operation: electrons must be sufficiently prevented from reaching the anode. That is, the electrons must satisfy the Hull cut-off condition given by

$$B_H = \left( \frac{m_o c}{|e| D^*} \right) \left[ \frac{2|e|V}{m_o c^2} + \left( \frac{|e|V}{m_o c^2} \right)^2 \right]^{\frac{1}{2}}. \quad (2-1-1)$$

Here,  $B_H$  is the critical field for magnetic insulation,  $m_o$  is the electron rest mass,  $e$  is the electron charge,  $c$  is the speed of light,  $V$  is the voltage applied across the A-K gap and  $D^*$  is the equivalent gap given by

$$D^* = \frac{r_a^2 - r_c^2}{2r_a}, \quad (2-1-2)$$

where  $r_a$  is the anode radius,  $r_c$  is the cathode radius and  $r$  is some radius in between.

These electrons then orbit the cathode at a drift velocity given by

$$v_d = \frac{E \times B}{|B|^2}. \quad (2-1-3)$$

The second and the key condition for magnetron operation is that the anode cavities constitute a slow-wave structure so that the phase velocity of a wave of interest propagating along this structure will equal the electron drift velocity:

$$v_p = \frac{\omega}{k} = v_d, \quad (2-1-4)$$

where  $v_p$  is the phase velocity of the cavity wave or the RF field of frequency  $\omega$  and wave number  $k$ . This resonant state is described by the B-H resonance condition given by

$$B_{BH} = \frac{mc^2 n}{e \omega_n r_a D^*} \left[ \frac{eV}{mc^2} + 1 - \sqrt{1 - \left( \frac{r_a \omega_n}{cn} \right)^2} \right], \quad (2-1-5)$$

where  $\omega_n$  is the frequency of the  $n$ th mode. For voltages greater than the Hull cut-off, the magnetron will result in a short circuit. For voltages less than the B-H thresholds, the magnetron will be non-resonant and therefore will not generate microwaves. The magnetron oscillates when the operating point lies between the cut-off and the threshold curves [2-6]. The Hull cutoff and B-H curves for the magnetron with the two cathodes will be presented in Chapter 3.

The basic conditions for magnetron operation has been established. In the next section the general properties of periodic structures will be discussed.

## **2.2 General Properties of Periodic Structures**

A variety of modes occur in a magnetron because the anode slow-wave structure is, in effect, a group of coupled resonators. Therefore, several possible types of oscillations exist, which differ in the way fields are distributed among the cavities.

In a periodic structure, the Floquet theorem states that the sinusoidal steady state field solutions in time differ by a complex phase factor from one cavity to the next. The electric field in a periodic structure can be written as

$$E(z + L) = E(z)e^{i\Gamma}, \quad (2-2-1)$$

where  $\Gamma$  is a complex constant and  $L$  is the periodicity of the structures [71]. In an  $N$ -cavity magnetron anode block such as that shown in Fig. 2-1, if we fix the radius and move in the azimuthal direction, the structure of the magnetron will appear to be infinitely periodic. According to the Floquet theorem, we can then write

$$E_{n+p} = E_n e^{-jp\Gamma}, \quad n, p = \text{integers} \quad (2-2-2)$$

where the subscript  $n$  represents the  $n$ th section of the magnetron, and  $E_{n+p}$  and  $E_n$  are measured at the distance exactly  $pL$  away from each other. Because of the geometrical periodicity, the  $N$ -cavity magnetron repeats every  $N$  sections,

$$E_{n+N} = E_n e^{-jN\Gamma} = E_n, \quad (2-2-3)$$

which implies that

$$e^{-jN\Gamma} = 1 \quad \text{and} \quad N\Gamma = 2n\pi, \text{ where } n = 0, \pm 1, \pm 2, \dots \quad (2-2-4)$$

$\Gamma$  can be rewritten as

$$\Gamma = \frac{2n\pi}{N}. \quad (2-2-5)$$

The modes are designated by mode number  $n$ , which is the number of times the RF field pattern is repeated in going around the anode once.

In addition to there being several modes of oscillation in a magnetron, there is, quite literally an infinite number of electron velocities that can excite any given mode [3]. In the presence of periodically spaced cavities, however, a certain set of modes excited in the interaction space have phase velocities less than  $c$ . Thus, when phase synchronism is established between any one of these modes  $m$  and the sheared space charge drifting with



velocity  $v_\theta = E_r(r)/B_z$ , strong wave-particle interaction sets in, resulting in efficient conversion of beam energy to electromagnetic energy.

The largest value of  $n$  is  $N/2$ , where  $N$  is the number of cavities. This mode is called the  $\pi$ -mode and is usually the desired mode of operation. However, for the relativistic magnetron under investigation the mode of operation is the  $2\pi$ -mode. Further discussion on this matter can be found in Chapter 3.

In the following section the interaction of the electron beam with the RF fields will be discussed.

### **2.3 Motion and Bunching of Electrons in RF fields of a Synchronous Wave**

The anode block is implemented as a slow-wave structure (SWS). If the externally imposed electric field and axial magnetic field are sufficiently strong, the average motion of the electrons is approximately the  $E \times B$  drift velocity. The electrons achieve an orbit near the cathode, and then move at a velocity given by Eq. (2-1-3). In this frame of reference, the electrons have a residual drift from the RF field. The flow will drift so as to form two regions.

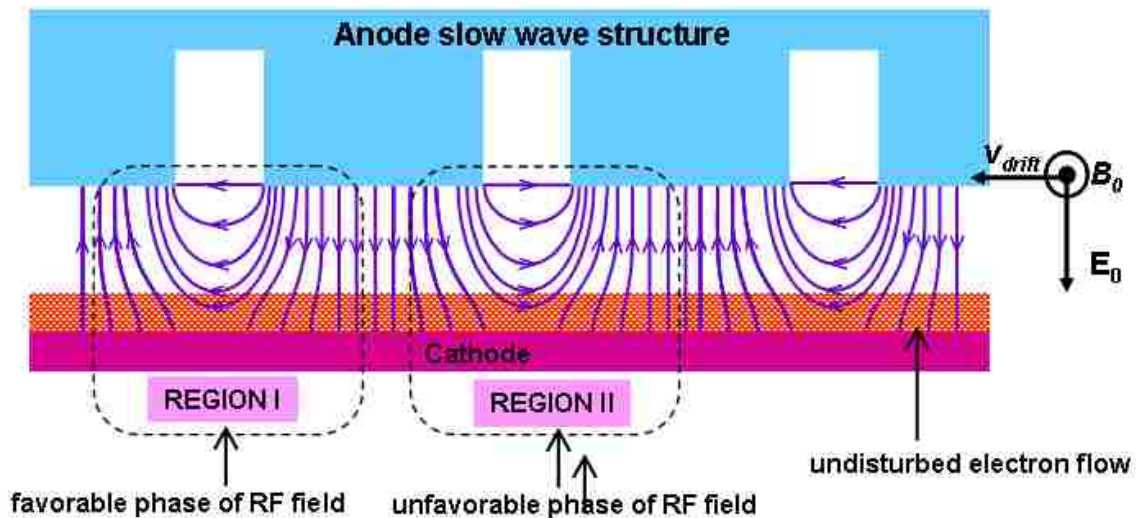


Figure 2-2 RF electric field distribution of the  $\pi$ -mode in the interaction space.

In Region I electrons fall in the favorable phase of the RF field and in Region II they fall in the unfavorable phase of the RF field. Figure 2-2 shows the RF field distribution of the  $\pi$ -mode in a planar magnetron at one instant in time.

The electrons in the favorable phase execute an upward drift closer to the anode. During this course the electrons experience a loss of potential energy associated with the DC electric field. The conservation of energy requires that this potential energy be converted to the RF. Here the electrons lose energy to the wave, and move toward the anode. Electrons in Region II gain energy from the RF wave, move toward the cathode and are either reabsorbed there or lead to secondary electron emission.

This process forms a pattern of spokes. The RF fields are stronger near the resonant cavity than they are closer to the cathode. On the whole, the amount of energy electrons in the unfavorable phase gain from the RF is less than the electrons in the favorable phase lose to the RF hence the RF signal grows.

In systems described above each mode grows from the ambient noise of the electron cloud or the Brillouin layer. The typical level of noise is about  $10^{-10}$  of the energy of electrons [5, 31]. The time necessary for the onset of azimuthal modulation from the initial noise is at least tens of cyclotron periods, leading to slow start of microwave oscillations and even mode competition.

## **2.4 The RF Field Solutions**

The resonant frequencies and corresponding RF fields of the anode block in the absence of space-charge are now derived [5, 6, 19]. With no sources, Maxwell's equations simplify and the static electric and magnetic fields, which have no effect on the resonant frequencies, can be ignored. Also, the problem is restricted to transverse electric (TE) waves and the magnetron is treated as a waveguide of unusual cross-section. Given these simplifications, the problem still cannot be solved analytically because of the complex boundary conditions at the anode. An approximate analytic solution can be found by dividing the anode into two parts: the resonators and the interaction space. The field structure is solved for each region with the same assumed boundary condition at the

common boundary. The resonant frequencies are determined by matching the admittances for each region.

Cartesian coordinates are used to solve for the field quantities. Only  $E_x$ ,  $E_y$ , and  $B_z$  can be nonzero, and only TE waves are allowed. Assuming a time dependence of  $\exp(i\omega t)$ , each field component,  $F$ , satisfies the wave equation

$$\nabla^2 F + k^2 F = 0 \quad (2-4-1)$$

where  $k = \omega/c$  is the free-space wave number. The metal walls are assumed to be perfect conductors so that the electric field is zero at the metal boundaries. The crucial assumption is that, across the resonator opening, a constant electric field of value  $E$  exists. Given these boundary conditions and further assuming that  $l < \lambda/2$ , where  $\lambda (= 2\pi/k)$  is the free space wavelength, the field solution are:

$$E_y = E \frac{\sin k(l-x)}{\sin kl} \exp(i\omega t) \quad (2-4-2)$$

$$B_z = -i \frac{E}{c} \frac{\cos k(l-x)}{\sin kl} \exp(i\omega t) \quad (2-4-3)$$

and all other field components are zero. This is essentially the field solution for half of a rectangular waveguide in the  $TE_{10}$  mode.

The interaction space is analyzed using cylindrical coordinates. The wave equation must still be satisfied, but with more complex boundary conditions. Consider the case of  $N$  resonators, when  $N$  is restricted to even numbers, labeling each gap by  $s = 0, 1, \dots, N-1$ . The tangential electric field is zero on the cathode surface and along the metal surfaces of the anode and is constant across the gap so that the fields in the resonators may be matched to those in the interaction space. At adjacent gaps, the field differs by a phase constant related to the periodicity of the interaction space. Mathematically, the boundary conditions are

$$\begin{aligned}
E_\theta(r_c, \theta) &= 0 \\
E_\theta(r_a, \theta) &= E \exp \frac{i2\pi m s}{N}, & \text{if } \left| \theta - \frac{2\pi s}{N} \right| < \psi \\
&0, & \text{other } \theta \text{ values}
\end{aligned} \tag{2-4-4}$$

where  $n$  is any integer.

By separating variables in Eq. 2-4-1, the solution is a combination of Bessel functions of the radial coordinate and  $\exp(ik\theta)$  in the angular coordinate. The boundary condition at the cathode is satisfied by a combination of Bessel functions. The anode boundary conditions require a Fourier series expansion with a full set of spatial harmonics in the angular coordinate. Neglecting the common factor  $\exp(i\omega t)$ , the field solutions are

$$E_\theta(r, \theta) = E \frac{N\psi}{\pi} \sum_{m=-\infty}^{\infty} \frac{\sin k\psi}{k\psi} \frac{z'_k(kr)}{z'_k(kr_a)} \exp ik\theta \tag{2-4-5a}$$

$$E_r(r, \theta) = -iE \frac{N\psi}{\pi k r} \sum_{m=-\infty}^{\infty} k \frac{\sin k\psi}{k\psi} \frac{z_k(kr)}{z'_k(kr_a)} \exp ik\theta \tag{2-4-5b}$$

$$B_z(r, \theta) = -iE \frac{N\psi}{c\pi} \sum_{m=-\infty}^{\infty} k \frac{\sin k\psi}{k\psi} \frac{z_k(kr)}{z'_k(kr_a)} \exp ik\theta \tag{2-4-5c}$$

where,

$$z_k(kr) = J_k(kr) - \frac{J'_k(kr_c)}{Y'_k(kr_c)} Y_k(kr), \tag{2-4-5d}$$

$k = \omega/c$  is the free space wave number,  $J_k$  is the Bessel function of the first kind of order  $k$ , and  $Y$  is the Bessel function of the second kind and the primes denote differentiation with respect to  $k_r$  [19]. The integer  $k = n + mN$  varies from  $-\infty$  to  $+\infty$  as  $m$  varies.

The fields for  $n = 0$  and  $n = N/2$  are nondegenerate standing waves. All other  $n$  values result in two degenerate field patterns because of the different directions of rotation in the  $\theta$  coordinate for  $n = s$  and  $n = -s$ . Equations 2-4-5 show that, near the

cathode surface, the RF electric field is very weak and is dominated by the lowest  $k$  modes. Hence, the lowest order spatial harmonics will be most important when considering interaction with electrons.

## **2.5 Growth of Oscillations**

It has been shown in the preceding section regarding boundary conditions that near the cathode surface the RF fields are very weak. The point of focus for this section is to elaborate on the importance of the azimuthal component of the RF electric field,  $E_\theta$  on the rate of growth of oscillations in magnetrons. The radial distribution of the azimuthal electric field of the operating mode,  $E_\theta(r)$  given by Eq. 2-4-5 a, determines the average velocity of electron motion to the anode

$$v_r = \frac{E_\theta B_{oz}}{B_0^2} \quad (2-5-1)$$

and therefore, determines the rate of energy conversion of electron potential energy into RF energy in the regions where  $[\vec{E}_\theta \times \vec{B}_o] > 0$ . Here,

$$B_o = \sqrt{B_{oz}^2 + B_{o\theta}^2} \quad (2-5-2)$$

is the magnetic field tangent to the anode surface and

$$B_{o\theta} = \frac{\mu_o I_z}{2\pi r} \quad (2-5-3)$$

is the azimuthal magnetic field associated with the axial cathode current  $I_z$ , and  $\mu_o$  is the permeability of free space. Therefore, weak  $E_\theta$  near the cathode surface would lead to slower rate of build-up of oscillations.

The growth rate  $Im \omega$  of oscillations is estimated using the Brillouin model and the final result is expressed as [3, 28]

$$\text{Im} = \frac{1}{8t_s} \left( -1 \pm \sqrt{1 + 32\chi_s \frac{eE_o S_c}{m V} t_s^2} \right) \quad (2-5-4)$$

Here  $S_c$  is the cathode area,  $t_s$  is the characteristic fill-time of the resonant system by electromagnetic energy of the  $sth$  mode and is given by

$$t_s = \frac{Q_s}{\omega_s} \quad (2-5-5)$$

$\chi_s$  is the ratio of the square of the azimuthal electric field on the surface of the electron sheath to the square of the average electric field in the resonant system given by

$$\chi_s = \frac{E_{s\theta}^2(\Delta)}{\frac{1}{V} \int_V |\vec{E}|^2 dV} \quad (2-5-6)$$

and  $\Delta$  is the sheath thickness and is expressed as

$$\Delta \approx \frac{2\gamma_e v_e}{\omega_H} \quad (2-5-7)$$

Here,  $\omega_H$  is the cyclotron frequency and  $\gamma_e$  is the relativistic factor corresponding to the electron sheath drifting with velocity  $v_e$  parallel to the cathode surface,

$$\omega_H = \frac{eB_o}{m\gamma_e} \quad (2-5-8)$$

$$\gamma = \left( 1 - \frac{v_e^2}{c^2} \right)^{\frac{1}{2}} \quad (2-5-9)$$

$$v_e = \frac{E_{or}}{B_o} \quad (2-5-10)$$

Thus Eq. (2-5-1) and (2-5-4) show that fast growth of oscillations can be provided by increasing the azimuthal electric field  $E_\theta$ , on the electron sheath,  $\Delta$ .

The theoretical material discussed so far has shown that a large amplitude of  $E_\theta$  is required for fast growth of oscillations. A magnetron with solid cathode would not be able to meet this requirement since the boundary conditions would force the field to go to zero at the surface of the cathode leaving only a small amplitude of  $E_\theta$  near the cathode surface where electrons are emitted. A transparent cathode was developed at UNM the structure of which not only allows a large amplitude of  $E_\theta$  on the electron flow, but also has provides three distinct forms of priming. The features of the transparent cathode are discussed in more detail in the following section.

## 2.6 The Transparent Cathode

The initial motivation for the transparent cathode was to increase the rate of build-up of oscillations in short-pulse magnetrons by increasing the synchronous electric field,  $E_\theta$  in the electron hub region. This was accomplished by removing longitudinal strips of material from a hollow cathode [18, 30], thus making the cathode transparent to the field with azimuthal orientation in which the axial component of the electric field is absent since the operating modes in magnetrons are TE modes. This effect is synonymous to a transparent grating consisting of wires that are perpendicular to the polarization of an incident wave as depicted in Fig. 2-3 (right). The “transparent cathode” was named after this feature. Figure 2-3 (left) is a photograph of a transparent cathode manufactured at UNM.

In addition the transparent cathode offers three distinct forms of priming: cathode priming, magnetic priming and electrostatic priming self consistently. This chapter will highlight the manifold features and advantages of the transparent cathode.

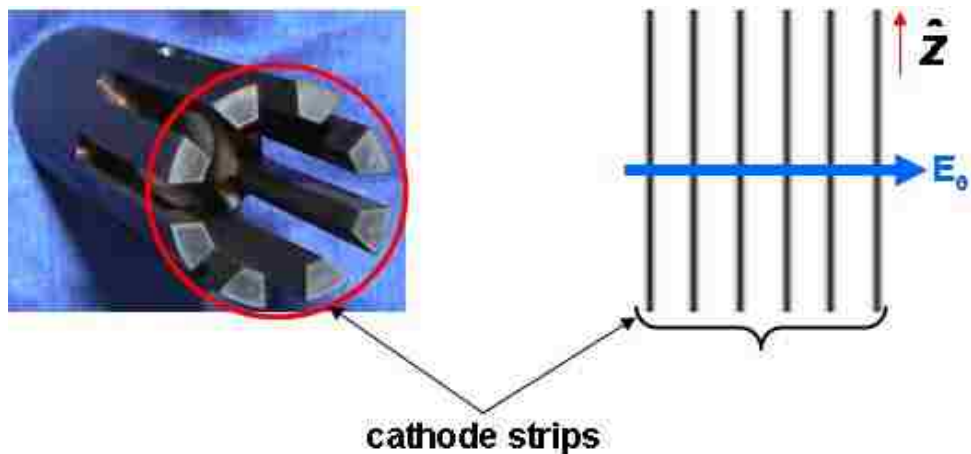


Figure 2- 3 (Left) Photograph of a transparent cathode made of graphite, (right) cathode strips perpendicular to the direction of  $E_\theta$ .



### 2.6.1 Rate of Buildup of Oscillations

The transparent cathode provides rapid delivery of electrons to the anode. As outlined in the preceding section the rate of growth of oscillations is determined by the average radial velocity of electron motion to the anode  $v_r$  which is dependent on the magnitude of  $E_\theta$  expressed by Eq. 2-5-1. In a magnetron with such a cathode, the synchronous azimuthal RF electric field,  $E_\theta$ , is distributed as a modified Bessel function of the first kind of order  $n$  [30] as

$$E_{\theta\text{-transparent}}(r) = \frac{E_\theta(r_a)I_n(gr)}{I_n(gr_a)} \quad (2-6-1)$$

where  $n$  is the azimuthal index of the operating wave. In the case of a magnetron with solid cathode the radial distribution of  $E_\theta$  was expressed by eq. 2-4-6a

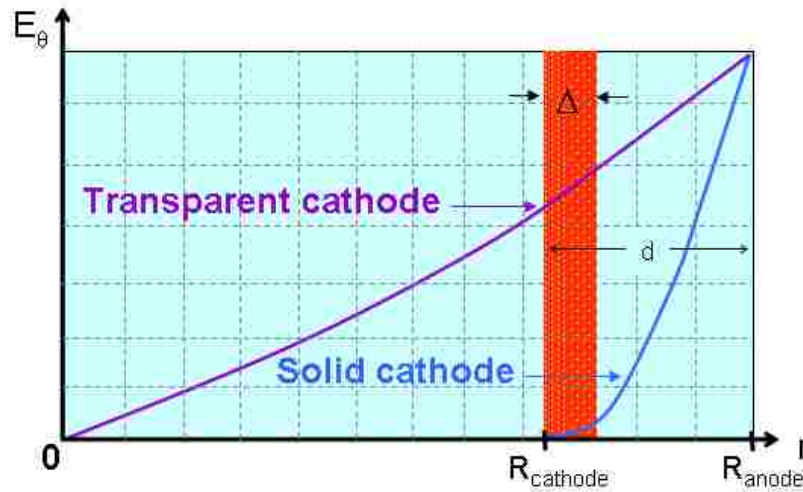
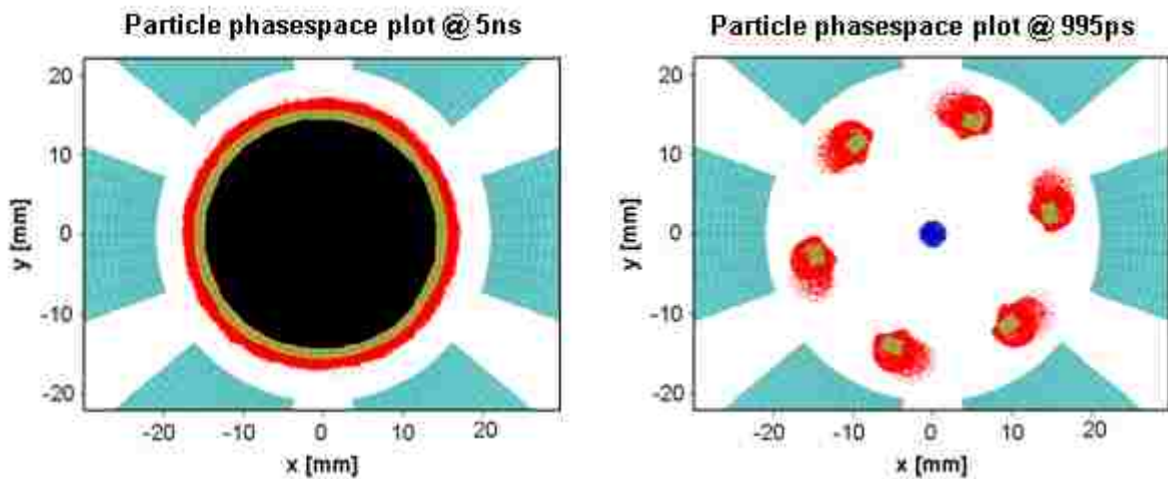


Figure 2-4 Dependence of the azimuthal electric field of the synchronous wave on radial position for a transparent cathode versus a solid cathode. Here  $r_a$ ,  $r_c$  and  $\Delta$  are anode radius, cathode radius and the electron hub height, respectively.

The red shaded region in Fig. 2-4 represents the electron sheath at the cathode surface. For the case of the transparent cathode the  $E_\theta$  distribution takes a form such that it leaves a large amplitude on the electron flow. It follows from Eq. 2-5-1 then that a magnetron that uses a transparent cathode would exhibit faster rate of build-up of oscillations. On the other hand, for a solid cathode the boundary conditions force the  $E_\theta$  field to go to zero at the cathode surface and monotonically increase to the electron sheath rotating around the cathode. Thus, for a magnetron with solid cathode one would rely on the RF fields to grow to a large enough amplitude and finally reach saturation through the natural process.

### **2.6.2 Cathode Priming in a Transparent Cathode**

The technique of cathode priming invented at UM [20] introduces periodic electron emitting zones around the azimuth of a solid cathode. This method of priming immediately forces electrons to bunch into the desired mode. The structure of the transparent cathode serves a similar purpose where each cathode strip acts as a discrete emission region.



**Figure 2- 5 (Left) Solid ring of electrons around the solid cathode. (Right) Electron prebunching in the transparent cathode.**

Figure 2-5 presents the electron phase space plot taken from MAGIC simulation results for these two cathodes at a given instant of time. In these simulations the applied voltage pulse ramped up to a maximum voltage of 350 kV in 1 ns after which it stayed constant up to 40 ns. The cathode and anode surfaces were treated as perfect conductors. The cathode was allowed to emit electrons when the electric field reached a threshold value of 100 kV/cm on the cathode grids. The simulation model is outlined in more detail in Chapter 3. Figure 2-5 left shows the evolution of the electron cloud around the solid cathode at 5 ns. There is only a solid ring of electrons around the cathode which is closely packed into a Brillouin hub with no apparent sign of beam modulation due to RF fields. In the case of the transparent cathode (Fig. 2-5 right), however, simulations show prebunched electrons with six-fold symmetry being released into the  $E \times B$  fields of the magnetron interaction space around 995 ps. (The “interaction space” is defined to be the region where the main physics of magnetron operation takes place.) The electron prebunching is attributed to cathode priming while the very early appearance of electrons is attributed to the electrostatic priming effect. Electrostatic priming takes place due to the concentration of electric field lines around the cathode strip and will be further elaborated on in Section 2.6.4. Prebunching the electrons in this manner suggests that the RF current starts practically simultaneously with electron emission. Thus, the RF current appears even earlier than when the solid electron sheath is formed, and the resultant drifting bunches lead to a rotating modulation of the electron sheath. Note that 6 cathode strips were chosen in order to give impetus to the formation of 6 discrete electron bunches. The A6 magnetron explored in this research favors  $2\pi$ -mode oscillations which has a six-fold symmetry in the electron spokes and therefore it is only logical to use 6 cathode strips. Hence, mode pre-selection can be achieved in a magnetron with transparent cathode by choosing an appropriate number of cathode strips.

### 2.6.3 Magnetic Priming in a Transparent Cathode

The magnetic priming technique, also invented at UM [22], introduces an azimuthal perturbation in the axial magnetic field by the use of external permanent magnets arranged around the azimuth of the magnetron. Magnetic priming takes place self-consistently in a magnetron using a transparent cathode. The axial currents along the longitudinal cathode strips produce periodically alternating azimuthal magnetic fields locally around the strips as shown in Fig. 2-6.

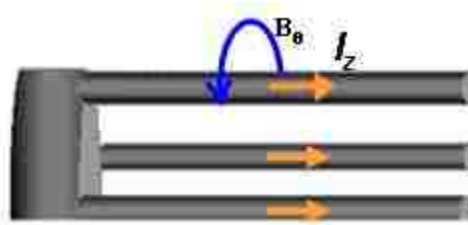


Figure 2-6 Magnetic field  $B_\theta$  resulting from the current through each strip.

The magnetic field in the space around individual cathode strip, at a distance  $r$  is expressed in equation form using Ampere's Law,

$$B_{N\theta} = \frac{\mu_o I_{NZ}}{2\pi r} \quad (2-6-2)$$

A simple simulation was performed using a 2-dimensional magnetostatic code FEMM to visualize the form the magnetic field lines would adhere to, in the magnetron interaction space, in the presence of 6 cathode strips. Each cathode strip was modeled to have a wedge-like cross-section and had 3 kA of current passing through it. In a typical MAGIC simulation that yielded coherent microwave oscillations in the  $2\pi$ -mode the total anode current was measured to be approximately 18 kA. The leakage current in both the upstream and downstream directions are small in comparison to the anode current. Even though the axial current gradually decreases along the cathode down to the value of the leakage current, it is reasonable to estimate an average of 3 kA of current through each

strip (i.e. 18 kA ÷ 6 strips) in the main interaction space. Figure 2-7 shows the simulation result for the resultant magnetic flux density and the magnetic field lines around the circumference of the cathode due to the current distribution through each cathode strip.

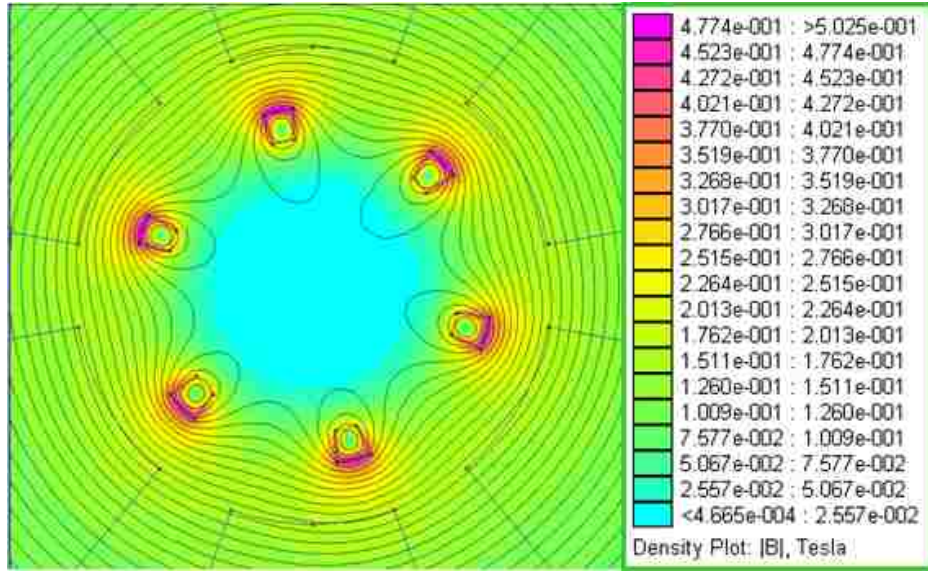


**Figure 2-72 Magnetic flux distribution as a result of axial current through each cathode strip.**

The periodic modulation of the  $B_\theta$  field is apparent in Fig. 2-7. One would expect the rotating electron cloud around the cathode strips to be modulated by this field distribution.

Furthermore, the  $B_\theta$  field crossed with the radial DC electric field leads to electron drift in the axial direction, expressed by Eq. 2-6-3. Hence, the  $B_\theta$  could contribute to leakage current in magnetrons.

$$v_{z\_drift} = \frac{E_r}{B_\theta} \tag{2-6-3}$$

Thus, in the case of the solid cathode  $B_\theta$  only leads to reduction of total efficiency while in the case of the transparent cathode it adds the benefit of magnetic priming.

Next let us examine the effect  $B_\theta$  has on the cyclotron radius of the electrons orbiting the cathode. It has been established that the electrons emitted off the cathode surface execute a drift in the azimuthal direction under the influence of the radial electric field and the applied axial magnetic field. This drift velocity is given by,

$$v_d = \frac{E_r}{B_z} \quad (2-6-4)$$

Thus, the electron cyclotron radius  $R_H$  can be defined as the ratio of the electron drift velocity,  $v_d$  and the electron cyclotron frequency,  $\omega_H$ . The cyclotron frequency is given by

$$\omega_H = \frac{e B_o}{m} \quad (2-6-5)$$

where  $e$  and  $m$  are the electron charge and mass, respectively and  $B_o$  is the total magnetic field given by

$$B_o = \sqrt{B_z^2 + B_\theta^2} \quad (2-6-6)$$

Taking the ratio of Eqs. 2-6-5 and 2-6-6 and rearranging them yields

$$R_H = \frac{m}{e} \frac{E_r}{B_z \sqrt{B_z^2 + B_\theta^2}} \quad (2-6-7)$$

Equation 2-6-7 explains that the electron cyclotron radius is mainly dependent on the axial magnetic  $B_z$ .

### 2.6.4 Electrostatic Priming in a Transparent Cathode

Electrostatic priming results from the concentration of electric field lines around the cathode strips as depicted in Fig. 2-8. Concentration of electric field lines leads to electric field enhancement around the cathode strips leading to early emission of electrons and may eventually lead to faster start of oscillations. Electrostatic priming also results in periodically modulated radial electric field  $E_{0r}$  whose value varies along the cathode depending on whether the position is underneath cavities or between them, which leads to the appearance of an azimuthally nonuniform thickness  $\Delta$  of the electron sheath.

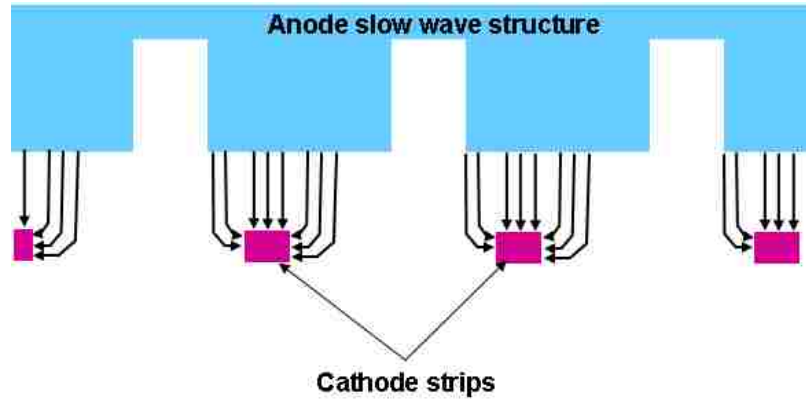


Figure 2-8 Electric field enhancement near cathode strips.

Electrostatic priming is mostly effective when the anode-cathode gap is small, i.e. the ratio of the anode radius,  $r_a$  to cathode radius  $r_c$  is less than 5. For  $r_a/r_c > 5$  the inhomogeneity of the electric field on the cathode decreases, making the electric field modulation negligibly small [30].

Figure 2-9 shows the electric field distribution for a magnetron with solid cathode. The vanes of the anode block perturb the radial electric field in the interaction space. The darker lines indicate stronger electric field and the lighter lines represent weaker electric field. This could be disadvantageous for a magnetron with solid cathode since the varying degrees of electric field around the cathode would allow a greater spread in the electron drift velocities giving rise to mode competition. This sort of

unwanted electron drift is absent in the case of the transparent cathode thereby increasing the chances of mode purity.

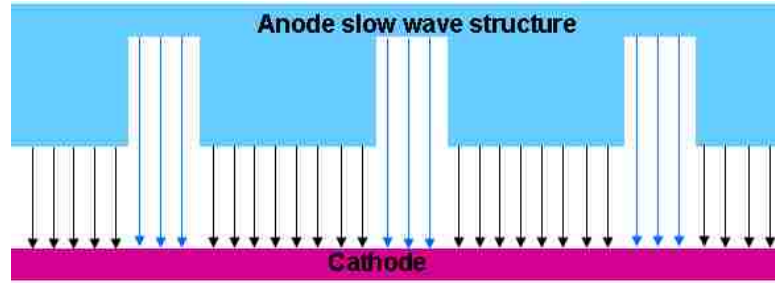


Figure 2-9 Electric field lines for a planar magnetron with solid cathode.

### 2.6.5 Other Merits of the Transparent Cathode

Short cathode life time has been an issue in magnetrons particularly in systems that have long voltage pulses, typically in the range from 100 ns to several microseconds. As outlined in section 2.1, in the oscillating state the space-charge cloud around the cathode may be divided into two principle regions. Region I contains electrons that fall in the favorable phase of the RF fields and region II contains electrons that fall in the unfavorable phase. The electrons in the favorable phase lose their energy to the RF fields. In principle the energy transfer of electrons to the RF field is essentially by extraction of potential energy from the radial DC electric field as they are moved toward the (higher potential) anode by the RF fields [5]. The average lifetime of electrons in the favorable phase is given by the relation 2-6-9, which is derived from the synchronous condition,

$$\left| \frac{\omega}{v_e} - \frac{\omega}{v_{ph}} \right| L_{e\theta} < \pi \quad (2-6-8)$$

where  $L_{e\theta}$  is defined as the azimuthal path of electrons and can be expressed as

$$L_{e\theta} = v_e \tau_e \quad (2-6-9)$$



Here,  $\omega$  is the electron cyclotron frequency,  $v_e$  is the electron drift velocity,  $v_{ph}$  is the phase velocity of the synchronous wave and  $\tau_e$  is the average life time of an electron in the favorable phase of the RF field during their motion to the anode. Eventually the electrons in the favorable phase make their way to the anode seeding the formation of anode plasma. In a similar manner, electrons in the unfavorable phase strike back on the cathode surface usually with very strong force [5]. While electron back-bombardment of the cathode surface causes secondary electron emission thereby acting as a source of electrons its effects can be detrimental to the average life time of the cathode.

In the case of a magnetron that uses a transparent cathode, due to the discontinuous periodic arrangement of the cathode surface there is almost no surface area available for electron back bombardment. Hence one would expect a longer life expectancy for a transparent cathode compared to a solid cathode.

Furthermore, the formation of anode plasma is solely due to deposition of electrons on the anode surface by the process described above. However, the source of cathode plasma also comes from explosive emission from the applied DC electric field, in addition to electron back-bombardment. Diode gap closure leading to shorter microwave pulses from plasma gap closure has been a major problem in magnetrons that operate under long applied voltage pulses. Figure 2-10 is used to describe the flow of anode and cathode plasma for the two cathodes. The red arrows and the blue arrows indicate the direction of flow of anode and cathode plasma, respectively. In a transparent cathode the gaps between the cathode strips allows a larger volume for plasma expansion and therefore one can expect a longer time lapse before the diode gets shorted due to gap closure compared to the solid cathode. Additionally in the case of solid cathode the surface area for plasma production is much greater compared to the transparent cathode. As the electrons move from the cathode to the anode, the DC electric field delivers its potential energy to the RF fields. Unfavorably phased electrons extract energy from the RF field and rapidly return to the cathode. While returned electrons absorb RF energy, they do so only for a short time and dissipate this energy to the cathode, inducing the emission of secondary electrons.

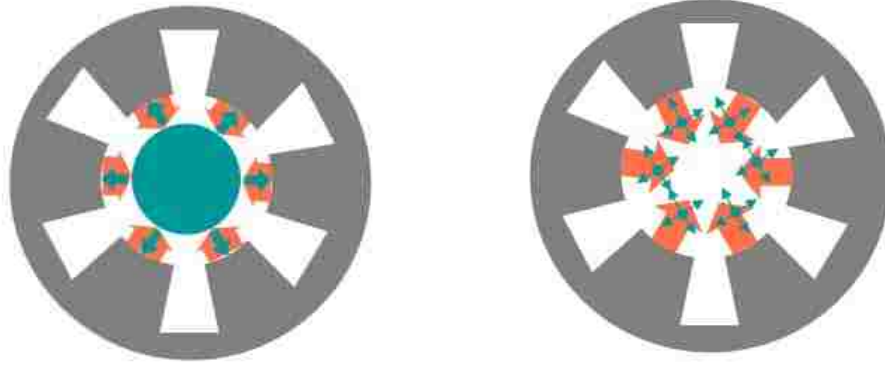


Figure 2-10 Plasma flow in magnetron with solid cathode (left) and transparent cathode (right).

## 2.7 Efficiency Estimate of a Magnetron

According to Fig. 2-2, electrons in the center plane of the bunch do not change their longitudinal velocities in the process of interaction with an RF field and move to the anode [4]. Here we assume that all electrons of the beam have bunched in the retarded phase (favorable phase of the RF fields). The electrons begin moving from cathode surface, where they have energy  $e_o U x_o = e_o (U_a/d) x_o$ . If the electron bunches in the process of interaction approach the anode, the kinetic energy of all electrons at the anode is the same. But if the electrons arrive at the anode moving in the dc electric field, their kinetic energy is  $e_o U_a$ . The energy difference

$$\Delta W = e_o U_a - e_o U_a \left( 1 - \frac{x_o}{d} \right), \quad (2-7-1)$$

transfers to the electromagnetic field. Thus, the electronic efficiency is

$$\eta_e = \frac{\Delta W}{e_o U_a} = 1 - \frac{x_o}{d}. \quad (2-7-2)$$

There is an efficiency penalty at high voltages characteristic of relativistic magnetrons [2]. At high RF voltages, electrons often make their way to the anode in only a few cycles, and in consequence gain radial kinetic energy, thus limiting efficiency. Under the same conditions, back-bombardment of the cathode is enhanced.

## Chapter 3

### Simulation Results

The A6 magnetron geometry and its basic features of operation, including natural mode of oscillation and dispersion characteristics, will be discussed followed by simulation results. To gain confidence that simulation results are representative of experiment we first attempted to reproduce the results of Palevsky [7] numerically. Once the basic trends of magnetron operation were confirmed we then proceeded to compare magnetron performance with the solid and transparent cathodes. The effect of rise-time voltage pulse compared to the characteristic filling time cavities ( $Q/\omega$ ) with the electromagnetic energy of the mode of interest was explored. Finally, simulations were performed with the voltage characteristics of the SINUS-6 electron beam accelerator to compare with the experimental results.

#### 3.1 The A6 Magnetron

The A6 magnetron is the most successful and most studied relativistic magnetron invented at MIT by George Bekefi et al. [2, 7]. The resonant system of the A6 magnetron consists of six identical sectoral cavities of angular width  $20^\circ$ , an axial length 7.2 cm, anode radius  $r_a = 2.11$  cm cavity radius  $r_{\text{cav}} = 4.11$  cm, and radius of the solid cathode  $r_c = 1.58$  cm. Figure 3-1 is a cross section of the A6 magnetron in the  $r-\theta$  plane at a  $z$  location corresponding to the axial center of the tube. Figures 3-2 and 3-3 show the cross-sections of the magnetron in the  $r-z$  planes taken at the azimuthal center of the cavity and the vane, respectively.

For the A6 magnetron the quantity  $d/r_a \approx 0.25$  and the geometry approaches that of the so called planar magnetron, where  $d$  is the A-K gap and  $r_a$  is the anode radius. The gap dimension is very critical in the design of magnetrons as it determines the RF electric field configuration which is particularly sensitive to the A-K gap.

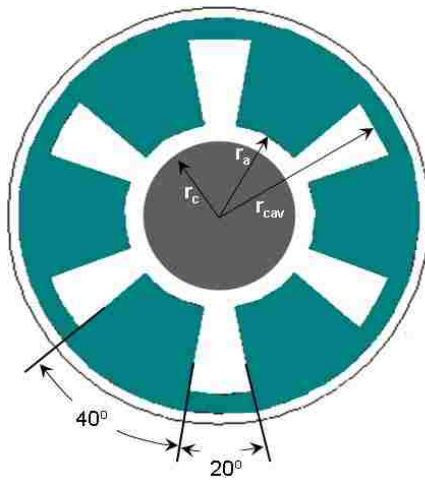


Figure 3-1 The A6 magnetron geometry in the  $r$ - $\theta$  plane.

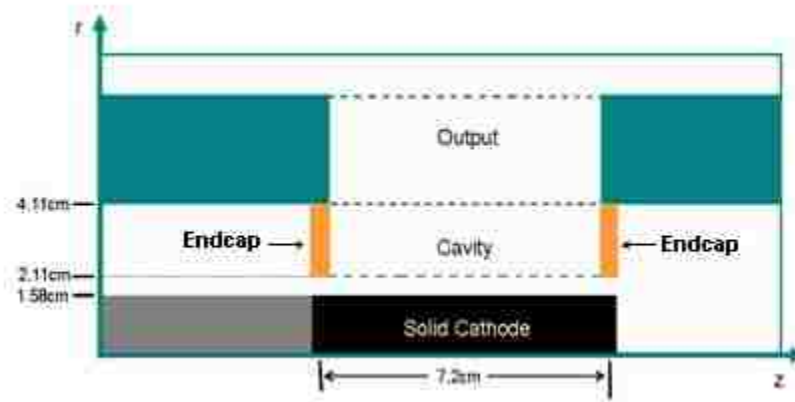


Figure 3-2 The A6 magnetron geometry in the  $r$ - $z$  plane taken at the azimuthal center of the cavity.

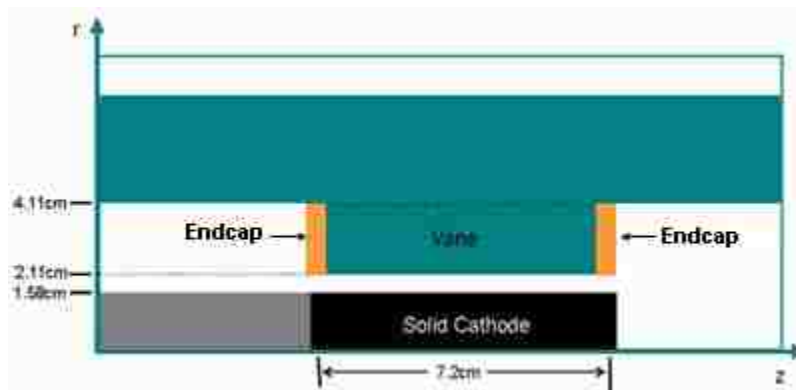


Figure 3-3 The A6 magnetron geometry in the  $r$ - $z$  plane taken at the azimuthal center of the vane.

### **3.2 Endcaps**

A magnetron is a three-dimensional object, and therefore axial modes associated with the finite length  $L$  of the resonator system may exist [2, 7, 35]. The frequencies of these axial modes depend sensitively on boundary conditions at the ends of the anode block such as whether the ends are electrically open or closed and are given by

$$\left(f_n^l\right)^2 = f_n^2 + \left(\frac{lc}{4L}\right)^2, \quad l = 0, 1, 2, \dots \quad (3-2-1)$$

where  $L$  is the resonator length. If end-caps are not employed, the effective length of the resonator is  $L_{eff} \approx 1.2 L$ .

When the anode has endcaps as indicated in Figs. 3-2 and 3-3, the nodes in electric field are well defined. With open ends antinodes do not always coincide with the end of the anode, and their position depends on the proximity of other metal surfaces. This condition may lead to axial mode competition. Work reported in [7, 35, 36] have shown distinctive improvement in microwave output powers with the anode block terminated at both ends with annular endcaps. Based on the successes of these reports the endcap configuration was adopted in this research.

### **3.3 The RF Field Configuration in the A6 Magnetron**

Most conventional magnetrons are designed to oscillate in  $\pi$ -mode ( $n = 3$ ). For this mode the RF electric fields in adjacent resonators are  $180^\circ$  out-of-phase with one another. The A6 magnetron oscillates preferentially in the  $2\pi$  mode ( $n= 6$ ), which is characterized by the fact that the RF fields of all resonators are precisely in phase.

Whether or not a given mode is conducive to strong spoke formation and thus to efficient magnetron operation depends on both the radial and azimuthal field components [2, 7]. The differences in the field configurations of a given mode  $n$  in the relativistic magnetron and a conventional magnetron come from the differences in the gap widths  $d$ . The reason the A6 magnetron favors the  $2\pi$ -mode compared to the  $\pi$ -mode is explained

in [7] and is based on the RF field configuration of the  $\pi$  and the  $2\pi$ -modes shown in Fig. 3-4.

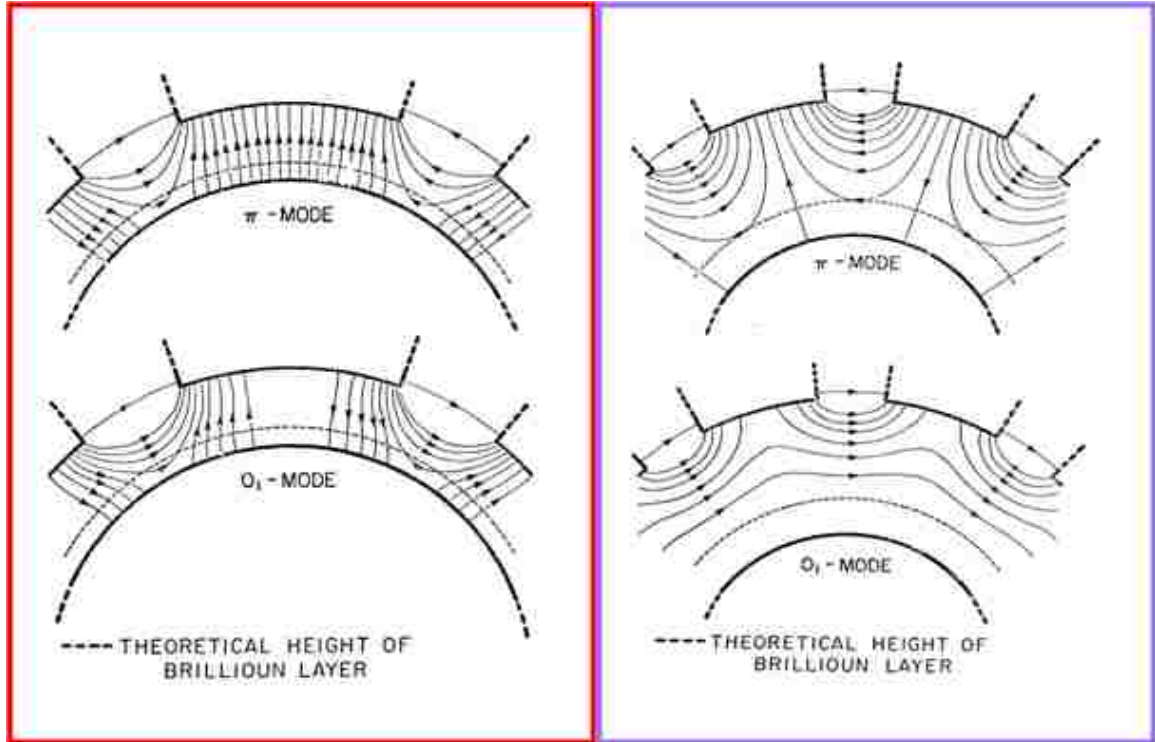


**Figure 3-4 RF electric field for A6 magnetron for narrow A-K gap (left), for large A-K gap (right) [7].**

Figure 3-4 represents the electric field lines of  $n = 3$  ( $\pi$ -mode) and  $n = 6$  ( $2\pi$ -mode). According to [7] spoke formation requires an “equal mix” of radial and azimuthal field components. Hence from Fig. 3-4 it can be inferred that the likelihood of spoke formation for the  $2\pi$ -mode is greater than the  $\pi$ -mode for a narrow A-K gap while for large A-K gaps the condition for spoke formation is more defined for the  $\pi$ -mode.

### 3.4 A6 Magnetron Dispersion Characteristics

The annular interaction space  $d = r_a - r_c$  together with the periodically spaced cavities can be viewed as a coaxial microwave resonator of complicated geometrical cross section, or can be viewed as a coaxial transmission line operating at a frequency equal to the cutoff frequency. The modes of interest which this resonator supports belong to the family of transverse electric modes (TE modes), with the RF magnetic field lying entirely along the z-axis. The method to compute the frequencies of the natural modes of oscillation is outlined in [6]. Figure 3-5 shows the dispersion diagram of the A6 magnetron of Palevsky [7, 30]. Displayed on the same figure are the values of frequencies and their associated mode numbers obtained from a hot test for an A6 magnetron driven with a transparent cathode.

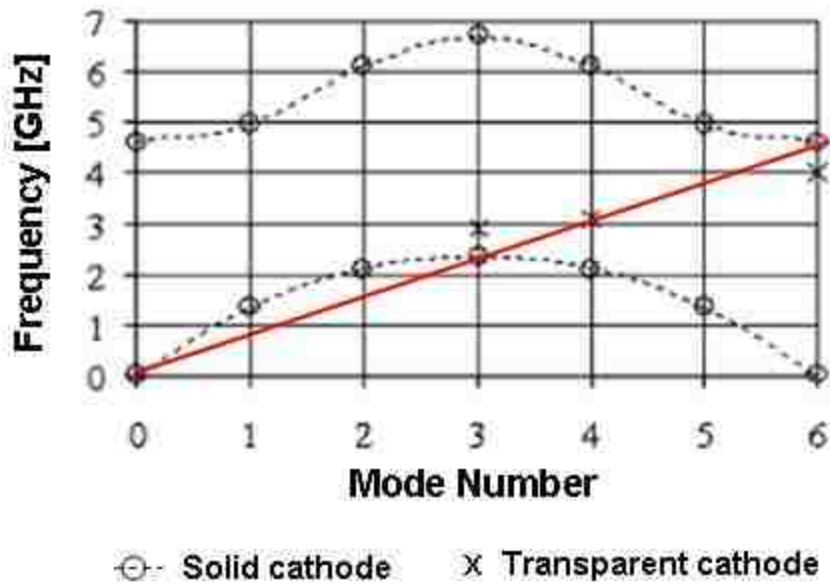


Figure 3-5 Dispersion diagram for the A6 magnetron using a solid cathode and transparent cathode [31].

One period of the first two passbands is shown. Symbols mark the discrete oscillation frequencies supported by the A6 magnetron. Oscillations can occur when a beam line intersects a TE mode. The lowest order frequencies peak at the  $\pi$ -mode, and all other modes are twofold and therefore degenerate [3, 4]. One might expect the lowest frequency  $\pi$  mode to dominate; however, the A6 magnetron oscillates in the  $2\pi$ -mode. Note that the phase velocity of a mode is given by the slope of a straight line drawn from the origin, given in units of segments per second [5, 36]. By a coincidence of design, the  $\pi$  and the  $2\pi$ -modes for the A6 magnetron have the same phase velocity. A qualitative explanation on why the narrow A-K gap magnetron would oscillate in the  $2\pi$ -mode has been described in the preceding section.

The B-H curves for the solid and the transparent cathode were drawn based on the frequency information acquired from the MAGIC simulations and are shown in Figs. 3-6 and 3-7, respectively. Note that the B-H lines for the  $\pi$  and the  $2\pi$  modes overlap. This is because the  $\pi$ -mode frequency is exactly twice that of the  $2\pi$ -mode. This can give rise to mode competition between the  $\pi$  and the  $2\pi$ -modes and lead to overall deterioration in the performance of the magnetron, which can also be inferred from the dispersion diagram in Fig. 3-5. The frequencies for the  $\pi$  and the  $2\pi$  modes are well separated in the case of the transparent cathode, thereby lowering the chances of mode competition between them.

Hitherto, the general features of the A6 magnetron have been discussed. In the following sections the simulation setup and results will be presented.



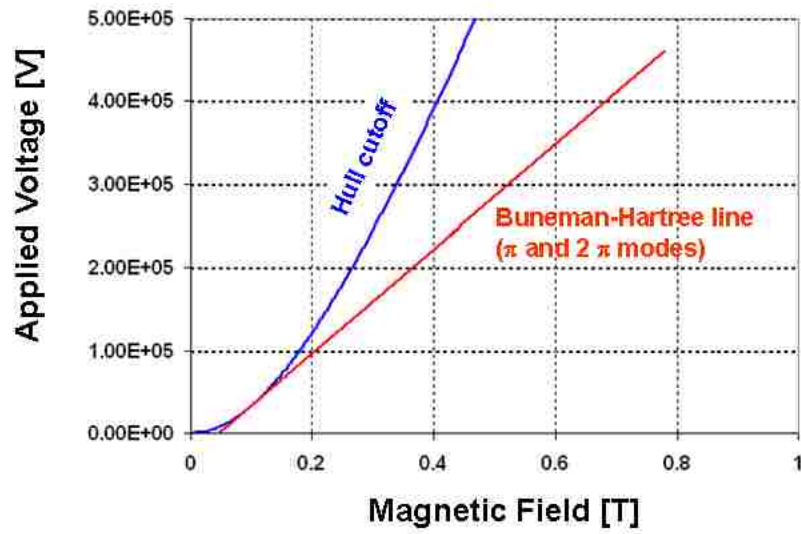


Figure 3-6 B-H and the Hull cutoff curves for the A6 magnetron with solid cathode.

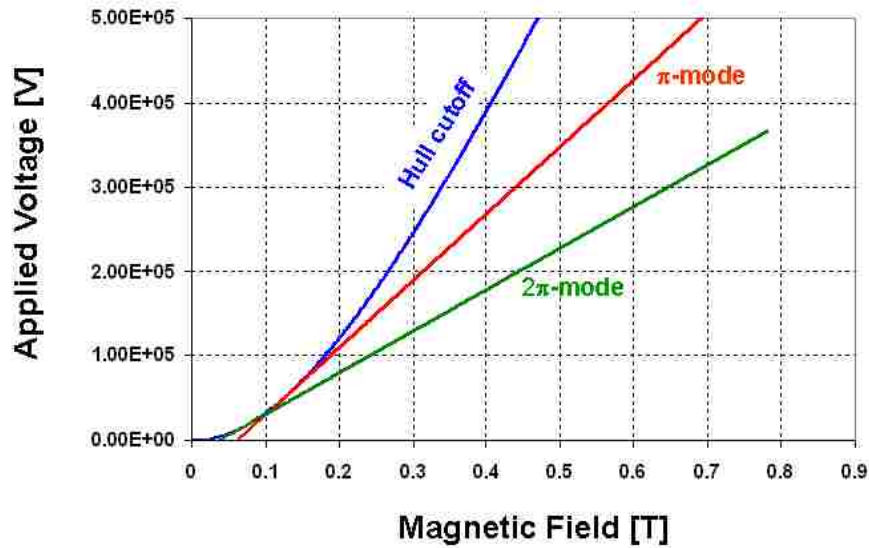


Figure 1-7 B-H and the Hull cutoff curves for the A6 magnetron with transparent cathode.

### **3.5 Description of MAGIC and Simulation Setup**

To demonstrate the advantages of the transparent cathode over the solid cathode in magnetrons we use the three-dimensional fully electromagnetic and fully relativistic PIC code MAGIC for computer simulations of the A6 magnetron [37]. MAGIC calculates the interaction between charged particles and electromagnetic fields as they evolve in time and space from some defined initial configuration. The numerical calculation uses the finite-difference method in which time and three dimensional space are divided into finite grids. From some known initial state, time is advanced by adding a single time step. At each new value of time, Maxwell's equations are solved throughout the space to advance the electromagnetic fields in time. Using this new field the Lorentz equation is solved to advance the momenta and coordinates of all charged particles in the simulation. The continuity equation is solved to map charge and current densities onto the grid, which are then used as sources for Maxwell's equations onto the next time step. This provides the self-consistent interaction between the fields and particles.

The fidelity of the simulation result is highly dependent on the gridding that is used to divide the simulation volume. As a general rule the finer the grid the better the accuracy of the simulation results. However, associated with high grid resolution are cost and time. One of the most attractive features of MAGIC is that it allows adaptive meshing, a scheme used for increasing the cell resolution in the area or volume of simulation where the important physics takes place.

**Table 3.1 Spatial grid resolution of the interaction space**

<b>Quantity</b>	<b>Dimension</b>
Radial grid resolution	0.5 mm
Axial grid resolution	10 mm
Azimuthal grid resolution	5 degrees
Time step	95 ps

The magnetron interaction space was divided according to the parameters in Table 3.1. A finer radial grid was chosen since the main physics occurs in the radial direction. There were  $\sim 400,000$  active particles present during the course of the simulation.

The simulation model is shown in Figs. 3-1 to 3-3. Power is fed to the magnetron by injecting a voltage wave at the inlet via a short coaxial transmission line section. The associated wave current depends on the impedance of the magnetron load. The applied voltage was kept constant at the load during the B-field scan by using the “CIRCUIT” option in MAGIC, which has an equivalent effect as that of a ballast resistor. The B\_STATIC option for defining the applied axial magnetic field assumed a uniform value throughout the simulation volume. Electron emission at the cathode surface occurred when the normal electric field reached a specified value of 100 kV/cm. One cavity of the anode block is open for power extraction and an iris is used to obtain maximum power. Power is radiated through an outlet whose impedance is matched to the expected mode of oscillation. The input voltage, anode current, leakage current, microwave power and frequency were measured for each simulation run.

As the first step Palevsky’s experimental work was reproduced numerically for ascertaining the fidelity of results obtained from MAGIC simulations. The applied voltage pulse used for these simulations reached an amplitude of 350 kV from zero to 10 ns after which it maintained a flat-top for a duration of 40 ns.

The initial A6 simulations conducted with a solid cathode replicated Palevsky’s experimental results [7]. The frequency of oscillation was measured to be 4.6 GHz and the mode of oscillation was identified to be an  $2\pi$ -mode from the particle phase-space plot. Comparable output powers were also measured. This reassured the fidelity of the MAGIC simulations.

Next, the solid cathode was replaced with the transparent cathode and the magnetron performance was compared for the two cathodes.

### **3.6 Comparison of the Solid Cathode and the Transparent Cathode for Palevsky’s A6 Magnetron Setup**

The initial comparison of the solid cathode and transparent cathode were conducted on the A6 magnetron geometry using a voltage pulse with 10 ns rise-time. In the section to follow the performance of the two cathodes will be made with a 1 ns voltage rise-time pulse. Here, the phrase “Palevsky’s A6 magnetron setup” is used to distinguish the two voltage rise-times.

The structure of the transparent cathode is such that it allows various combinations of the number of strips, angular width of the strips, and their azimuthal orientation. Therefore, prior to comparing the results of the solid cathode with the transparent cathode we had to optimize these parameters. It was found from the simulations that the optimal azimuthal orientation of the strips are a position placed slightly off-center with respect to the anode structure, as illustrated in Fig. 3-8. As for the number of strips, 6 cathode strips are ideal because it would favor the formation of 6 spokes, which corresponds to the  $2\pi$ -mode. The results obtained after the optimization of these parameters were then compared with the results obtained from the solid cathode.

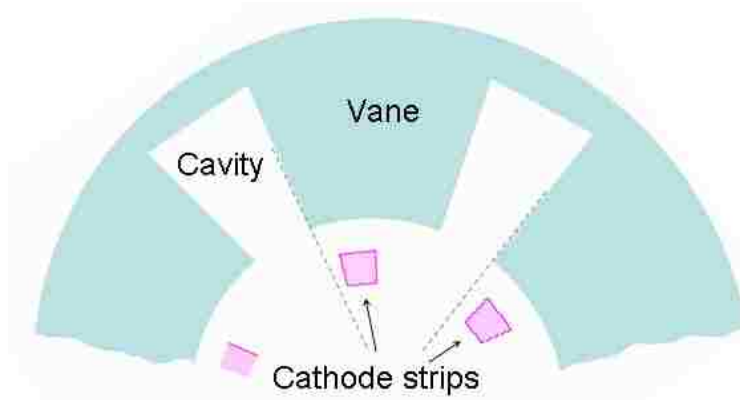


**Figure 3-8 Off-center placement of the cathode strips.**

Figure 3-9 shows the progress in spoke formation as a function of time, which indicates the build-up of RF signal. As shown in Fig. 3-9, visible bunching associated with RF current, i.e. spoke formation, around a solid cathode occurs only around 15 ns and the six-fold modulation of the electron sheath, which corresponds to the  $2\pi$ -mode forms around 20 ns (not shown in the diagram). On the other hand, the 6-fold symmetry of the electron sheath is completely formed in the case of the transparent cathode at least three times faster than the solid cathode. Figure 3-10 clearly shows fast start and growth of oscillations. The microwave signal saturates around 14 ns in the case of the transparent cathode, while it reaches its peak value after 40 ns in the case of the solid cathode. Figure 3-11 shows microwave power as a function of axial magnetic field. From the results it is apparent that transparent cathode was capable of delivering higher output powers compared to the solid cathode.

The preliminary MAGIC simulations confirmed the consistency of the theory of operation of the transparent cathode by showing fast start and rate of build-up of oscillations with an added benefit of delivering higher output powers.

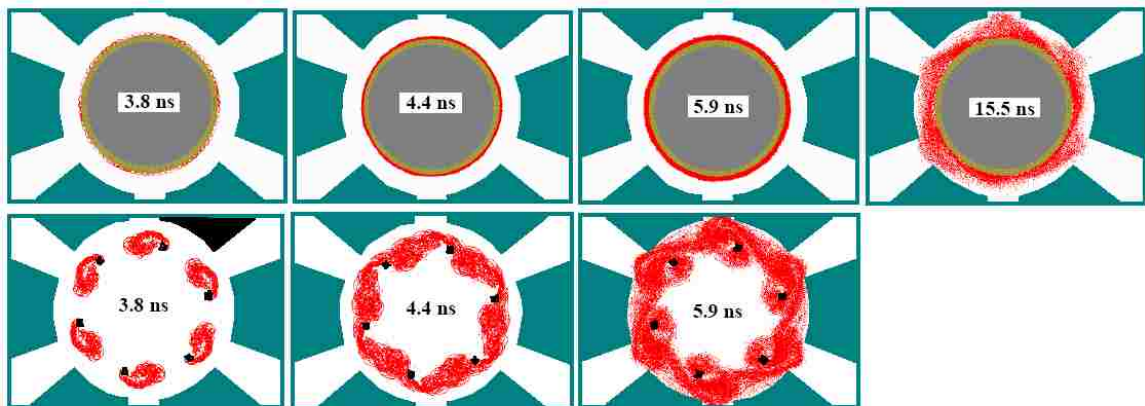


**Figure 3-9 Progress in the formation of spokes for Solid Cathode (top), Transparent Cathode (bottom).**

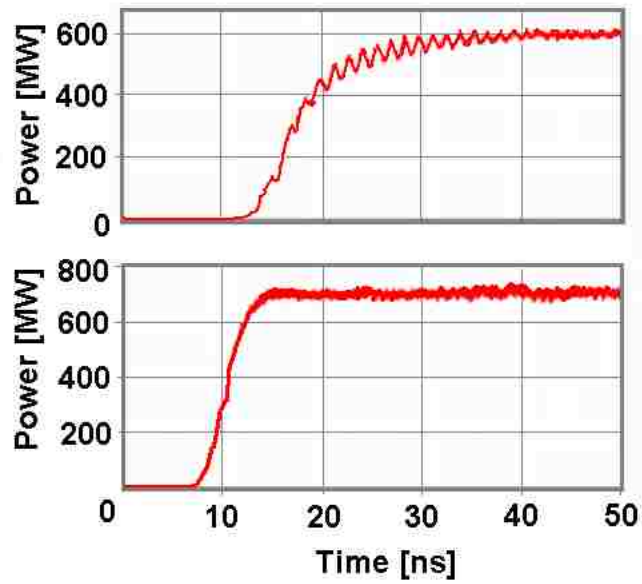


Figure 3-10 Output power for the Solid Cathode (top) and Transparent Cathode (bottom).

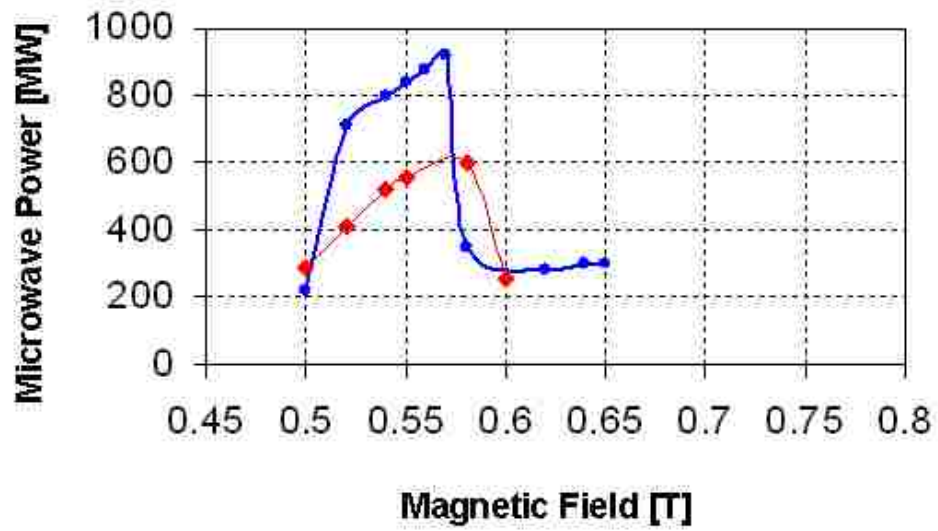
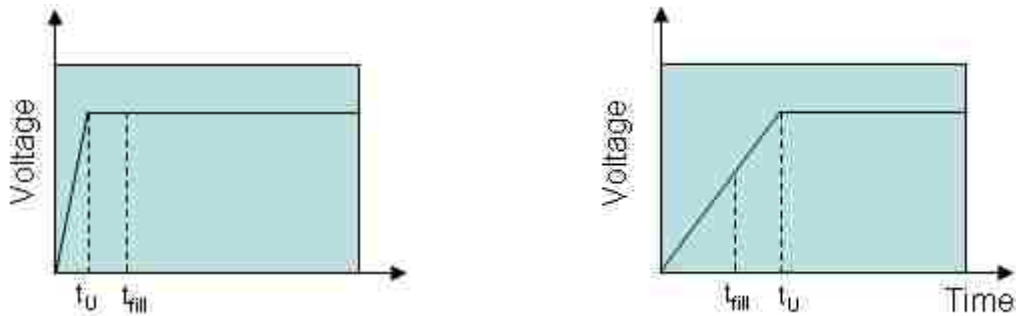


Figure 3-11 Microwave output power dependence on applied magnetic field.

### 3.7 Effect of voltage Rise Time on Magnetron Output Characteristics

In this section the effect of voltage rise-time on magnetron output will be explored. The self-excitation of oscillations in resonant microwave sources strongly depends on the relation between the cavity fill-time  $t_{fill}$  of the  $n$ th mode, and the voltage rise time  $t_U$  [18] or, more precisely, on the time of increasing azimuthal electron drift velocity as the voltage grows. From our hot tests,  $t_{fill} \approx 4 - 5$  ns for the  $\pi$ -mode and the  $2\pi$ -mode. These numbers agree with the results published in [7]. We have studied the following two cases: 1) instant turn-on and 2) slow turn-on.



**Figure 3-12 (Left) Instant turn-on:  $t_U < t_s$  ; (Right) Slow turn-on:  $t_U > t_s$ .**

The case of instant turn on implies that the rise-time of the electron beam reaches its nominal value practically instantly. For slow turn-on, however, there is sufficient time for modes with lower phase velocity to develop once their B-H thresholds are exceeded during the voltage rise. This may lead to mode competition or, at least, slower start-of-oscillations of the operating mode owing to the reforming of electron spokes.

Simulations were performed with a 350 kV, 1 ns rise-time voltage pulse on the A6 magnetron for the two cathodes and the results are presented in Fig. 3-13.

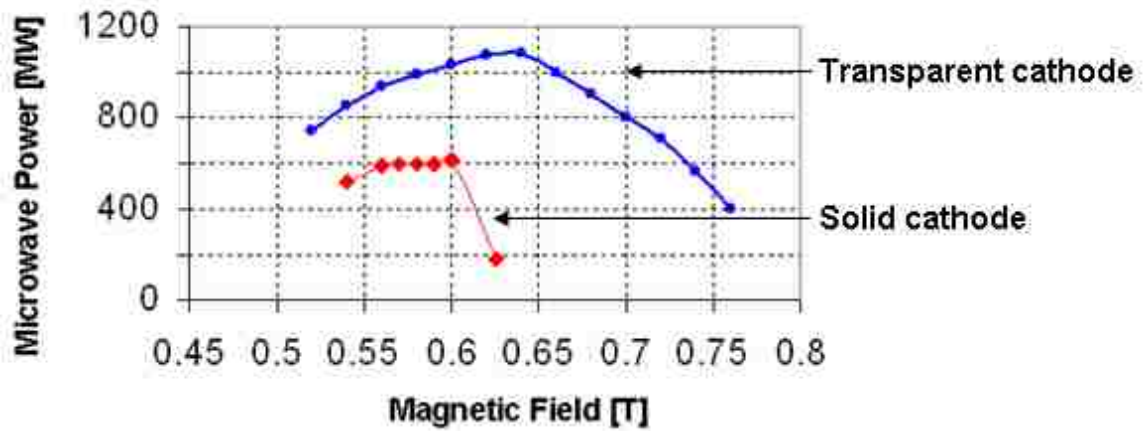


Figure 3-13 Magnetic field dependence on microwave output power with an applied voltage of rise time 1ns.

Figure 3-13 shows the microwave output power as a function of magnetic field for the two cathodes. All the points on the curves correspond to magnetron oscillation in  $2\pi$ -mode. The transparent cathode shows overall higher output powers compared to the solid cathode with the peak power exceeding 1 GW at the optimal magnetic field. Furthermore, oscillations in the  $2\pi$ -mode occur over a wider range of magnetic for the transparent cathode. Comparing these results with Fig. 3-11 it is apparent that the transparent cathode is ideal for voltage rise-times that satisfy the condition for instant turn-on. The solid cathode showed no significant improvement in magnetron performance for either voltage pulse.

The effect of longer voltage rise-times was also studied. The results of the magnetron behavior for different rise times are summarized in Fig. 3-14. A clear transition from  $2\pi$ -mode to  $\pi$ -mode is seen as one goes from shorter to longer voltage rise times in case of the transparent cathode. It must be mentioned that more power was extracted from the  $2\pi$ -mode than the  $\pi$ -mode as has been in reported in [7, 35, 36]. For very long rise times, that is  $t_U > 50$  ns, application of both solid cathode and transparent cathode lead to generation of only the  $4\pi/3$ -mode, which is of no interest to magnetrons with asymmetric extraction.



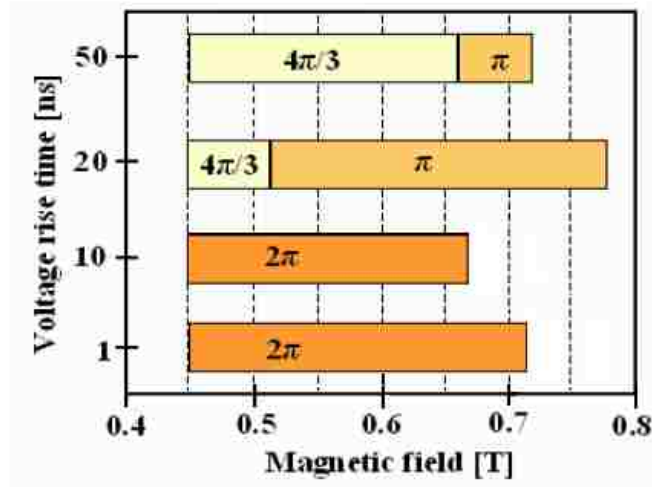
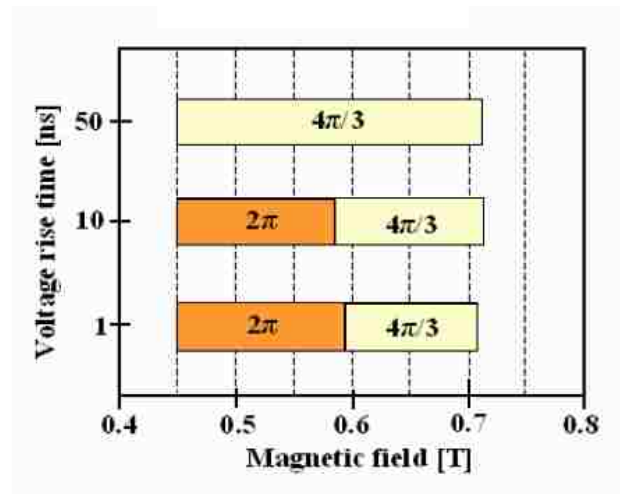


Figure 3-14 Appearance of stable operating modes in the A6 magnetron with Solid Cathode (top) and Transparent Cathode (bottom).

The poor performance of both cathodes in the slow turn-on regime is most likely due to sufficient time being available for lower phase velocity modes to develop. As discussed in Chapter 2, the source of electrons in relativistic magnetrons is explosive emission. The transparent cathode may still be a suitable candidate in magnetrons with long voltage rise-times if the electron emission process were somehow controlled so that the electrons would only be emitted when the electric field reached a satisfactory level that would favor the operating mode.

### 3.8 Heuristic Explanations for the Behaviour Depicted by the Transparent Cathode

This section presents qualitative explanations for the behavior exhibited by the transparent cathode. Possible reasons for the optimal positioning of the cathode strips and higher output powers extracted from the transparent cathode will be discussed.

In order to explain the effectiveness of the transparent cathode design, the initial startup phase and oscillatory phase of the RF pulse will be studied separately. DC priming and RF priming each play equally important roles in the magnetron oscillation process. However, the DC priming effect is dominant in the start-up phase while in the oscillatory phase the most general and important aspect in play is the coordination of both DC and RF priming with the established  $E \times B$  direction of flow to position electron bunches into favorable phases.

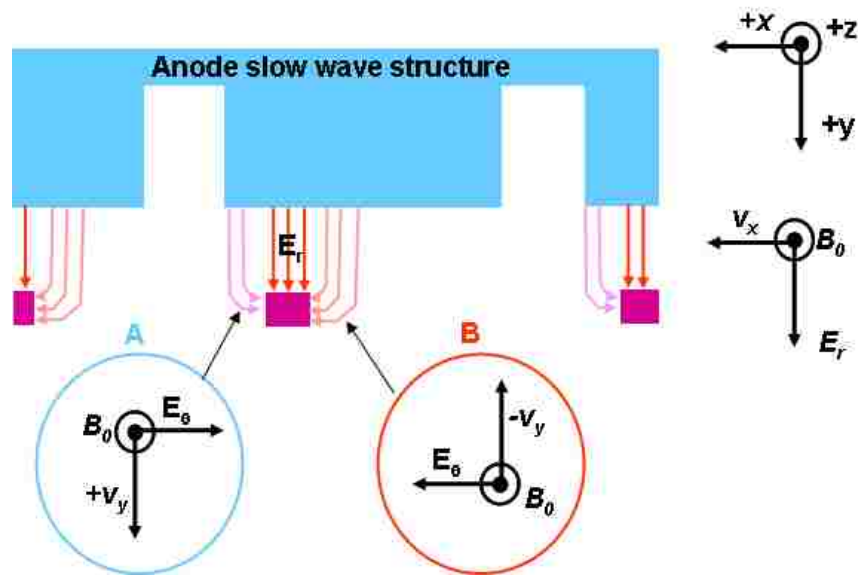


Figure 3-15 Direction of DC electric field around the cathode strip at its optimal position.

### **3.8.1 Startup Phase**

The startup phase is most influenced by two forms of DC priming, cathode priming and electrostatic priming, and each of these types of priming contributes to the launching of well-formed bunches into the zeroth-order ExB drift. As previously discussed, cathode priming results from bunched emission from the discrete size of each cathode strip. Electrostatic priming, as illustrated in Fig. 3-15, establishes two different zeroth-order ExB drifts that also contribute to the formation of electron bunches. On the left side of the indicated cathode strip, ExB drift is established downward, while the strip's right side creates an upward drift. The electric field is comparatively stronger in region B than in region A; hence, more electrons would be pushed into the interaction space by the drift in region B than pushed away from the interaction space in region A. Thus the cathode priming and the DC electrostatic priming ensure a constant supply of bunched electrons into the interaction space. Once the drift of these bunches satisfies the synchronous condition ( $v_{ph} \approx v_{drift}$ ) the electron trajectories should be such that they fall in the favorable phase of the RF fields so that RF priming could take place efficiently. The combination of all of these effects results in almost instantaneous startup of and establishment of high growth rate of a particular RF mode.

### **3.8.2 Oscillatory Phase**

During the steady-state oscillatory phase of the RF pulse, the transparent cathode design causes RF and DC priming effects responsible for high power performance. These can be best illustrated in Figs. 3-16 and 3-17, which both show electron plots for the  $2\pi$  mode during different times of the RF cycle. The top diagram illustrates RF field distribution in the favorable phase, and the bottom indicates positioning in the unfavorable phase. In the favorable phase (Fig. 3-16), the azimuthal orientation of the strips should be such that the electron bunches would drift in the favorable phase of the RF fields via combined RF and DC ExB drifts, efficiently losing their energy to the RF field. In the unfavorable phase (Fig. 3-17), the RF field distribution is such that it bunches electrons. There is a marked difference in the performance of the solid vs. the transparent

cathode during this phase. Whereas the solid cathode provides a large surface for electron collision, producing secondary electrons or energy loss to heating, the transparent cathode has smaller collision surface in regions where electrons move down in the radial direction. The result is that any potential energy that electrons gain at the expense of the RF field is not lost and can be used in the favorable phase to contribute to RF field energy in the next cycle. This may explain the overall higher output powers attained from the transparent cathode.

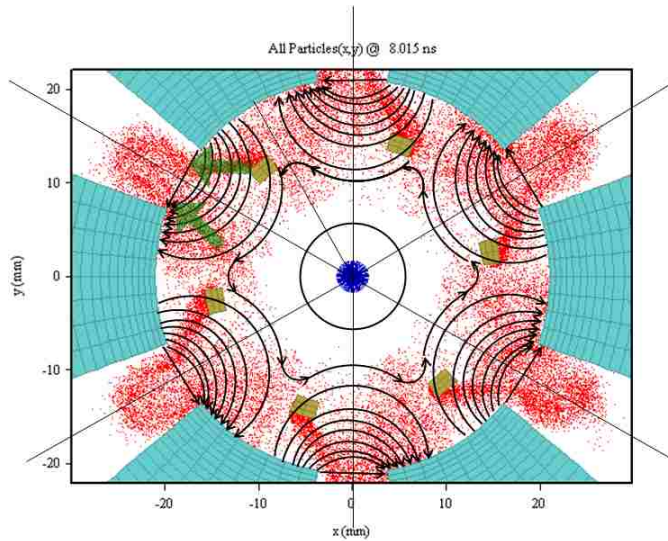


**Figure 3-16 Particle plot and their direction of drift in the favorable phase.**

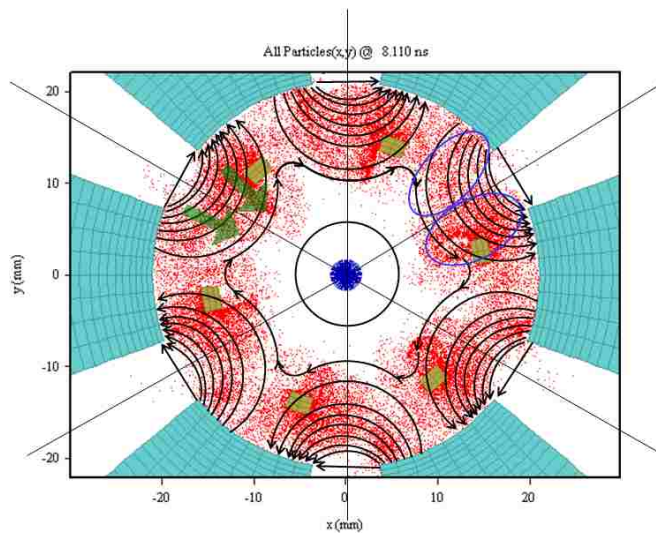


**Figure 3-17 Particle plot and their direction of drift in the unfavorable phase.**

(Solid black contours are a qualitative representation of the RF field for the  $2\pi$ -mode in Figs. 3-16 and 3-17).

### 3.9 Simulations with the SINUS-6 Voltage Waveform

Previous computer simulation results were very impressive and proved that the transparent cathode improves the magnetron output characteristics significantly. The UNM Pulsed Power, Beams, and Microwave Laboratory has two electron beam accelerators. Pulserad 110a is currently being modified to give a 4 ns risetime and 30 ns flat top voltage pulse with a saturation voltage of 350 kV.

The preliminary experiments with the transparent cathode were carried out on the SINUS-6 electron beam accelerator. The SINUS-6 voltage waveform is shown in Fig. 3-18. It has pulse duration of 12 ns and has the basic shape of a half sine wave. The major disadvantage of this type of waveform is that the microwave oscillations would not reach saturation since the voltage shape is constantly changing with time.

Despite this fact MAGIC simulations with a SINUS-6 input pulse have shown that the transparent cathode follows similar trends as the previous simulation results. The results are summarized in Figs. 3-19 to 3-21. Figure 3-19 shows the magnetic field dependence on the microwave output power. These simulations were performed with a 260 kV peak voltage, just under the maximum deliverable power of SINUS-6.

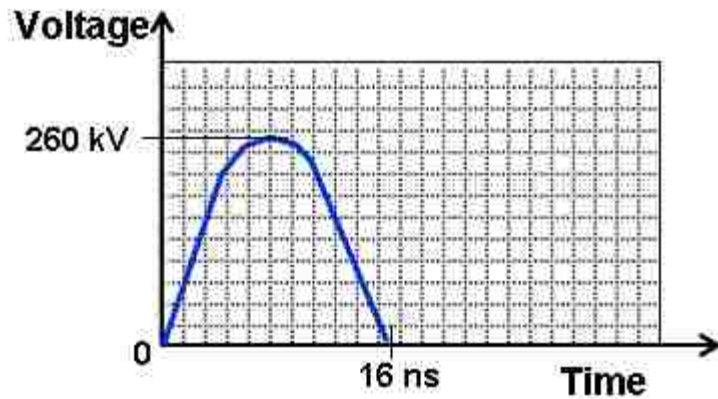


Figure 3-18 The SINUS-6 voltage waveform.

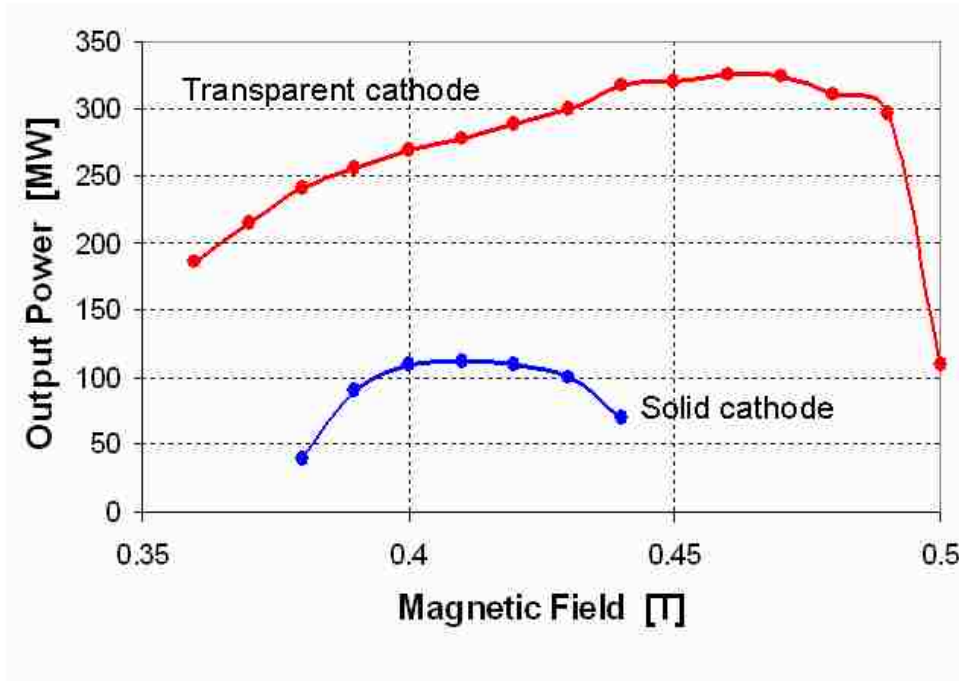


Figure 3-19 Dependence of magnetic field on microwave power.

The transparent cathode delivers higher output powers and oscillates in the  $2\pi$ -mode over a wide range of magnetic field compared to the solid cathode. A maximum power of 320 MW was obtained at 0.47 T from the transparent cathode while a maximum power of 110 MW at 0.41 T was attained from the solid cathode. The microwave pulse and the FFT of the RF signals are shown in Figs 3-20 and 3-21 for the two cathodes at these optimum magnetic field values. The fast start and rate of buildup of oscillation is apparent in Fig. 3-20 for the transparent cathode. Consequently, the total energy in the microwave pulse is higher. While in the solid cathode with the slow start of oscillations there is not enough time for microwave oscillations to reach a high enough value with the SINUS-6-type applied voltage pulse. The FFT signals in Fig. 3-21 show single-frequency operation for the transparent cathode while there is visible mode competition in the case of the solid cathode.

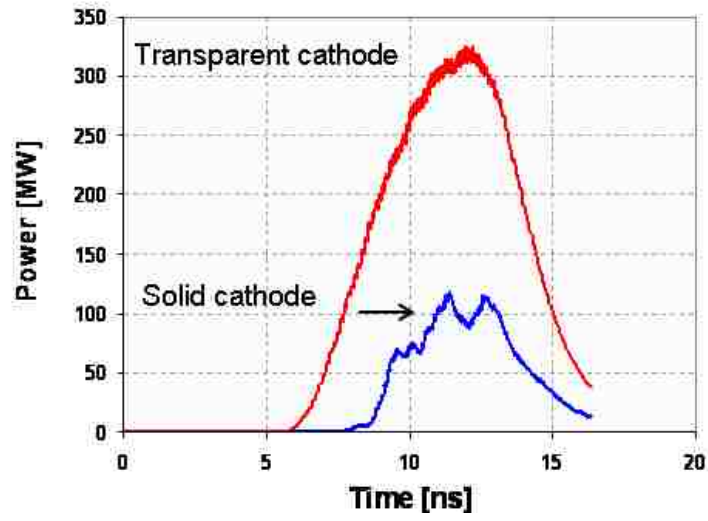


Figure 3-20 Microwave signal obtained at the optimum magnetic field.

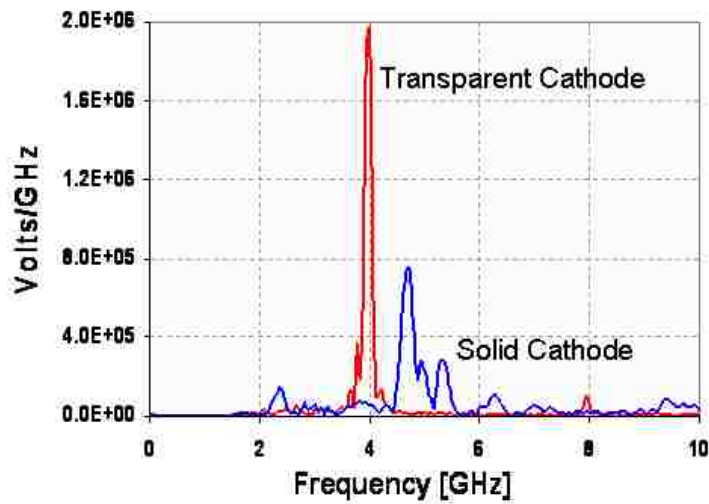


Figure 3-21 The FFT of the RF signal showing single frequency operation for the transparent cathode, while slight mode competition is observed in the case of the solid cathode.

### 3.10 Optimization of Microwave Radial Extraction

Recent studies have shown that magnetron performance is sensitive to the slot of microwave extraction, particularly the microwave output power [38, 39]. Therefore, the angle of extraction of the A6 magnetron with radial extraction was optimized. The initial angle of extraction was  $20^\circ$  and the optimized angle was found to be  $10^\circ$ . The MAGIC simulation results for the two angles are summarized in Fig. 3-22. The results show that the  $10^\circ$  extraction doubles the output power. The magnetron experimental setup utilized the  $10^\circ$  scheme.

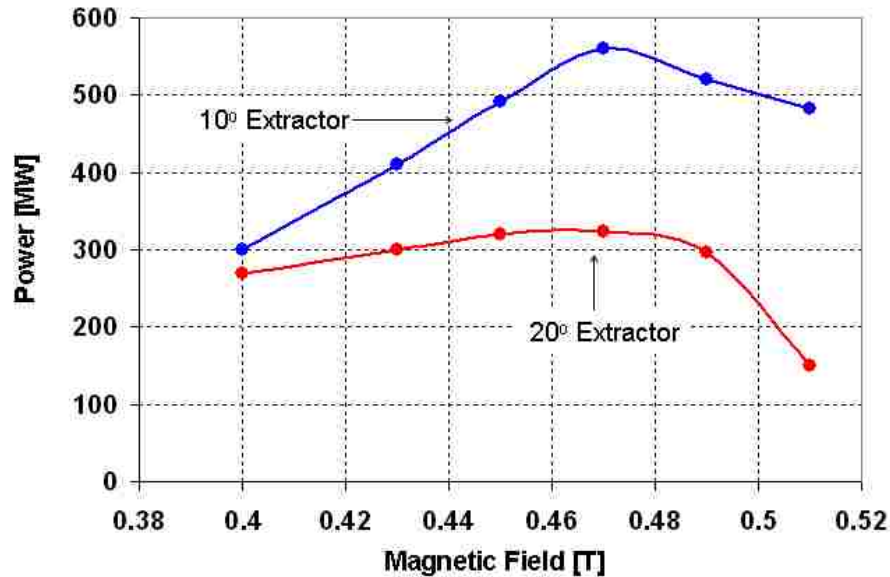


Figure 3-22 Comparison of microwave output power with the  $20^\circ$  extraction and the  $10^\circ$  extraction schemes.

Simulations have shown significant improvement in the output characteristics of a relativistic magnetron driven by a transparent cathode. In the next chapter the experimental setup will be described followed by the experimental results in chapter 5.



## Chapter 4

### Experimental Setup

This chapter describes the experimental setup. It is divided into four main sections. Section I presents the components of the SINUS-6 electron beam accelerator, its control system and an outline of the various modifications made to it in order to conduct magnetron experiments. Section II discusses the engineering required to design a new vacuum chamber including a new oil-vacuum interface. Section III presents the design constraints and requirements for the Helmholtz coils used in the experiments. Finally section IV discusses the load and microwave diagnostics used in the experiments including their physics of operation, construction scheme and calibration procedure.

#### 4.1.1 Description of SINUS-6 Electron Beam Accelerator

The SINUS-6 is a short pulse, high current, relativistic electron beam accelerator at the UNM Pulsed Power, Beams, and Microwaves Laboratory that has been modified to operate in the single-shot regime. Figure 4-1 is a schematic of the SINUS-6 accelerator. It comprises a Tesla transformer, pulse-forming line, a high voltage spark gap switch, transmission line, a magnetically insulated oil-vacuum interface and a cold-cathode vacuum diode [42, 43].

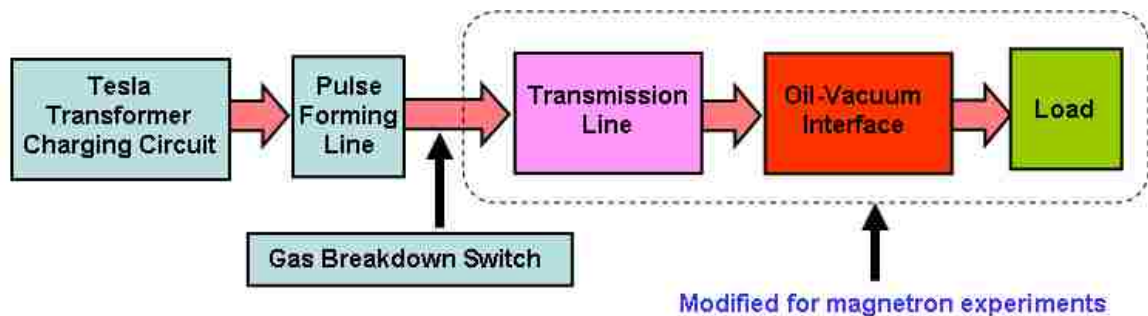
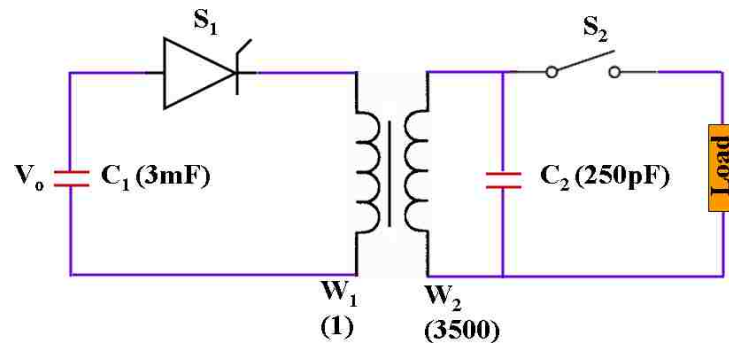


Figure 4-1 Principle elements of the SINUS-6 accelerator.

The main feature in the design of SINUS-6 is the conically formed Tesla transformer. An oil-filled coaxial line with an electrical length of 6 ns serves as the pulse forming line (PFL) and encloses the Tesla transformer. The primary winding of the Tesla transformer is placed on the inner surface of the outer conductor of the coaxial PFL and has a single turn, while a secondary winding is wound on a hollow truncated cone and is electrically connected to the inner conductor of the PFL.

The circuit diagram of the SINUS-6 pulse power system is shown in Fig. 4-2. The elements, S2 and C2 represent the gas breakdown switch and coaxial pulse forming line, respectively. During operation, the primary capacitor C1 is charged to a voltage of less than 300 V. Upon closing the thyristor switch, a voltage pulse is launched onto the single-turn coil W1. This induces a voltage of much higher amplitude in coil W2 (with 3500 turns), which charges C2 [44]. The charging time of the PFL is 60  $\mu$ s. When the self-breakdown gas switch S2 closes a pulse with full width half maximum (FWHM) of 12 ns is launched onto the load via the transmission line.



**Figure 4-2 Equivalent circuit of the SINUS-6 electron beam accelerator.**

The description of circuit elements in Fig. 4-2 are listed below.

$V_0$  – is the primary charge voltage (< 300 V),

$C_1$  – primary store capacitance (3 mF),

$S_1$  – thyristor switch (externally triggered from screen room),

Tesla transformer:  $W_1$  – primary winding (1 turn),  $W_2$  – secondary winding (3500 turns),

$S_2$  – spark gap switch (gas breakdown switch),

$C_2$  – pulse forming line (Capacitance: 250 pF; Electrical length: 6 ns; Impedance: 20  $\Omega$ ).

#### **4.1.2 Modifications Made to the SINUS-6**

The SINUS-6 accelerator at UNM was initially designed and built for an X-band, 100  $\Omega$  backward wave oscillator load (BWO). In order to conduct magnetron experiments on SINUS-6 it had to undergo several modifications listed below. Though SINUS-6 was sufficient for preliminary proof-of-concept magnetron experiments its design and circuit parameters limit the maximum available energy. For this reason the Pulserad 110a (PI 110a) accelerator at the UNM Pulsed Power, Beams, and Microwaves Laboratory is currently being modified so that the magnetron operation could be explored at higher voltages and magnetic fields, and longer pulse lengths.

#### **4.1.3 The Transmission Line**

The transmission line initially installed on SINUS-6 has a tapered-impedance construction in which a tapered inner conductor matches the 20  $\Omega$  PFL to the 100  $\Omega$  BWO load. The operational impedance of the A6 magnetron, to be tested, being 20  $\Omega$  was a complete coincidence. Therefore, matching of the PFL to the magnetron was easily accomplished by simply replacing the tapered inner conductor with a new inner conductor of uniform radius. SINUS-6 is capable of delivering a maximum power of 4.2 GW onto a matched load. After the replacement of the transmission line a maximum deliverable current of 14 kA is expected in a matched 20  $\Omega$  load with a beam voltage of 300 kV. Because of power limitations magnetron experiments were conducted at 260 kV.

#### **4.1.4 Pulsed Magnetic Field Producing System**

A new magnetic field-producing system had to be designed and built since the original SINUS-6 solenoid system could not meet the magnetic field requirements of the A6 magnetron. Details on the coil design procedure are presented in Section 4.2. The new magnets are a pair of Helmholtz coils designed to provide a maximum magnetic field of 1 T.

A discharge switch assembly consisting of a stack of SCR's and diodes was used to discharge the energy stored in the capacitor bank into the coils. Even though the pulsed power circuit allows the charging of capacitors up to 4 kV, the SCR's in the circuit are rated at 2.9 kV, thus, limiting the maximum charging voltage of the capacitors. The original SINUS-6 pulsed magnetic circuit consisted of a parallel arrangement of 6 90  $\mu$ F capacitors. The maximum capacitive energy available from this circuit of 3.24 kJ could not be converted into sufficient magnetic field for the magnetron experiments. The initial capacitors were replaced with two 500  $\mu$ F capacitors with voltage rating of 10 kV. This upgrade allowed a maximum magnetic field of 0.68 T, which was sufficient for the preliminary magnetron experiments.

#### **4.1.5 Vacuum Chamber**

Modifying the output impedance of the accelerator demanded the replacement of the vacuum chamber. A new vacuum chamber including a new oil-vacuum interface was designed and built. The new vacuum chamber was designed and manufactured in such a way that it could be used on both the SINUS-6 and the Pulserad 110a accelerators. One of the distinctive features of the Pulserad 110a is that it implements a fast oil-breakdown switch that will permit a voltage rise-time of 4 ns on to a matched load of 20  $\Omega$ . (The importance of voltage rise-time on magnetron operation has been explained in chapter 3). Thus, to maintain the fast voltage rise-time inductance in the section had to be minimized. The details are elucidated in section 4.3.

#### **4.1.6 Load Diagnostics**

Voltage measurements in pulse power systems must be performed in regions that are free from space charge. The original voltage measurement on SINUS-6 was made with a capacitive divider probe located in the oil-section before the transition to the vacuum section for this reason. It had to be recalibrated because of the change of transmission line dimensions. The calibration procedure is outlined in section 4.4.2.

Two new self-integrating Rogowski coils were built for current measurements in the magnetron experiments. The basic design, construction, concept of operation, and calibration procedure can be found in section 4.4.3. Figures 4-3 and 4-4 show the basic elements of the SINUS-6 before and after modification.

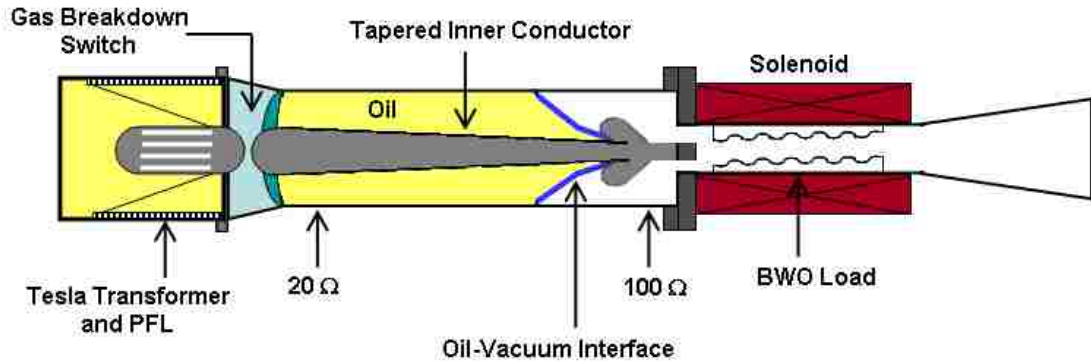


Figure 4-3 Schematic of the SINUS-6 electron beam accelerator before modification.

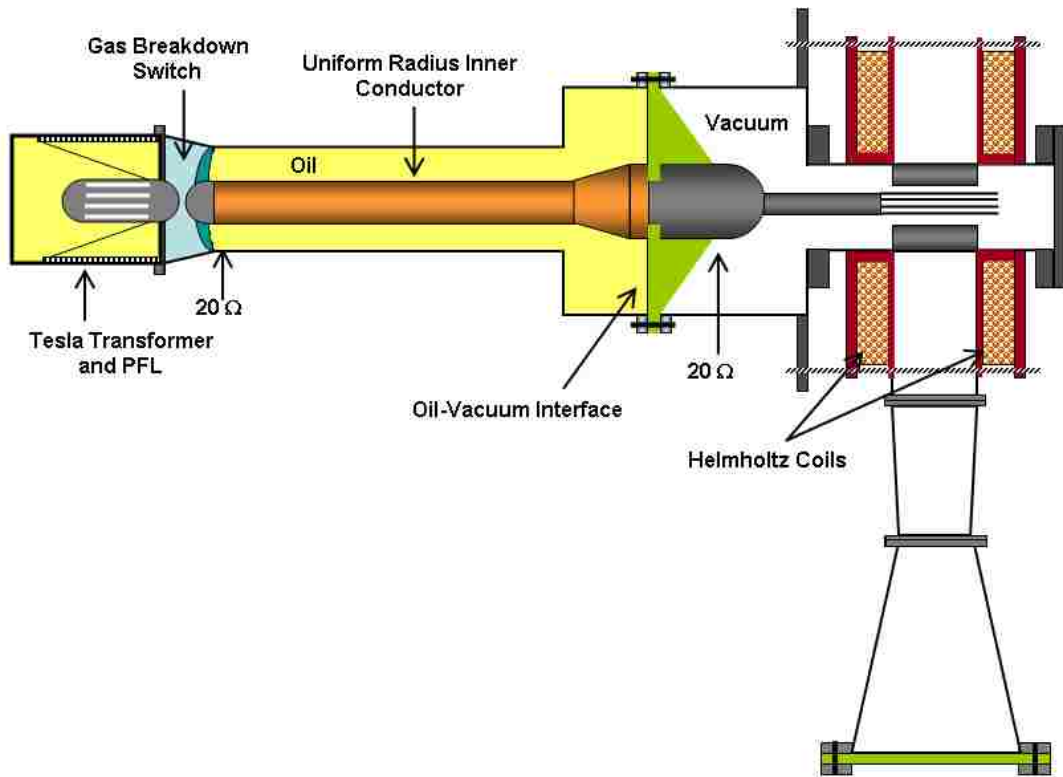


Figure 4-4 Schematic of the SINUS-6 electron beam accelerator after modification.

#### **4.1.7 SINUS-6 Control System**

A schematic of the control system is presented in Fig. 4-5. Two Russian (Computer Automated Measurement and Control) CAMAC-compatible units MFMS2 and FI were used for accelerator hardware control. Both of these units are located in the control box shown in Fig. 4-5. The trigger pulses generated by these units have signal amplitude and duration of 10  $\mu$ s, 10 V and 15  $\mu$ s, 150 V, respectively.

The initiation of the trigger pulses is accomplished by a Labview program. Four trigger signals are generated for setting the charge voltage of the capacitor banks, charging and discharging the capacitors and firing the accelerator. Each of these signals were controlled by ports S1, S3, C1 and C2 on the control box. The trigger events are summarized below:

- S1: sends a trigger signal for discharging the capacitor energy into the coils,
- S3: sends a trigger signal to a thyristor switch for firing the accelerator,
- C1: measures the voltage on the capacitor via a resistive divider circuit,
- C2: initiates the charge of the capacitor bank.

The trigger signals S1 and S3 were monitored on a 500 MHz Tektronix digital oscilloscope (TDS 644). Both of these signals had amplitude of 150 V and duration of 15  $\mu$ s. Prior to connecting these signals to the oscilloscope 10 dB attenuators and pulse stretchers were used. The pulse stretchers, to be discussed in more detail in the section to follow, were made since not all the trigger events could be successfully captured on the oscilloscope.

The discharge of the capacitor bank was synchronized by setting the time delay between trigger signals S1 and S3 such that the SINUS-6 fired at the peak of the magnetic field. The time delay is set by the Labview program. The initial 100 MHz digital clock of on the SINUS-6 control system allowed a maximum delay of only 6.3 ns between two trigger events. Since the modified pulsed magnetic system had a peak field occurring at 18.5 ns the 100 MHz clock was replaced with a slower clock speed of 10

MHz, which allowed a maximum delay of 63 ms to be set between trigger events; this allowed a delay of 18.5 ms to be set between S1 and S3.

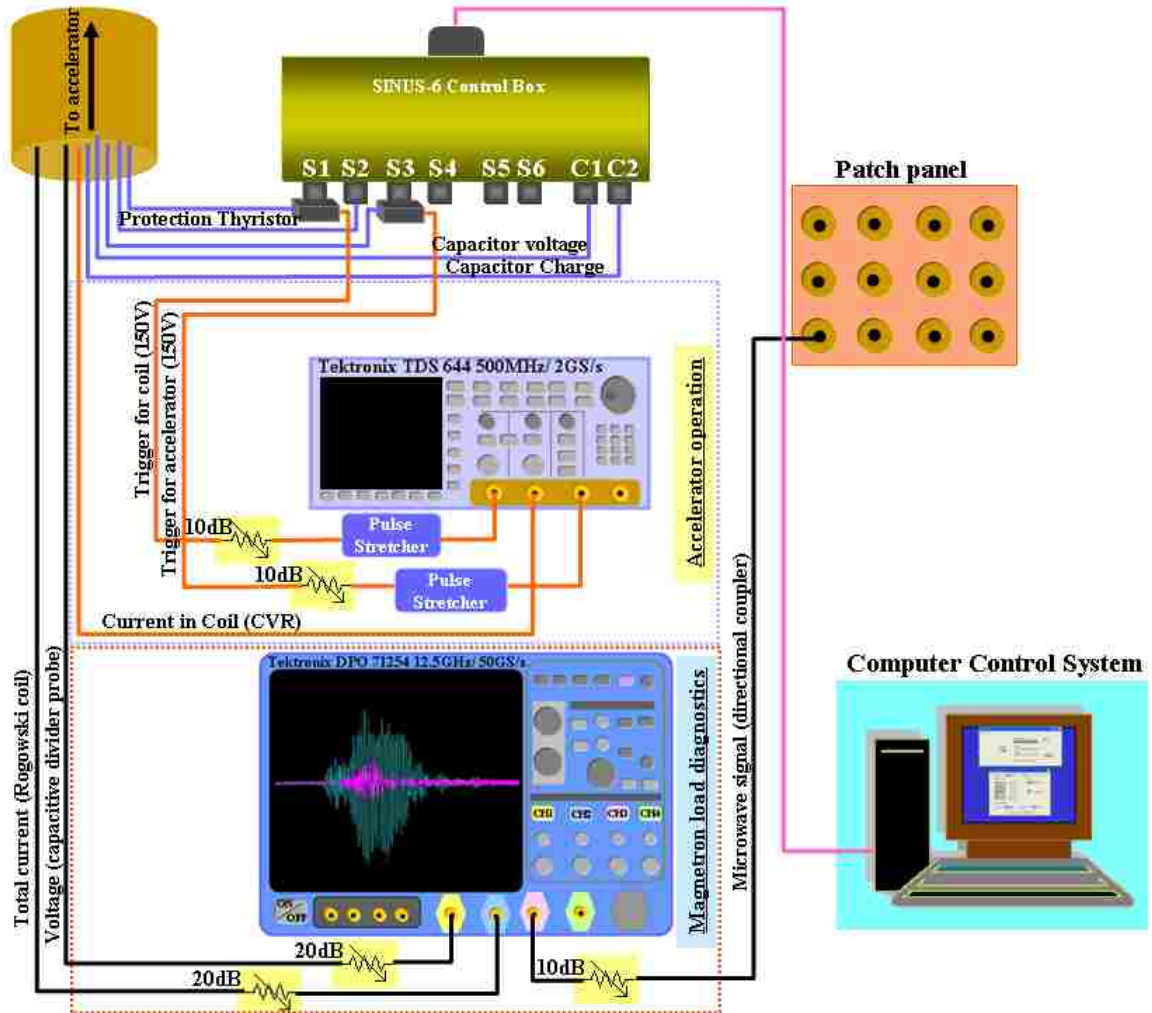


Figure 4-5 Details of the SINUS-6 control system.

#### 4.1.8 Pulse stretcher circuit

Two signals from ports S1 and S3 were sent from the control box to a Tektronix 500 MHz digital oscilloscope. These signals have amplitude of 150 V and pulse duration of 10  $\mu$ s. It was observed that for many shots the trigger events were not completely captured on the scope. This was due to aliasing, an artifact of digital oscilloscopes. Aliasing occurs when the oscilloscope does not sample the signal fast enough to construct an accurate waveform record. When this happens, the oscilloscope displays a waveform with a frequency lower than the actual input waveform or triggers and displays an unstable waveform.

For resolving these fast trigger events two identical pulse stretchers were built that produce an output pulse whose duration is greater than that of the input pulse and whose amplitude is proportional to the peak amplitude of the input pulse were built. The circuit diagram is shown in Fig. 4-6.

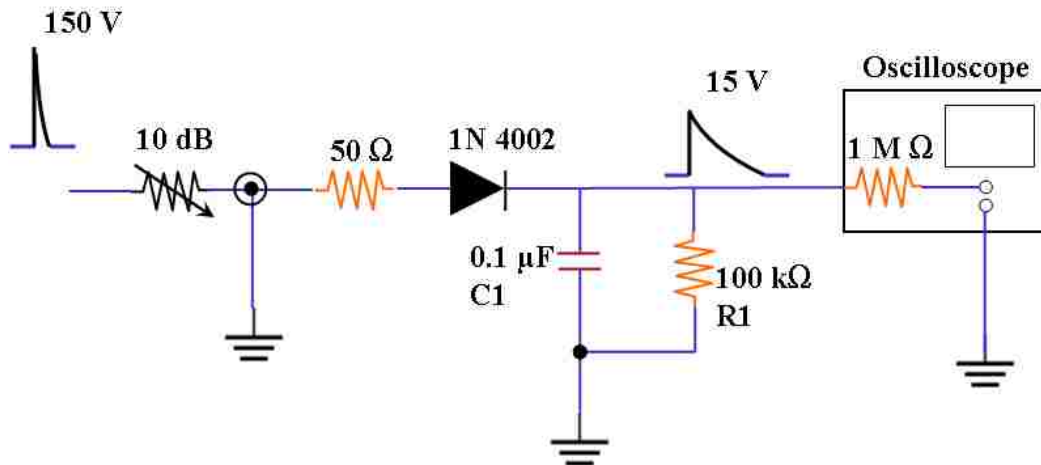


Figure 4-6 Equivalent circuit of the pulse stretcher.

A narrow positive pulse at the input causes the current to flow through the diode (1N 4002) and charges capacitor C1. This capacitor stays charged until resistor R1 slowly discharges it. The pulse width of the stretched pulse is equal to the RC time constant. The diode prevents C1 from being discharged by the input signal.



## **4.2 Pulsed Magnet**

This section discusses, in detail, the design of the magnetic coils which is a very crucial component of a crossed-field device. The vacuum chamber could only be designed after an acceptable design of the magnetic coils was reached. The coil is designed such that it can provide a maximum magnetic field of 1 T.

### **4.2.1 Requirements on the Coils**

A new magnetic field-producing system had to be designed and built since the original SINUS-6 solenoid system could not meet the magnetic field requirements of the A6 magnetron both physically and electrically.

The new coils had to meet the typical design requirement of  $\pm 2\%$  field uniformity in the interaction space [6] as well as provide radial access to the magnetron for microwave extraction. A pair of Helmholtz coils was the best option since it satisfied the above mentioned conditions.

### **4.2.2 Helmholtz Coils**

The new magnetic system features a capacitive discharge into an inductive, resistive pair of Helmholtz coils. A Helmholtz coil is a parallel pair of identical coils separated one radius apart and wound in series so that the current flows through both coils in the same direction. Consequently, the magnetic field produced by current flowing in one coil aids the field in the other coil. The basic premise of a Helmholtz coil is that it produces a homogeneous magnetic field in its center and allows radial access to the device.

The principle advantage of pulse systems lies in their ability to store energy over a long period of time and then rapidly discharge the energy through a coil, relying on thermal inertia to prevent overheating thereby removing the need for an additional cooling system.

### **4.2.3 Basic Parameter Selection**

The selection of the basic parameters is the first step in the design of the coils. The design of the coil commenced with a pair of single-turn loops in an arbitrary Helmholtz configuration and arbitrary current passing through each turn. These two parameters were tweaked until the desired field uniformity and magnetic field amplitude were reached. A 2-dimensional magnetostatic code, FEMM (Finite Element Magnetic Moments) was used for the initial coil design process. The axis symmetric model was used since the coil is uniform in the azimuthal direction.

Simulations showed that loop radius and separation of 13.2 cm would provide magnetic field uniformity of 99.6% over the length of the magnetron, i.e. 7.2 cm. Furthermore, a total amp-turn of 103.5 kA in this configuration would produce 0.68 T which is the maximum required b-field for magnetron experiments at an applied voltage of 350 kV. Once these parameters were confirmed, the total amp-turn was distributed over a cross-sectional area. The dimensions of the coils were restricted in the horizontal and vertical directions. The gap between the two coils had to accommodate the waveguide section for microwave extraction, thereby limiting its axial dimension. In the vertical direction the dimension of the coil was limited by the diameter of the flange of the vacuum chamber since the coil had to be able to slide over the vacuum chamber.

Taking into account the requirements of field uniformity and limitations on the physical dimensions the coil dimensions were finalized. Figure 4-7 shows the optimized coil configuration. A plot of the magnetic field uniformity in the interaction volume is shown in Fig. 4-8. Figure 4-8 shows that the variation in the magnetic field was less than 1% axially and radially in the interaction space, which is better than the initial design requirement.

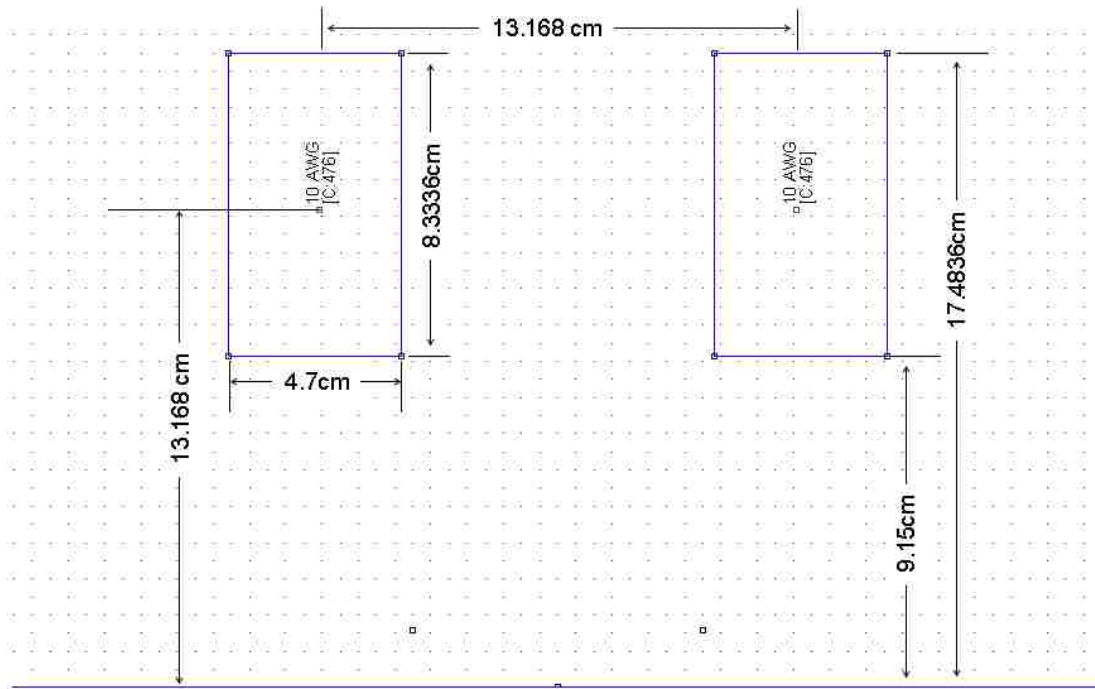


Figure 4-7 The physical dimensions of the optimized coil design.

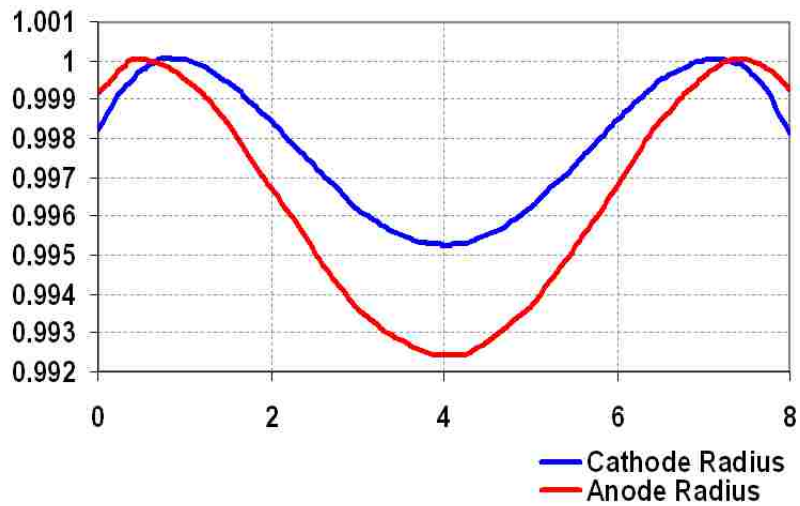


Figure 4-8 Magnetic field uniformity along the length of the magnetron, and between the A-K gap.

#### **4.2.4 Coil Fabrication Procedure**

The windings on the coils are made of AWG-10 wire which provides a maximum allowable DC current of up to 20 A and has high thermal resistant enamel insulation. A pair of identical coils were wound on non-magnetic, non-metallic phenolic framework. Each coil had 24 layers and each layer had 20 turns. The maximum applied voltage on each coil would be 1.5 kV since the maximum available energy is 3 kV, implying that the inter-layer voltage drop is ~60 V. In a multi-layer coil the forces between the layers is such that it causes a slipping motion. To increase the lifetime of the coil and avoid breakdown between the layers if the coil were to be operated at higher voltage, as an additional safety measure fiberglass tape was wound around each consecutive layer. Both coils were then potted in heat cured-epoxy. Figure 4-7 shows the physical dimensions of the coils. The gap between the Helmholtz pair and currents running in the same direction would cause a strong attractive force between them. It was necessary to calculate this force in order to estimate the required amount of support between the coils to prevent them from collapsing into each other. Details can be found in Appendix 1.

The temperature rise in the coil was also estimated to prevent damage to the coil from heating since the coils are uncooled during the pulse. The equations are presented in Appendix 2.

Figure 4-9 is a photograph of the fabricated coils. The axial magnetic field of the manufactured coil was measured using a digital Gauss meter (455 DSP) mounted on the magnetron drift tube in the anode center plane. The experimental measurement confirms the magnetic field uniformity predicted by the simulations. The coil was suspended using stainless steel rods. Once the coils were set to the Helmholtz configuration they were secured with stainless steel bolts in order to prevent being pulled towards each other, since the current through the coils would generate very strong attractive forces. Coaxial rings were made to align the axis of the magnetron section with the axis of the coils. This coaxial alignment ensures that the radial uniformity is maintained.

The coil electrical parameters estimated from the simulations and measured with an LCR (Inductance Capacitance Resistance) meter are tabulated in Table 4.1. The numbers compare very well.



Figure 4-9 Photograph of the manufactured Helmholtz Coils.

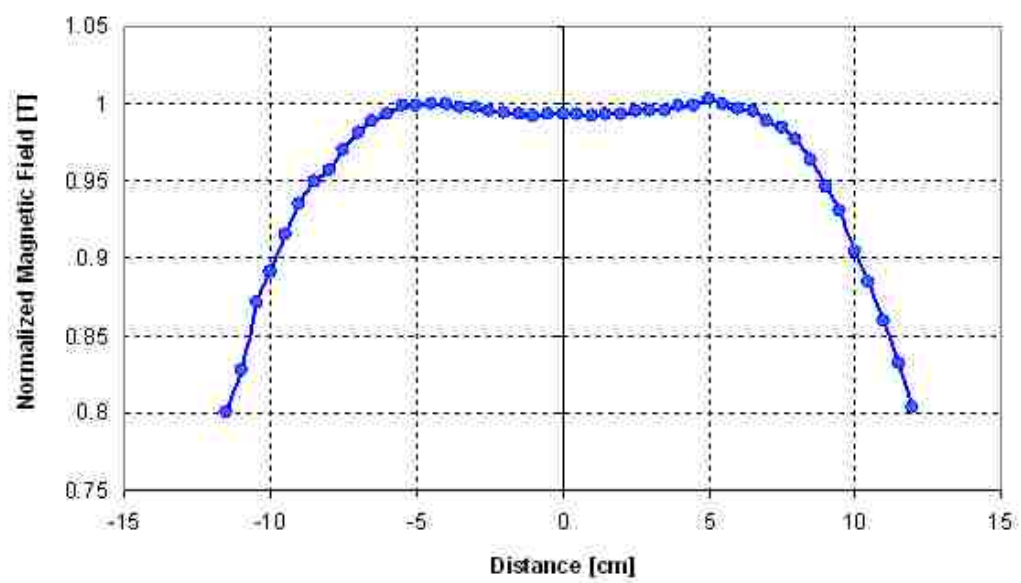


Figure 4-10 Magnetic field distribution of the manufactured Helmholtz coils.

**Table 4.1 Comparison of the calculated and measured electrical parameters of the coil**

<b>Quantity</b>	<b>Calculated Value</b>	<b>Measured Value</b>
Self Inductance	62.986 mH	63 mH
Internal Resistance	1.3042 $\Omega$	1.3 $\Omega$
Total Inductance	152.593 mH	153 mH
Total Resistance	2.60885 $\Omega$	2.6 $\Omega$

The coil configuration is not the only factor that affects magnetic field uniformity in pulsed magnetic systems. Metallic objects within the cylindrical volume of the coil tend to distort the magnetic field lines. This is a phenomenon that persists when the L/R time of the metallic objects enclosed within the magnetic volume is greater than the time scale of the applied time varying magnetic field. The L/R time is the characteristic time during which the eddy currents decay in conductors that are exposed to the time varying magnetic field. These eddy currents generate magnetic fields that oppose the change of the original magnetic field and prevent the magnetic field from penetrating. Therefore, to achieve a good degree of field uniformity the electrical properties of the pulse magnetic circuit must be such that the time for the first quarter cycle of the current rise must be greater than the L/R times of metallic objects that are enclosed by the coils.

The “Universal BField Toolkit” composed by Field Precision, capable of solving time-varying magnetic fields and eddy current effects, was used to cross-check FEMM calculations. These simulations confirmed that the magnetic fields generated by the manufactured coils reached the desired field uniformity around 19 ms. This time scale of 19 ms may be a slight over-estimation since the Universal BField Toolkit is a two-dimensional code and therefore could not take the three-dimensional property on the magnetron anode block into account. The cavities of the magnetron anode block would ease the magnetic field penetration process.

#### 4.2.5 Pulsed Magnet Circuit

The coils were energized with a 4.5 kJ capacitor bank which consists of a pair of 500  $\mu\text{F}$  capacitors with voltage rating of 10 kV. Three SCR switches connected in series are used to discharge the capacitors into the coils. The voltage rating of the SCRs limits the maximum allowable charge voltage to 3 kV. By varying the magnet capacitor bank charge voltage, the magnetic field in the interaction space was variable from 0 ~ 0.68 T. Because the time scale for the magnetic field pulse was in the order of  $\sim 10^5$  greater than the pulse duration of the diode voltage, the magnetic field was essentially DC during the time period of interest.

The pulsed magnetic circuit is a simple series RLC circuit. With all the circuit parameters known a P-SPICE simulation was carried out to determine the maximum current that can be driven by the coils. Figure 4-11 shows the circuit diagram.

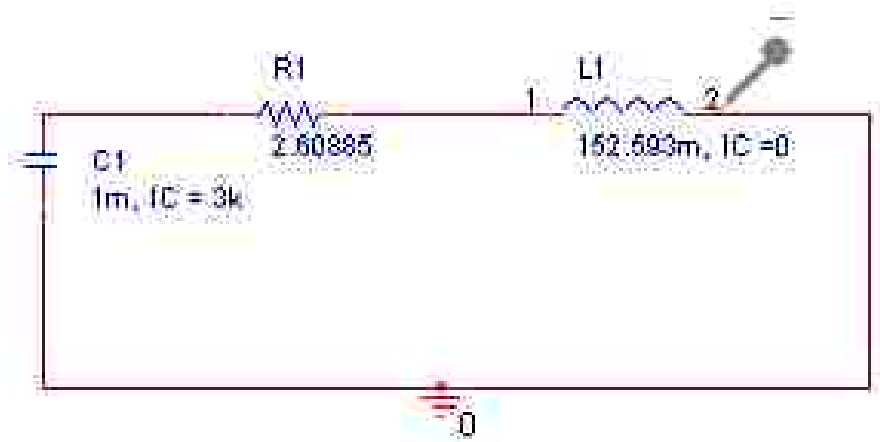


Figure 4-11 The RLC circuit diagram for the pulsed magnets.

The P-SPICE simulation showed that a maximum discharge current of 207 A could be acquired with a charging voltage of 3 kV, as shown in Figs. 4-12 and 4-13. With this current amplitude a maximum magnetic field of 0.68 T can be obtained. The coil and circuit parameters are summarized in Table 4.2. The time of the first quarter cycle is 18.5 ms.

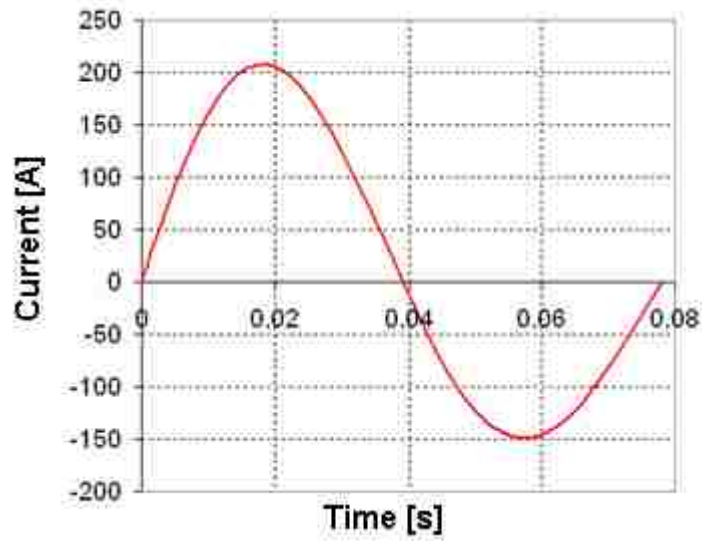


Figure 4-12 Current waveform when the capacitor is discharged into the coils.

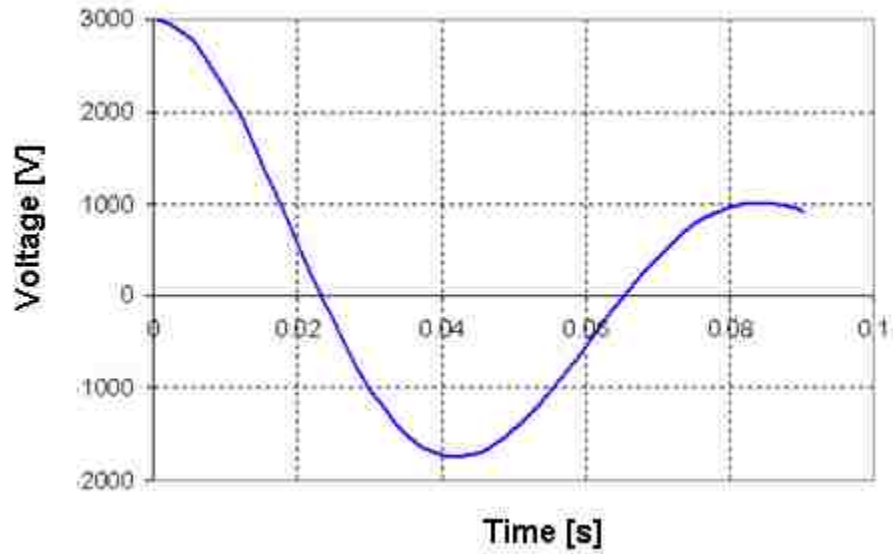


Figure 4-13 Discharge voltage of the capacitor.



**Table 4.2 Summary of the LCR circuit parameters.**

Maximum available energy	3 kV
Damping constant	0.029
Time for half cycle	42 [ms]
L/R time of coil	38.6 [ms]
Maximum current in circuit	207[A]
Magnetic field @ 207A	0.62 [T]
Temperature rise in coil @ 180A	0.7 [°C/shot ]
Force between coils @ 180A	5000 [N] 510 [kg] 1 122 [lbs]

### **4.3.1 Vacuum Chamber and the Oil-Vacuum Interface**

In order to perform magnetron experiments at UNM a new vacuum chamber including a new oil-vacuum interface was designed and manufactured. The new vacuum chamber was built in a way that it could be used on both the SINUS-6 and the Pulserad 110a accelerators. One of the distinctive features of the modified Pulserad 110a is that it could implement a fast oil-breakdown switch that will permit a voltage rise-time of 4 ns on to a matched load of 20  $\Omega$ . (The importance of voltage rise-time on magnetron operation has been explained in Chapter 3). Thus, to maintain the fast voltage rise-time inductance losses in the section had to be minimized.

The design of a low inductance 45° radial oil-vacuum interface, followed by a discussion of the design constraints of the vacuum chamber and finally an estimate of the increase of the voltage rise-time that incurred in the design process will be presented.

### **4.3.2 The Breakdown Process of an Insulator**

The initiation of a surface flashover usually begins with the emission of electrons generally by field emission from a triple point. Sometimes the initial emission can be caused by a group of electrons or ions (produced somewhere away from the insulator) striking the surface of the insulator.

While there is general agreement on the initiating mechanism of surface flashover, there is considerable disagreement concerning the mechanism and details of the intermediate or development stage of the discharge. The paths of electrons traveling along the surface of the insulator according to three different theories in the intermediate stage are summarized in [45, 46].

The most generally accepted mechanism is that electrons cascade along the surface of the insulator, or a secondary electron emission avalanche occurs [47]. Some of the electrons field-emitted from a triple point impact upon the surface of the insulator producing additional electrons by secondary emission. Some of these secondary electrons will again strike the insulator producing additional electrons by tertiary electrons. Continuation of this process results in a cascade along the surface of the insulator that

develops into secondary electron emission avalanche (SEEA). This SEEA, in turn, can lead to a complete breakdown.

Most work concerning surface flashover in vacuum has considered the cathode initiated flashover. However, under appropriate conditions a surface flashover may be initiated at the anode and will develop differently than a cathode initiated flashover. For further details see references [45-56].

Once a surface flashover has begun, its development times are generally fairly short, with complete collapse of the voltage along insulator occurring in times of the order of several ns. A surface flashover can damage the surface of an insulator. This damage can be severe enough to lower subsequent flashover voltages significantly. In some cases, the damage is sufficient to render the insulator useless. In applications where surface flashovers may occur during operation an insulator material strongly resistant to damage may be preferred to one with a higher surface flashover voltage.

### **4.3.3 The 45° Insulator**

One way to prevent the electrons from reaching the insulator surface, and therefore from multiplying, is to have some angle  $\theta$  between the insulator surface and the applied electric field. Figure 4-14 shows the flashover strength versus angle of insulator for Lucite between parallel plate electrodes. The angle is measured between the normal electric field line and the insulator surface. Investigations show that other insulators have similar dependence on the angle to that shown in Fig. 4-14. Surface flashover voltage of various dielectric materials has been determined by O. Milton [44].

From Fig. 4-14 it is apparent that the optimal insulator angle is 45°. The 45° insulator has been explored by many researchers. A large number of accelerators operate reliably with the 45° insulator in a stacked configuration with grading rings, as shown in Fig. 4-15 [44].

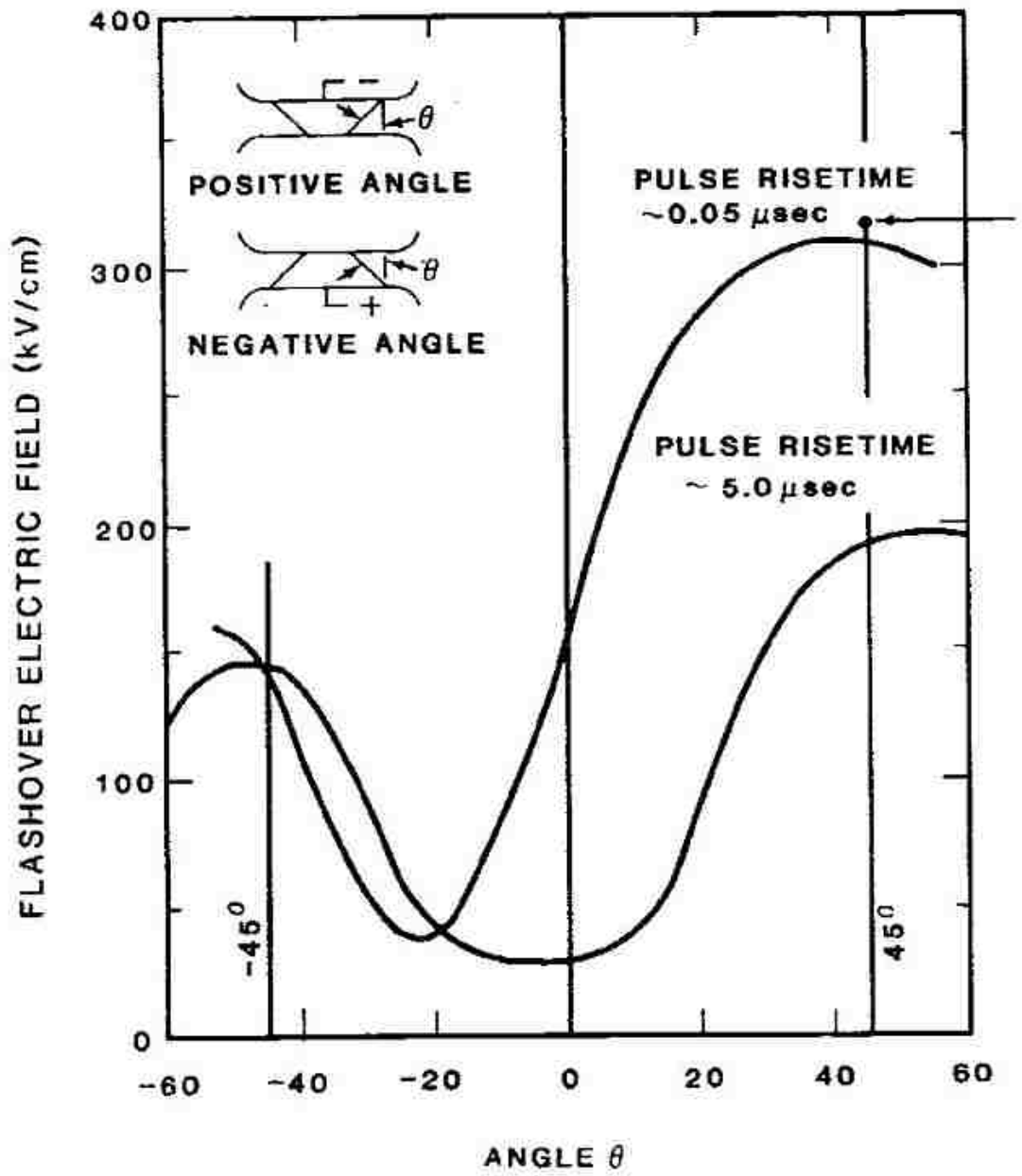


Figure 4-14 Flashover strength versus angle of insulator for Lucite between parallel plate electrodes [51].

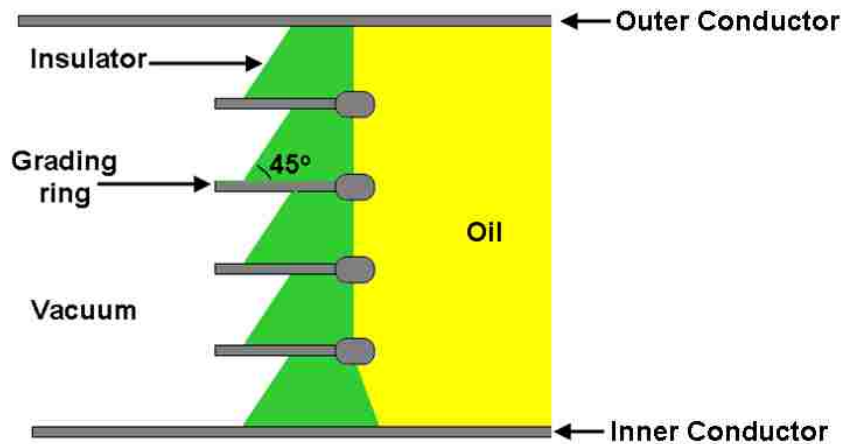


Figure 4-15 Insulator stack with parallel plate grading ring.

Equation 4-1-1 is an empirical formula deduced from these investigations to determine the breakdown strength of the insulator surface [44, 51]

$$F t_f^{1/6} A^{0.1} = 175. \quad (4-1-1)$$

Here  $F$  is the electric field in kV/cm at which the probability of flashover of the vacuum insulator is 50 %,  $t_f$ , the effective time in  $\mu s$  during which the voltage across the insulator is greater than 89 % of the peak value, and  $A$  is the area of the insulator in  $cm^2$ .

The breakdown strength varies with angle as shown in Fig. 4-13 because of the following two facts: 1) the electric field at the cathode triple point is decreased with the insulator angle due to the difference in dielectric constant of the dielectric and vacuum, 2) if electrons are emitted at this triple point, the probability that they will contact the insulator is small.

The  $45^\circ$  insulator was chosen for the new vacuum chamber. Although there is extensive data available for this design, operation of SINUS-6 with the  $45^\circ$  insulator, not in a stacked configuration, would be the first time this could be tested on a working accelerator system [51].

Figure 4-16 is taken from one of the simulations performed in the absence of an applied axial magnetic field, using the 2.5-dimensional (two spatial and three velocity components) PIC code MAGIC.

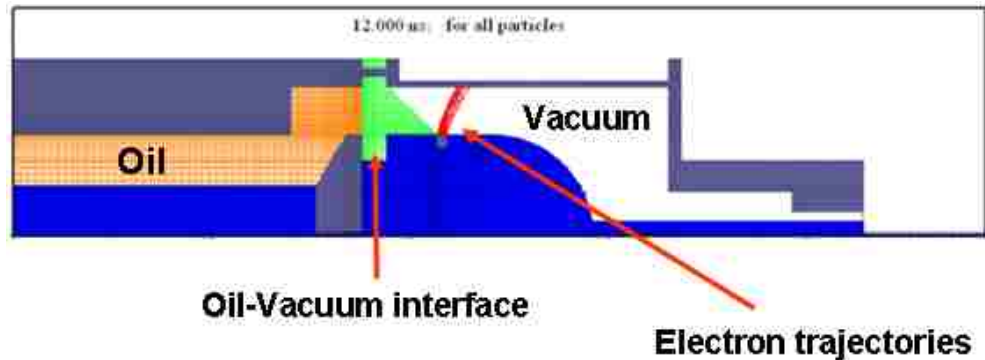


**Figure 4-16 Electron trajectories at the cathode triple point in the absence of applied axial magnetic field.**

In the simulation a very small emission region was created at the cathode triple point that was allowed to emit electron at very low electric field strength of 30 kV/cm. It is apparent from the simulation that electrons born at the cathode triple points would take paths that were unlikely to strike the insulator surface. Furthermore, the current through the inner conductor generates azimuthal magnetic field  $B_{\theta}$  around it.  $B_{\theta}$  crossed with the applied radial electric field  $E_r$  causes an axial drift, in this case, in the direction of increasing  $z$ -coordinate, thus pushing the electrons further away from the insulator. This effect is shown very clearly in Fig. 4-16.

Figure 4-17 shows the equipotential line plots. The bending of the equipotential lines as they transition from the 45° insulator onto vacuum indicates the weakening of the radial electric field at the triple point. This is caused by the difference in dielectric constant of the insulator and vacuum.

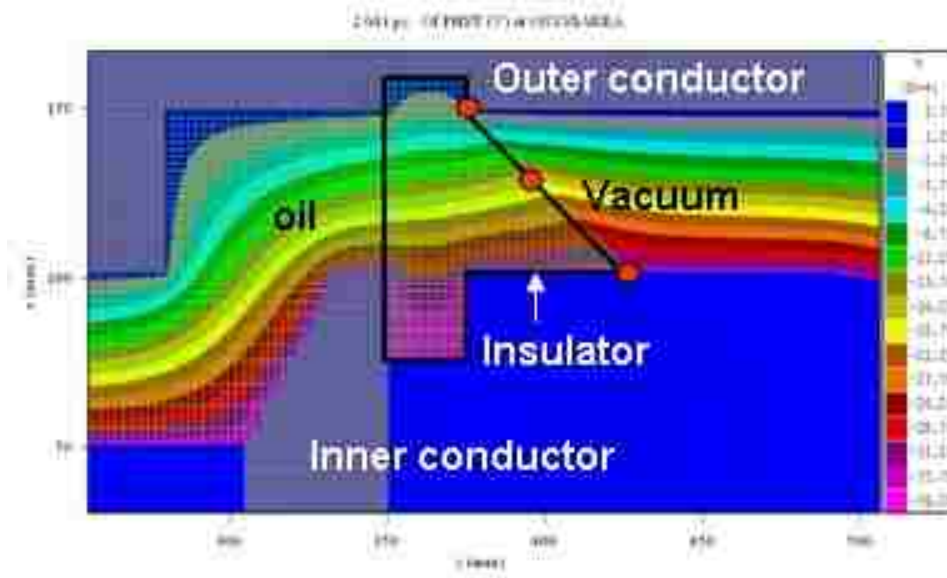


**Figure 4-17 Equipotential lines generated by MAGIC showing weakening of the radial electric field at the triple junction of the 45° insulator.**

The electric fields along the surface of the insulator with an applied voltage of rise-time 4 ns and constant voltage amplitude of 350 kV up to 30 ns, were measured at three distinct points indicated on Fig. 4-17. The values are summarized in Table 4.3.

**Table 4.3 Maximum radial electric fields along the insulator surface**

<b>Position</b>	<b>Radial Electric Field [kV/cm]</b>
Cathode triple point	45
Midway between anode and cathode	75
Anode triple point	145

The values recorded in Table 4-3 are the peak values taken during the overshoot shown in Fig. 4-18. Figure 4-18 shows the time dependence of the electric fields at the points described above. For breakdown processes the peak value would have more significance than average steady state values.

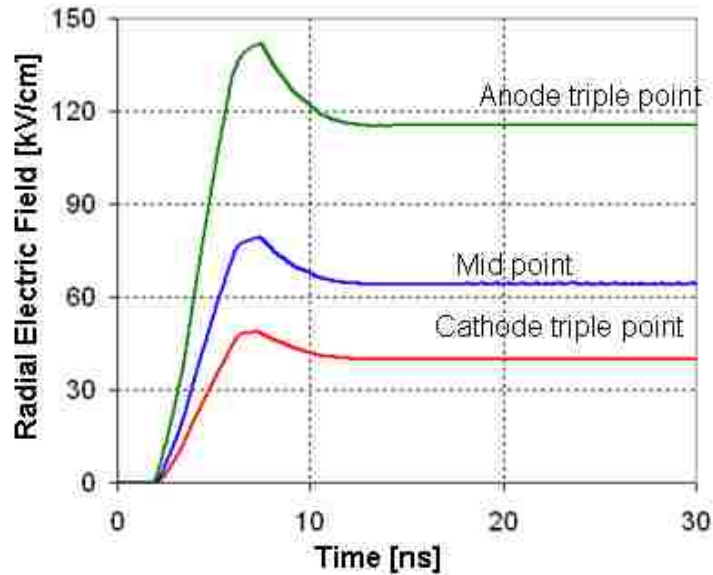


Figure 4-18 The radial electric field measured along the surface of the insulator.

The 45° angle ensures that even if the accelerator is accidentally fired without a magnetic field the electrons will have a trajectory such that the chance of insulator breakdown due to secondary electron emission is minimal.

The term  $t_f^{1/6} A^{0.1}$  in the scaling formula is equal to unity and the projected breakdown strength 175 kV/cm. Therefore, our operating field is 26% of the expected breakdown strength. This is a very large safety factor. In addition, the emission threshold level of stainless steel is expected to be greater than 150 kV/cm in the short pulse regime. In this design the maximum electric field of the inner conductor that extends after the insulator is 80 kV/cm, thereby adding to the already existing safety factor.

Generally with pulsed voltages the surface flashover voltage decreases with increasing pulse duration in the ns region. The effect of insulator angle is much greater for short voltage pulses (ns) than it is for  $\mu$ s or longer pulses.

Lexan was the material of choice for the construction of the oil-vacuum interface due to its property as a good vacuum material and ease of machining.

Most theories of surface flashover predict that the final stage of flashover involves gas desorbed from the surface of the insulator. For this reason the surface of the insulator



on the vacuum side was thoroughly cleaned with alcohol and later pumped on under high vacuum for a long period of time before applying voltage in order to improve its hold-off voltage.

#### **4.3.4 Design of Vacuum Chamber**

The section of the vacuum chamber that followed the oil-vacuum design involved some very careful engineering before a final design was reached. A small section of the transmission line that shows the vacuum chamber is shown in Fig. 4-19.

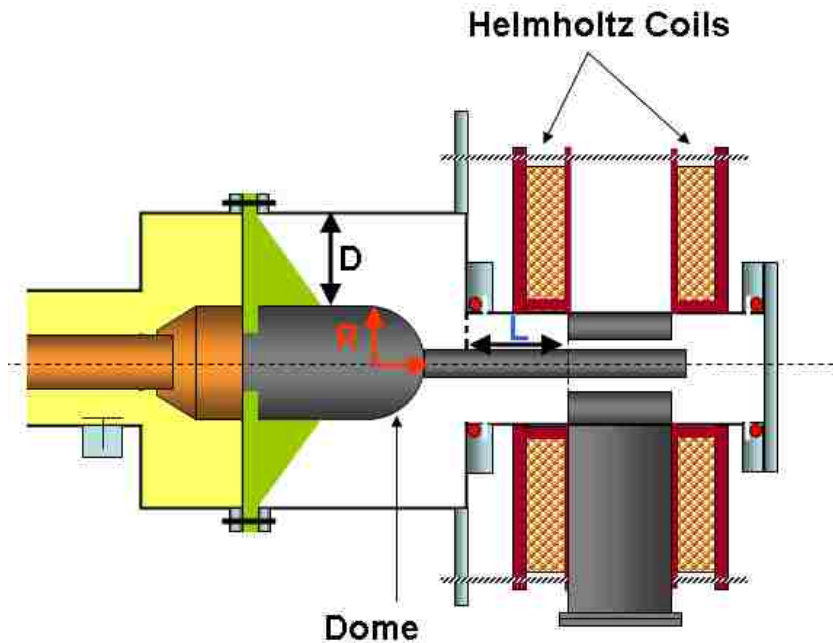


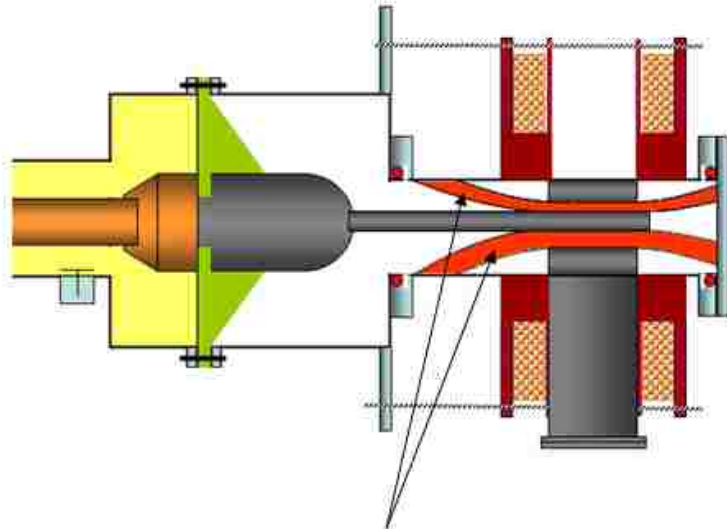
**Figure 4-19 Vacuum chamber section showing parameters D, R and L that had to be optimized.**

D is the gap between the inner and outer conductors of the section of the transmission line that follows right after the oil-vacuum interface. The impedance of this section had to be between  $20 \Omega - 30 \Omega$  and the electric field levels had to be maintained below  $100 \text{ kV/cm}$ . The final dimensions of the inner and outer conductor have been chosen such that the electric field on the surface of the inner conductor was  $80 \text{ kV/cm}$  with an applied voltage pulse of  $350 \text{ kV}$ . The vacuum chamber was constructed of

stainless steel 304 L for several reasons: 1) it has a high vacuum compatibility; 2) polishing the surface so that it has a “mirror finish” increases the emission threshold to ~ 300 kV/cm; 3) its conductivity is lower than copper allowing for faster magnetic field penetration. The radius of the dome, R was determined by the dimensions of the inner conductor, and the outer conductor, and gap D.

Due to the coaxial shape of the magnetron and its finite length, electrons leak from the magnetron interaction space in both the upstream and downstream directions along the magnetic field lines. The length L shown in Fig. 4-19 was adjusted so that the leakage electrons would be trapped by the dome and situations shown in Fig. 4-20 (top) and (bottom) could be avoided. Both of these cases lead to current loss in the system and lower the total efficiency. The leakage current in the upstream direction is usually much less than the leakage current in the downstream direction. The leakage current in the downstream direction has been a subject of much discussion and details can be found in [56, 57], but is not the main focus of this section. Even though the upstream current is of the order of ~100 A, a situation like that shown in Fig 4-20 (bottom) where electrons streaming from the interaction space are very close to the oil-vacuum interface is highly undesirable. The scenarios depicted in Figs. 4-20 could be created with a  $\pm 5$  cm change of the parameter L.

Figure 4-21 shows the optimized vacuum chamber dimensions. The distribution of the magnetic field lines that extend from the interaction space suggest that the leakage electrons in the upstream direction will be successfully trapped by the dome. Figure 4-22 shows the results from a 2-dimensional MAGIC simulation confirming the electron behavior predicted by the magnetic field lines in Fig. 4-22. The smaller spread in the electron distribution at their point of contact with the dome is attributed to the way the Helmholtz coils were modeled in MAGIC, i.e. two single-turn coils.



Electrons leaking from the magnetron interaction space via the magnetic field lines

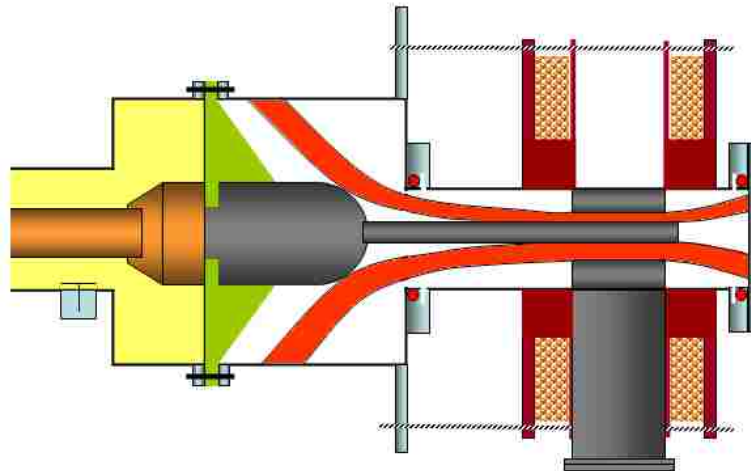
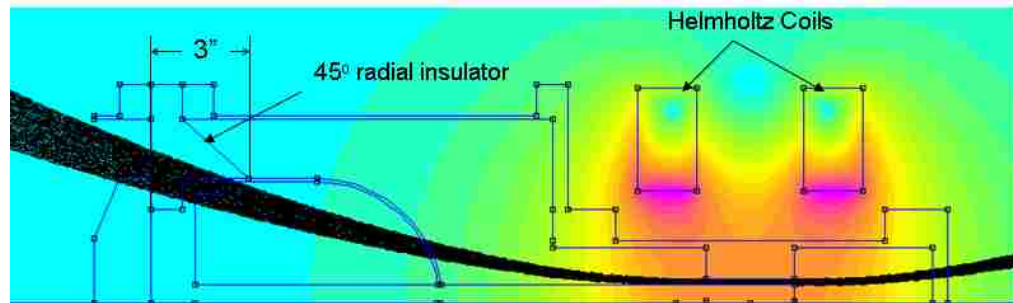
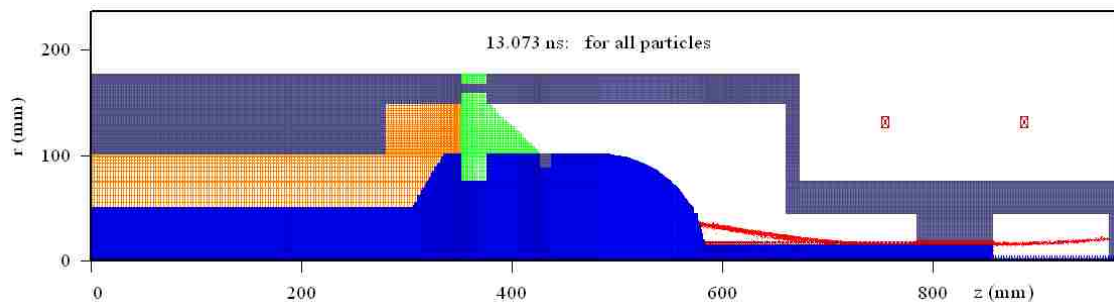


Fig. 4-20 Possible scenarios of leakage electrons in the upstream direction depending on the length  $L$ , of the section shown in Fig 4-18.



**Figure 4-21 Magnetic field lines predicting the electron trajectories defined by the coils using FEMM.**



**Figure 4-22 Particle trajectories from MAGIC simulation showing that the leakage electrons are trapped by the dome.**

To determine the final voltage at the load, the complicated transmission line geometry that delivers the voltage pulse to the load was divided into 7 sections as shown in Fig. 4-23. The characteristic impedance and electrical length of each section was estimated. The values are shown in Table 4-4. A PSPICE model of the experimental setup, shown in Fig. 4-23 was created. The circuit model of the SINUS-6 pulser used in this simulation is shown in the same diagram. The pulser model uses a voltage pulse trapezoidal in time with rise time, flat-top duration and fall times of 5 ns, 10 ns and 5 ns, respectively. The magnetron load was treated as a 25  $\Omega$  resistor. The voltage pulse at the source and the final voltage at the load are shown in Fig. 4-24. This result suggests that the final voltage pulse at the load would suffer a degradation in rise-time of approximately 1.5 ns.

**Table 4-4 Equivalent impedance and electrical lengths of the transmission line model.**

<b>Transmission Line Section</b>	<b>Electrical Length</b>	<b>Impedance</b>
<b>T2</b>	<b>13.8 ns</b>	<b>27 <math>\Omega</math></b>
<b>T3</b>	<b>0.68 ns</b>	<b>16 <math>\Omega</math></b>
<b>T4</b>	<b>0.56 ns</b>	<b>6.5 <math>\Omega</math></b>
<b>T5</b>	<b>0.25 ns</b>	<b>24 <math>\Omega</math></b>
<b>T6</b>	<b>0.42 ns</b>	<b>42 <math>\Omega</math></b>
<b>T7</b>	<b>0.25 ns</b>	<b>135 <math>\Omega</math></b>
<b>T8</b>	<b>0.42 ns</b>	<b>60 <math>\Omega</math></b>

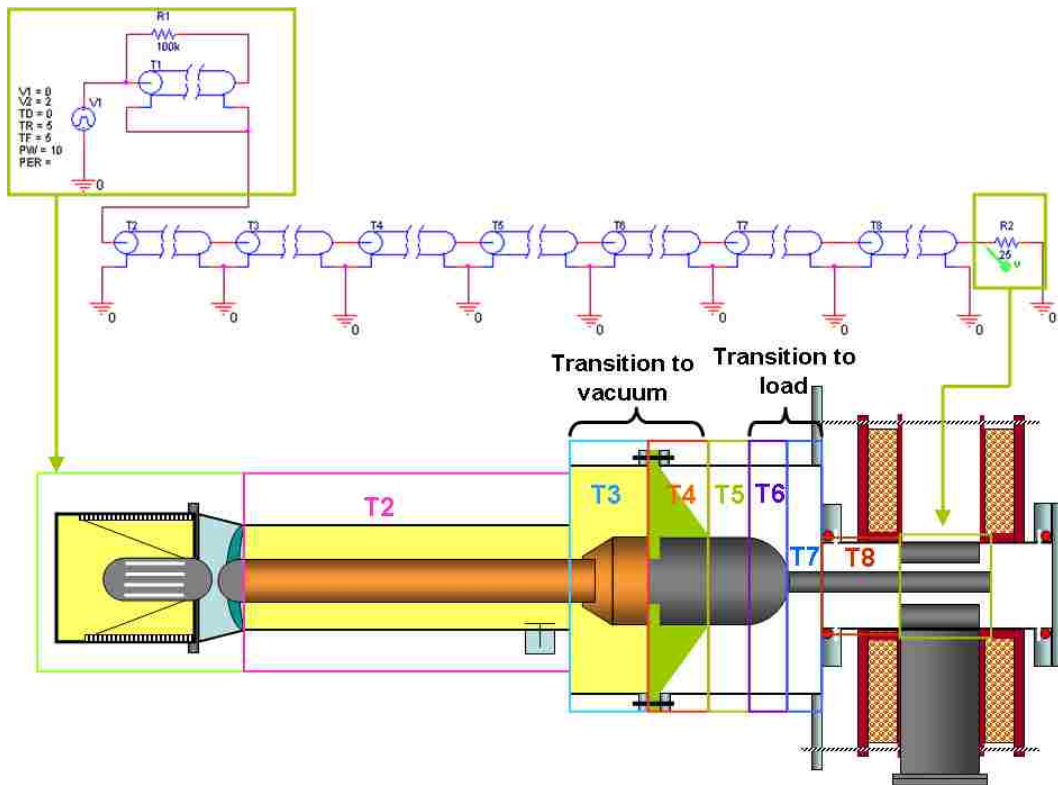


Figure 4-23 P-SPICE model of the SINUS-6 accelerator to estimate final voltage rise-time at the magnetron load.

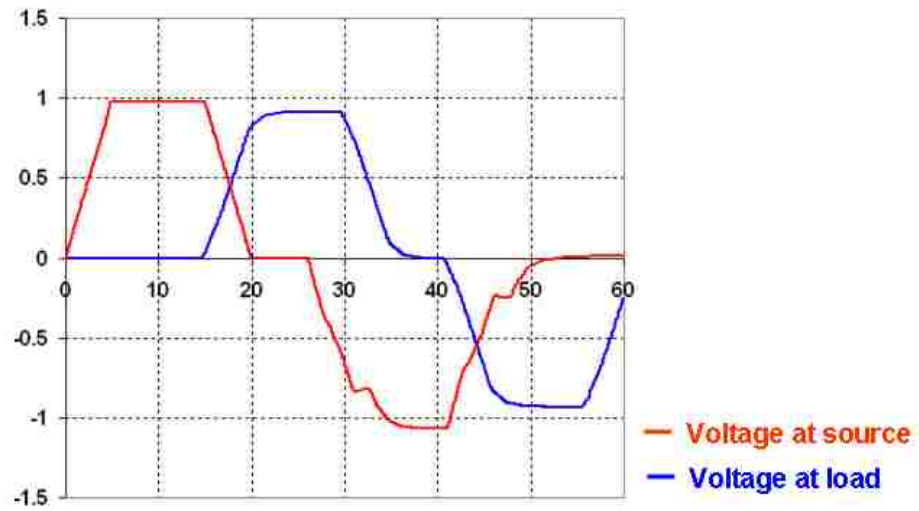


Figure 4-24 Voltage traces at the source and the load from the P-SPICE simulation.

## **4.4 Diagnostics**

This chapter will describe the diagnostics that were used to characterize the accelerator parameters and the microwave output. For measuring the applied voltage and the current at the magnetron a capacitive divider probe and Rogowski coils were used, respectively. A detailed theory and design of a capacitive divider probe is outlined in [58-66]. The theory of operation of self-integrating Rogowski coils can be found in an excellent series of papers written by Pellinen [58]. The desired magnetron output characteristics to be determined were microwave power and frequency. An E-band loop-type directional coupler was used to measure the microwave power. More information on the loop coupler can be found in [67-70]. The microwave frequency was determined by taking the fast Fourier transform (FFT) of the RF signal that was captured directly on a fast 12 GHz Tektronix oscilloscope. The operation mechanism, design and calibration of each diagnostic device will be discussed in detail in the following sections.

### **4.4.1 Voltage Diagnostic: Capacitive Divider Probe Concept of Operation**

High voltage dividers with predominantly capacitive coupling to the high-voltage electrode are frequently employed in liquid dielectric transmission lines. Figure 4-25 shows the circuit of the capacitive voltage divider connected to an oscilloscope through a coaxial cable. Capacitor C1 and C2 represent high voltage and low voltage arms. C1 is usually much less than C2 and normally is on the order of a few pF. Such a small capacitance draws very little current from the main circuit and the voltage measured by the probe  $V_s$  can be expressed as

$$V_s = \frac{V_1 C_1}{2(C_1 + C_2)} \quad (4-4-1)$$

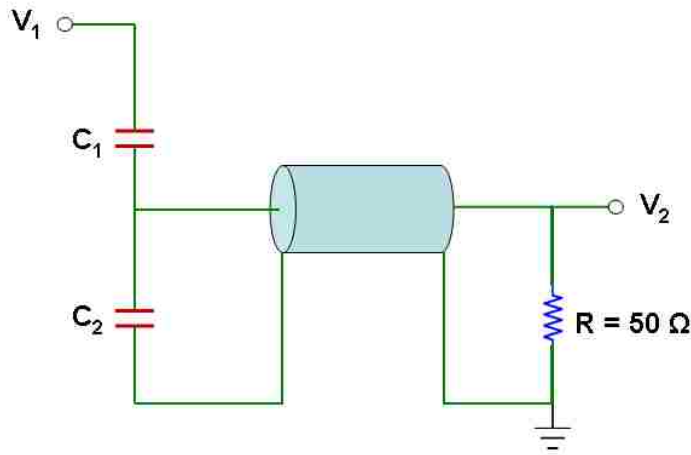


**Figure 4-25 Equivalent circuit of the capacitive divider probe on SINUS-6.**

The capacitive divider probe for voltage measurements on SINUS-6 is located towards the end of the transmission line in oil right before transition to vacuum. The initial calibration constant of the probe could not be used since the inner conductor of the transmission line was changed. The calibration procedure and the new calibration constant are described next.

#### **4.4.2 Calibration Procedure**

The transmission line was first charged via a 50 MΩ charging resistor and a high voltage DC power supply (maximum output voltage of 10 kV), powered by a 110 V AC variac. It was then discharged through a spark gap switch to a matched load which in this case is a 30 Ω carbon resistor. The charge voltage on the line was measured using a x1000 high voltage probe and a digital voltmeter, as depicted in Fig. 4-26. Figure 4-27 shows the equivalent circuit of the calibration setup. The response of the capacitive divider probe was recorded on a 500 mHz Tektronix digital oscilloscope. A typical probe response is shown in Fig. 4-28. The calibration constant was calculated by taking the ratio of the charging voltage and the voltage on the oscilloscope. This experiment was repeated for several different charging voltages in order to confirm the consistency of the calibration procedure. The calibration constant was measured to be  $726.5 \pm 2$ .



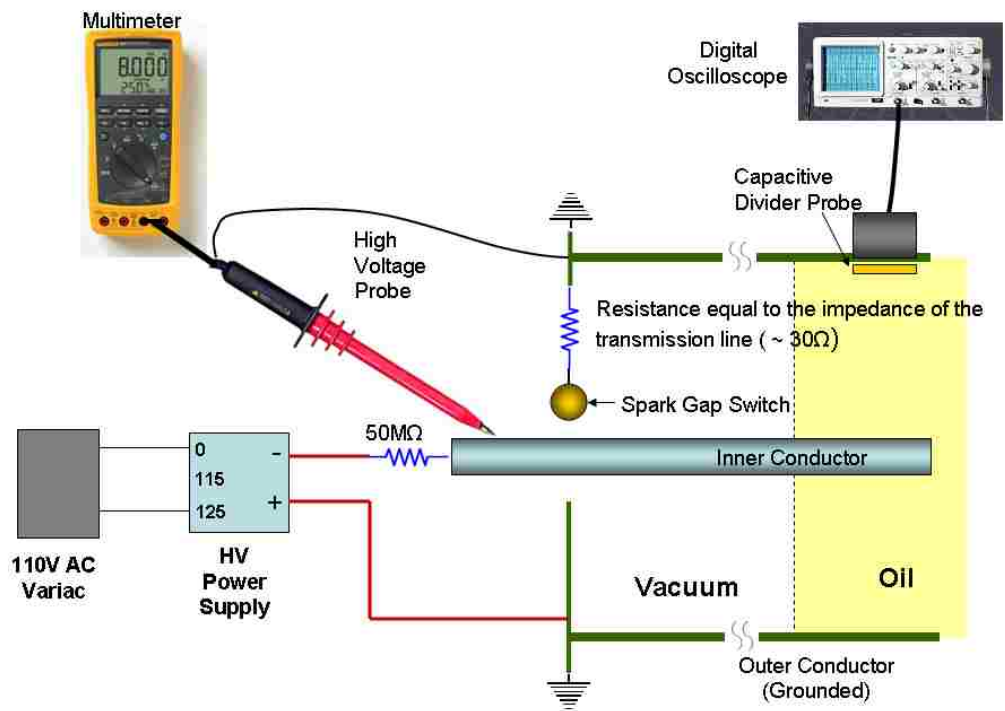


Figure 4-26 Calibration setup for the capacitive divider probe.

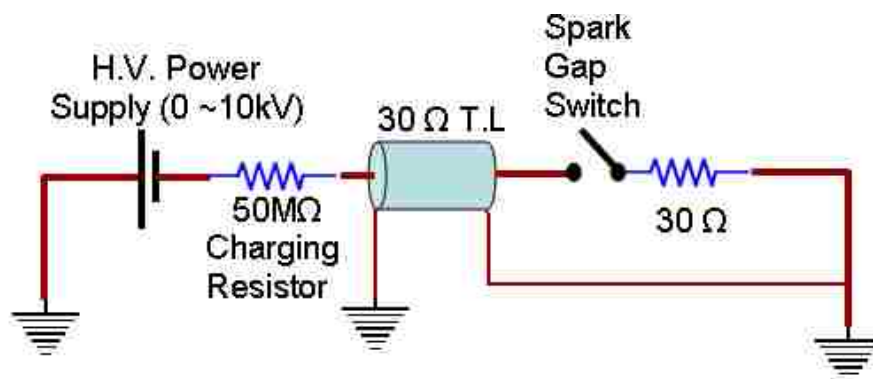


Figure 4-27 Equivalent circuit of the calibration setup.

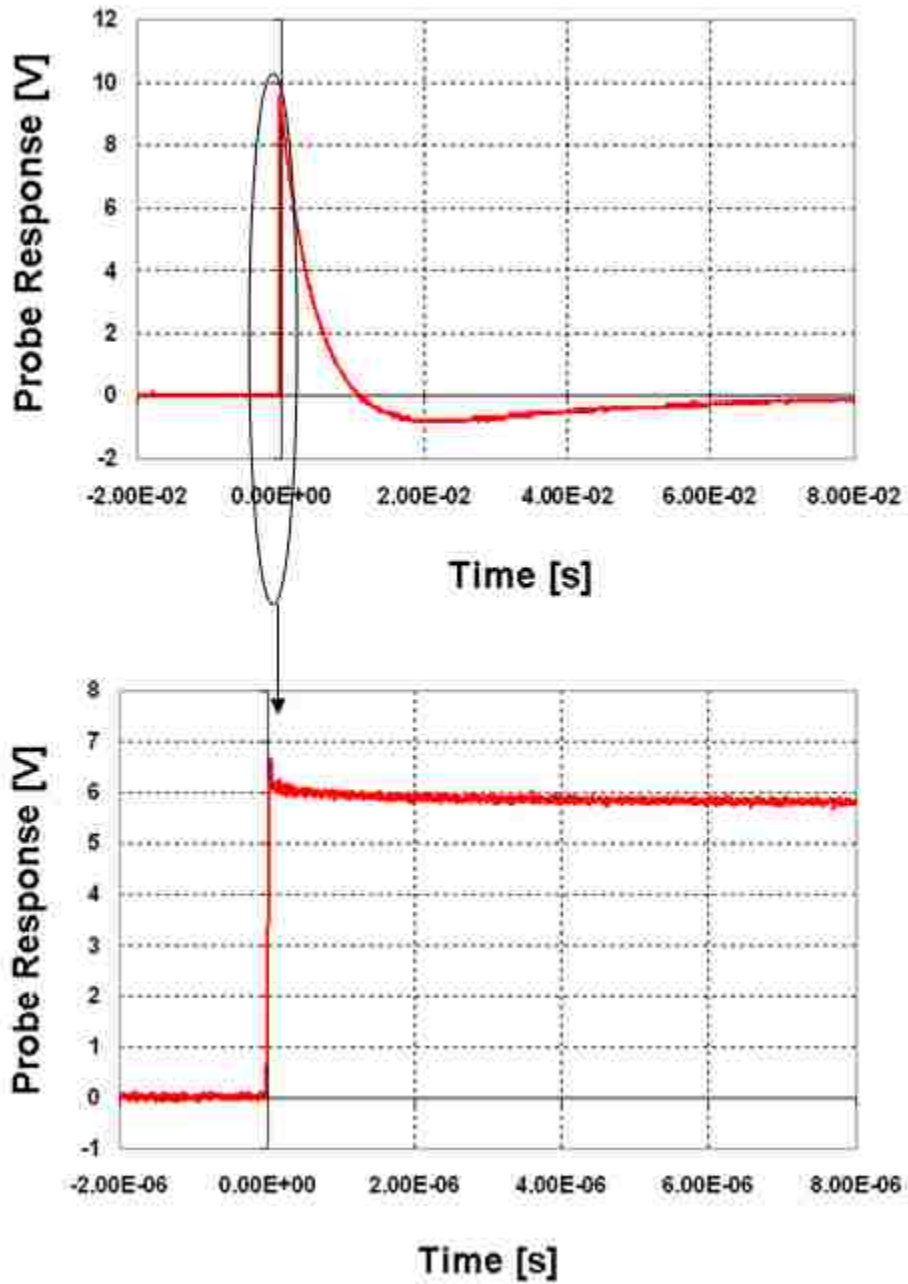


Figure 4-28 (top) Full trace of the capacitive divider probe response (bottom) zoom-in on the full trace to determine voltage response more accurately.

### 4.4.3 Current Diagnostic: Rogowski Coil

The Rogowski coil is a major tool for measuring currents of high-current, pulsed electron beam accelerators. It consists of a toroidally wound coil through which the main current (current to be measured) is threaded, as shown in Fig. 4-29. The advantages of this coil are: (1) reliability, (2) ease of installation, and (3) linearity, unlike current transformers and other ferromagnetic-cored devices. A well designed Rogowski is capable of measuring currents of the order of several hundred kA, a few ns risetime, and microsecond decay times.

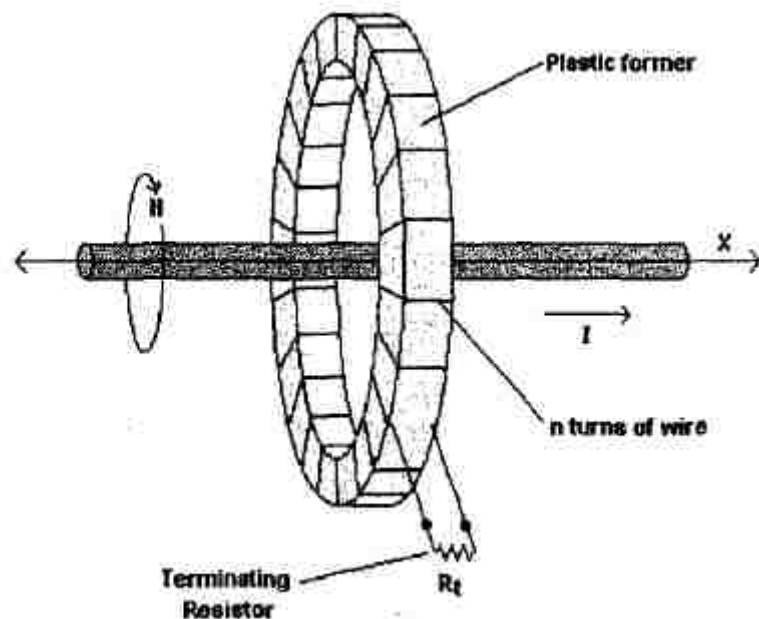


Figure 4-29 Basic structure of a Rogowski coil [64].

### 4.4.4 Concept of Operation

Figure 4-29 shows the basic structure of a Rogowski coil. It consists of  $N$  small loops with each loop forming a helix. The primary current to be determined is completely encircled by the secondary coil. Depending on the design and applications, the Rogowski coil can be used to measure the magnitude of the pulse or the rate of change of the

primary signal. The former can be measured with an external integrator or with a self-integrating Rogowski coil. The two Rogowski coils used in the magnetron experiments were self-integrating. Figure 4-30 is the equivalent circuit of a self-integrating Rogowski coil.

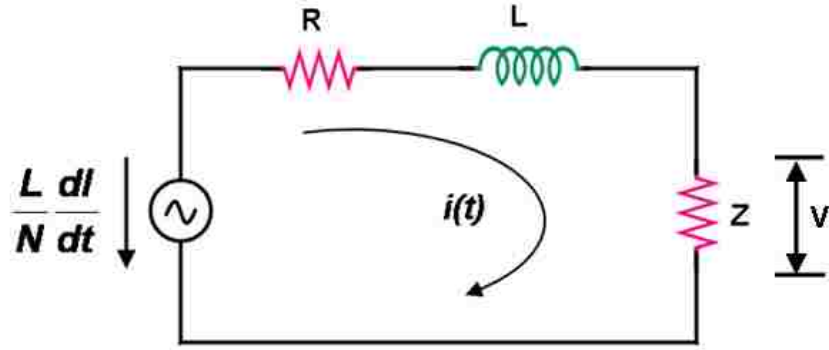


Figure 4-30 Equivalent circuit of an integrating Rogowski coil [44].

$\frac{L}{N} \frac{dI}{dt}$  is the induced EMF in the secondary coil;  $R$  is the resistance of coil;  $i(t)$  is the current secondary coil;  $Z$  is the shunt resistance;  $V$  is the voltage drop across the shunt.

The “self-integrating” Rogowski coil is not, as its name suggests, capable of self integration. It is however possible to design a Rogowski coil such that its output will (under certain conditions) be proportional to the observed current, and will as such contain no differential component. This may be accomplished by designing the coil such that the time constant  $T$  of the coil is significantly longer than the current pulse to be measured  $T = L / (R + z)$ .

The governing equation for the voltage drops along the circuit is:

$$\frac{L}{N} \frac{dI}{dt} - L \frac{di}{dt} - (R + Z)i = 0 \quad (4-4-2)$$

where  $I$  and  $i$  are the primary and secondary currents, respectively and  $L$ ,  $N$ ,  $R$  are inductance, number of turns and resistance of the Rogowski coil, respectively, and  $Z$  is the cable impedance. If the characteristics time  $t_c$  of the primary current is such that

$$t_c \ll \frac{L}{R+Z} \quad (4-4-3)$$

Then the third term in equation 3.1 can be neglected, yielding

Therefore, by measuring the voltage  $V$  across the resistance  $Z$ , one can determine  $I$ .

$$V = iZ = \frac{I}{N} Z \quad (4-4-4)$$

#### **4.4.5 Construction**

A Rogowski coil briefly comprises a wire of length  $l_w$  cross-sectional area  $A$ , and finite conductivity  $\sigma$ , wound onto a non-conducting, non-metallic, non-magnetic toroidal form of mean radius  $r$  and cross sectional area  $S$ .

Under pulsed conditions high  $dV/dt$  can produce capacitively coupled common mode currents which can significantly disturb the measurement process. To prevent this capacitive pick-up the coil is encased in a massive non-magnetic, conductive housing. This electrostatic shield must allow magnetic flux to enter the system so that either it should not completely enclose the toroidal coil; it should either be split in the median plane or its thickness should be less than the skin depth for the required frequency.

A # 31 wire was used to make the Rogowski coils. It was wound around a 1/8" flexible Teflon rod. A lot of care and attention was given during the winding process in order to avoid kinks in the wires which could create a short in the coil and thereby distort the response of the coil.

The coil wound around the Teflon rod was set in this groove giving it a toroidal shape. One end of the coil was soldered to the inner conductor of a TNC connector and the other end was connected to the housing which is grounded. A TNC connector was chosen because its threaded feature allows it to make a better electrical connection than a BNC –type connector.

Two identical coils were fabricated. Figure 4-31 is a photograph of the one of the fabricated coils. The first coil was located upstream of the magnetron to measure the total

current and the second coil was located downstream to measure the leakage current as indicated. The anode current was taken as the difference of the two measurements. Each coil had approximately 800 turns. Such a large number of turns were wound in order to satisfy the condition of a self-integrating Rogowski coil, as discussed in the preceding section. A coil designed in this manner is particularly useful since the output of the coil will be proportional to the measured current, alleviating any necessity for complex mathematical processing subsequent to or during the measurement process. Another advantage of such a design is that the signal strength is large enough that signal picked up from ground loops can be neglected. A coaxial cable carries the signal from the Rogowski coil to a digital oscilloscope which has to be internally terminated at 50  $\Omega$ . The physical and electrical properties of the Rogowski coil are summarized in Table 4.5.

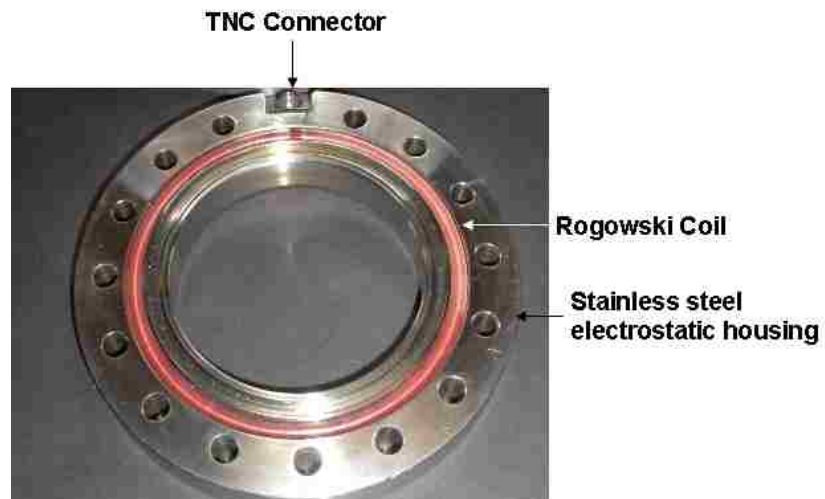


**Figure 4-31 Photograph of the fabricated Rogowski coil.**

**Table 4.5 Rogowski coil's physical parameters**

<b>Quantity</b>	<b>Description</b>	<b>Value</b>
Calibration factor		26.5 A/V
r	Major mean radius of coil	5.16cm
d	Wire diameter	0.8mm
L	Total inductance of coil	L = 98.5μH
R <sub>coil</sub>	Resistance of coil	R = 8.55Ω
N	Total number of turns on coil	800 turns
R <sub>total</sub>	Total resistance R <sub>total</sub> = R <sub>coil</sub> + 50Ω	~ 58 Ω
τ	Decay time of coil $\tau = \frac{L}{R_{total}}$	~ 1.7 μS

#### 4.4.6 Calibration

A calibration setup and procedure similar to that described in [58] was used. A high voltage, 40 ns pulser was refrabricated to calibrate the rogowski coils. A 50  $\Omega$  RG213 low loss coaxial cable was used as the charge line. A Tektronix current transformer was used to directly measure the current threading the rogowski coil. The current into a 50  $\Omega$  load is  $V_{load} / (2 \times 50)$ , and the current into a short is  $V/50 \Omega$ . A schematic of the calibration setup is shown in Fig. 4-32.

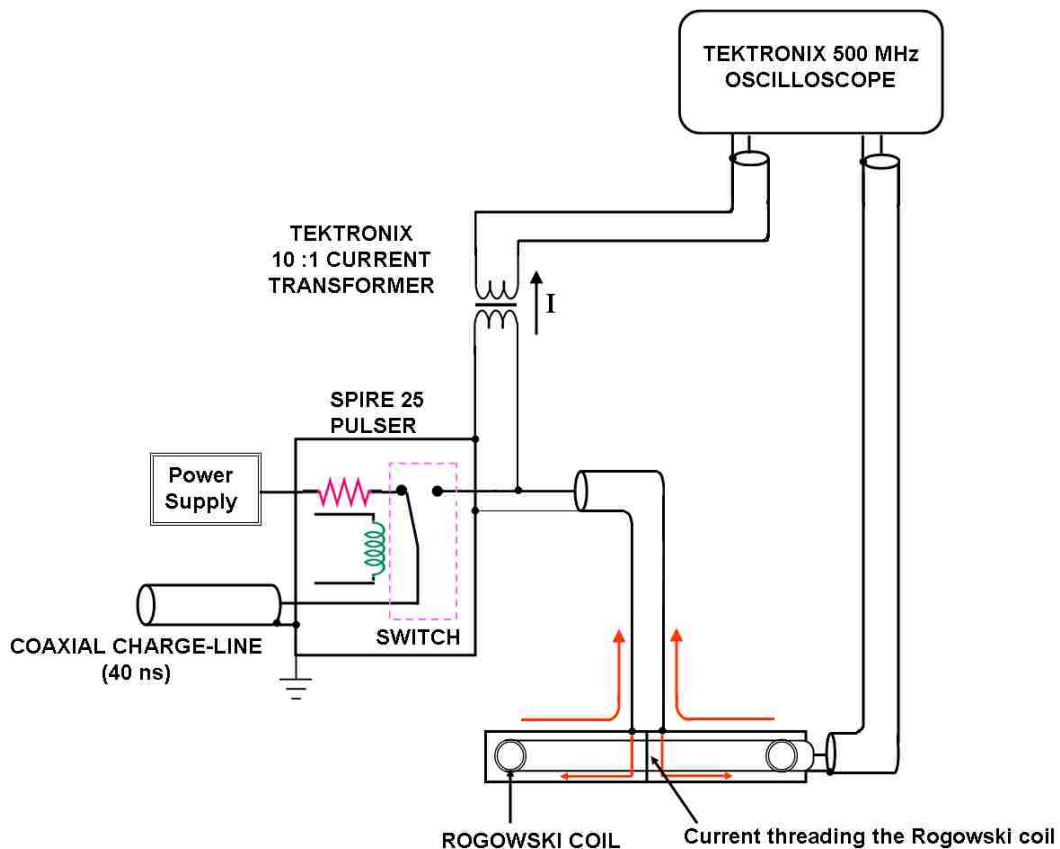


Figure 4-32 Schematic of coil calibration setup.



Figure 4-33 shows the traces obtained from the calibration setup. The Rogowski current trace matches the current transformer trace fairly well. The coil sensitivity was estimated to be  $26 \text{ A/V} \pm 0.5$  for both coils.

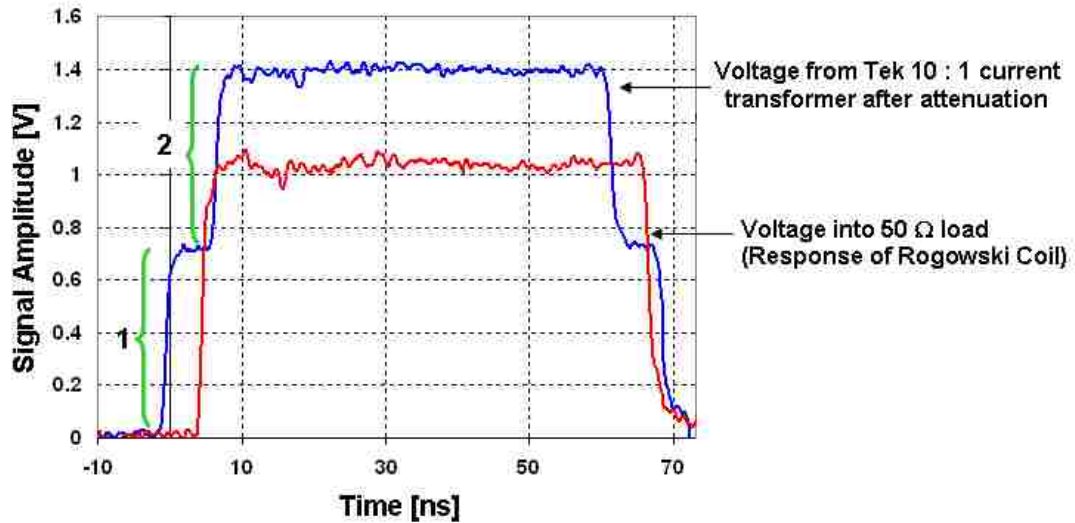


Figure 4-33 Rogowski coil response versus the response of a Tektronix current transformer.

The labels 1 and 2 on the blue trace represent the outgoing current step and the return current step, respectively.

#### **4.4.7 Directional Coupler for Microwave Power Measurements**

A comprehensive study of various methods of measuring microwave power has been neatly outlined in [67-70]. Among all the methods available an E-band loop-type directional coupler was used at UNM for characterizing the microwaves extracted from the magnetron. The principle of operation of the loop-coupler will be discussed briefly in the section to follow.

#### **4.4.8 Principle of Operation of the Loop Coupler**

A loop coupler consists of a segment of an auxiliary conductor located within a waveguide section and brought out through the wall to the desired connectors or terminations. The plane of the loop is normally approximately parallel to the axis of the main line to which the loop is coupled.

A rough idea of the operating principle can be obtained from Fig. 4-34. An electromagnetic wave in the guide will generate currents in the cables A and B because (1) the loop acts as a capacitance probe and responds to the passing electric field, and (2) the time changing magnetic field of the passing wave links the loop and generates a voltage.

The instantaneous direction of the current due to the electric field is the same at both ends of the loop while the current in A due to the magnetic field is opposite in direction to that in cable B. For the forward wave in the guide these currents will tend to cancel in cable B and add in cable A, while for the reflected wave there will be currents that cancel in A and add in B. The following relations must be maintained for satisfactory directional properties [70]:

- (1) The loop dimensions must be small compared to a quarter wavelength. This makes them less sensitive to small changes in frequencies.
- (2) The ends of the loop must each be terminated in a purely resistive load.
- (3) The loop must be small enough so that the reactance due to its self-inductance is small compared to the characteristic impedance of the cables.

(4) The geometry of the loop must be such that the current caused by the magnetic field in the guide or coaxial line has the proper phase and magnitude with respect to the current caused by the electric field.

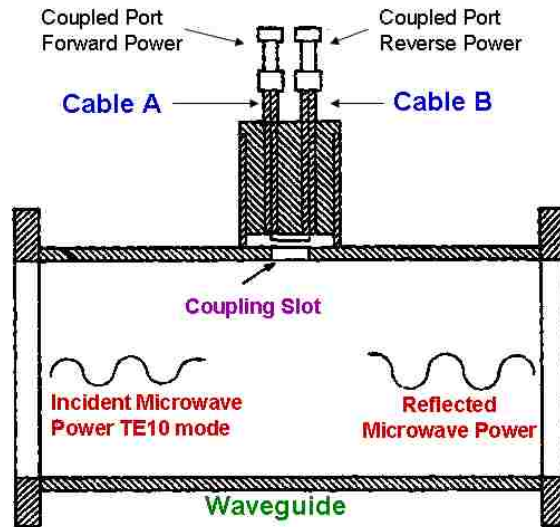


Figure 4-34 Cross-sectional view of a typical loop directional coupler [70].

#### 4.4.9 WR 229 Dual Monitor Directional Coupler

The E-band (WR-229) loop coupler used at UNM for magnetron experiments was manufactured by Mesa equipment. Two ports were made, each tuned to the transparent cathode and solid cathode frequency obtained from the MAGIC simulations, i.e. 3.6 GHz and 4.0 GHz, respectively. Both ports were designed to operate with a forward coupling coefficient of 70 dB, directivity of 27dB and have a power handling capability of ~1 GW. The calibration chart, i.e. coupling versus frequency response of the coupler in E-band (3.3– 4.9 GHz) can be found in Appendix 4. A low loss RG-213-type coaxial cable was used to deliver the RF signal from the directional coupler port to a 12 GHz Tektronix Digital Oscilloscope.

Figure 4-35 is a typical RF signal picked up from the directional coupler. The total RMS microwave power was calculated from Eq. 4-4-1

$$P = \frac{V^2}{2R} A \quad (4-4-5)$$

where V: is the peak voltage

R: 50  $\Omega$  (internal termination of the oscilloscope)

A: is the total attenuation.

The total attenuation A was calculated by taking the sum of the forward coupling of the directional coupler, attenuation in the coaxial cable and additional attenuators.

#### 4.4.10 Microwave Frequency

Typically high frequency measurements involve the use of the heterodyne technique. This technique requires a very precise knowledge of the frequency to be measured and is not suitable in systems that may have multiple frequencies present. For the experimental results reported in this dissertation a 12 GHz bandwidth, Tektronix oscilloscope was used. Since the frequencies to be measured (3.6 GHz and 4.0 GHz) fell well within the range of the bandwidth of the oscilloscope the RF frequency was calculated simply by performing a fast Fourier transform on the data using MATLAB.

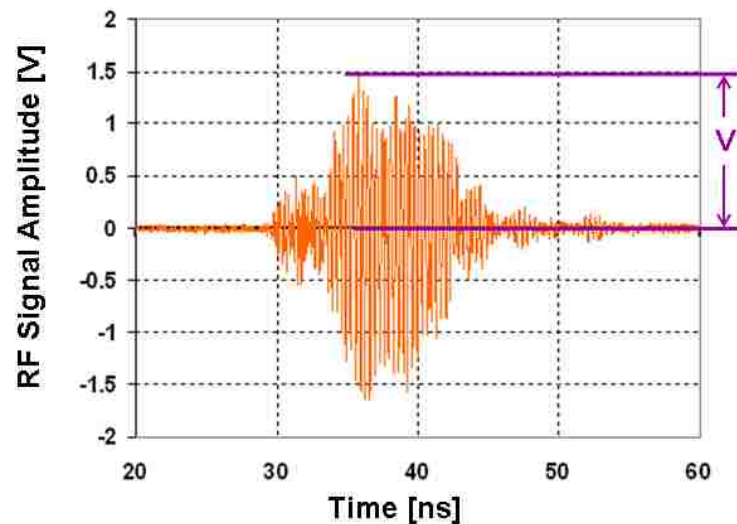


Figure 4-35 RF signal picked up by the directional coupler.

## Chapter 5

### Experimental Results

In this chapter the experimental procedure will be described followed by the experimental result where the performance of the A6 magnetron with the transparent cathode and the solid cathode are compared.

#### 5.1 Experimental Setup and Procedure

A dry turbo pumping system (Varian TPS-Compact TV81) with a pumping speed of 81 l/s was used to pump the vacuum chamber and the magnetron experimental setup down to reasonable vacuum levels. Experiments were conducted when the vacuum pressure was in the lower  $10^{-5}$  Torr range (typically between  $1 \sim 2 \times 10^{-5}$  Torr).

The cathodes used in the experiments were constructed of low porosity, vacuum compatible POCO graphite. Graphite was the material of choice because of its good field emission characteristics, small erection delay and ease of machining.

The anode block and the vacuum chamber were constructed of type 304 stainless steel. Stainless steel was chosen because it is vacuum compatible and is less prone to erosion by strong electron bombardment. Most anode blocks are constructed of copper due to its high electrical conductivity and therefore would cause less RF losses. Even though stainless steel is more resistive than copper, studies have shown that there was no difference in the output power obtained from a magnetron constructed of either material [7]. Photographs of the transparent cathode, solid cathode and the magnetron anode block that were fabricated in the laboratory are shown in Fig. 5-1.

The coils were energized with a 10 kV, 4.5 kJ capacitor bank. The discharge of this capacitor bank was synchronized such that SINUS-6 fired at the peak of magnetic field. By varying the magnet capacitor bank charge voltage, the magnetic field in the interaction space could be varied from 0 – 0.68 T. Because the time scale for the magnetic field pulse was 18.5 ms the magnetic field was essentially DC during the period of interest (12 ns).

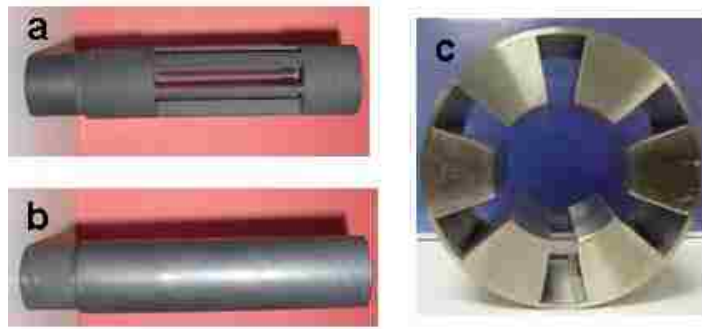


**Figure 5-1 Photographs of a) transparent cathode, b) solid cathode, and c) A6 magnetron manufactured at UNM.**

The trigger timings for starting the charging of the capacitor banks and the firing of the accelerator are shown in Fig 5-2 below. The sinusoidal trace shows the current in the RLC circuit when the capacitor energy is discharged into the coils and is measured by a low inductance, low resistance current viewing resistor.

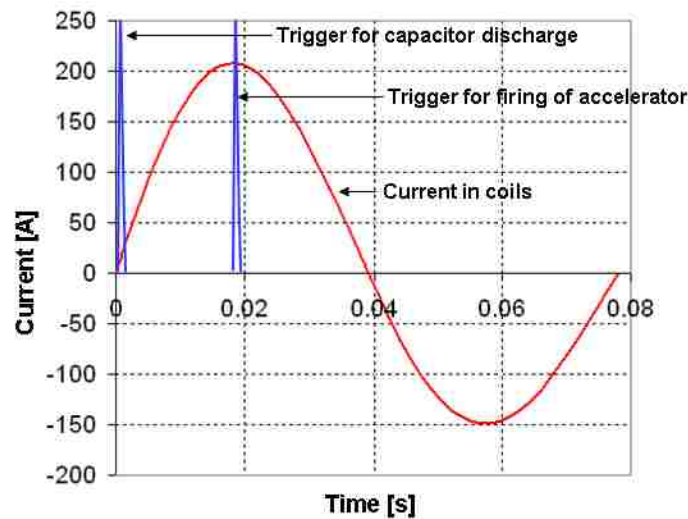


**Figure 5-2 Trigger timings and current in the RLC circuit.**

The experiments were conducted at constant voltage (260 kV) over a range of magnetic field (B-field). As the B-field was varied one would expect the diode voltage to vary as well. However, in order to effectively characterize magnetron operation both the

simulations and experiments must be conducted at the same voltage. This was easily accomplished in the simulations using the “circuit” option in MAGIC that maintains a constant applied voltage, the effect of which is equivalent to that of a ballast resistor. In experiments usually the output line is applied to a parallel combination of the magnetron and a liquid ballast resistor with variable resistivity [35, 36]. The resistor can be adjusted to compensate for variations in the line voltage and thereby provide a matched load to the pulser. Ballast resistor has the property of increasing in resistance as current flowing through it increases, and decreasing in resistance as current decreases. It therefore tends to maintain a constant current flowing through it, despite variations in applied voltage or changes in the rest of the circuit.

The diode voltage on SINUS-6 is determined by the gas pressure of the gas breakdown switch located downstream of the PFL. In the experiments conducted at UNM, to keep the charging voltage constant between shots as well as with changing magnetic field the gas pressure was adjusted accordingly. Even at constant gas pressure large shot-to-shot variation in the voltage was observed. Therefore, to ensure reproducibility of diode and microwave operating characteristics, the voltage trace was carefully monitored on the oscilloscope and data from 10 shots that were within  $\pm 5$  kV range of the desired applied voltage were recorded. Schematic of the experimental setup is shown in Fig. 5-3.

Diode voltage was measured using a capacitive divider probe located in the downstream region of the transmission line before transitioning into vacuum. While capacitive divider probes are very effective ways of measuring high voltages they do not perform very well in vacuum regions [35]. Two Rogowski coils located upstream and downstream of the magnetron were used to measure the total current and leakage current, respectively. The anode current was taken as the difference of the two readings assuming that the upstream leakage current was negligibly small. The microwave power was measured by taking a sample of the RF signal in the waveguide using the directional coupler. The frequency was determined by taking the FFT of the RF signal.

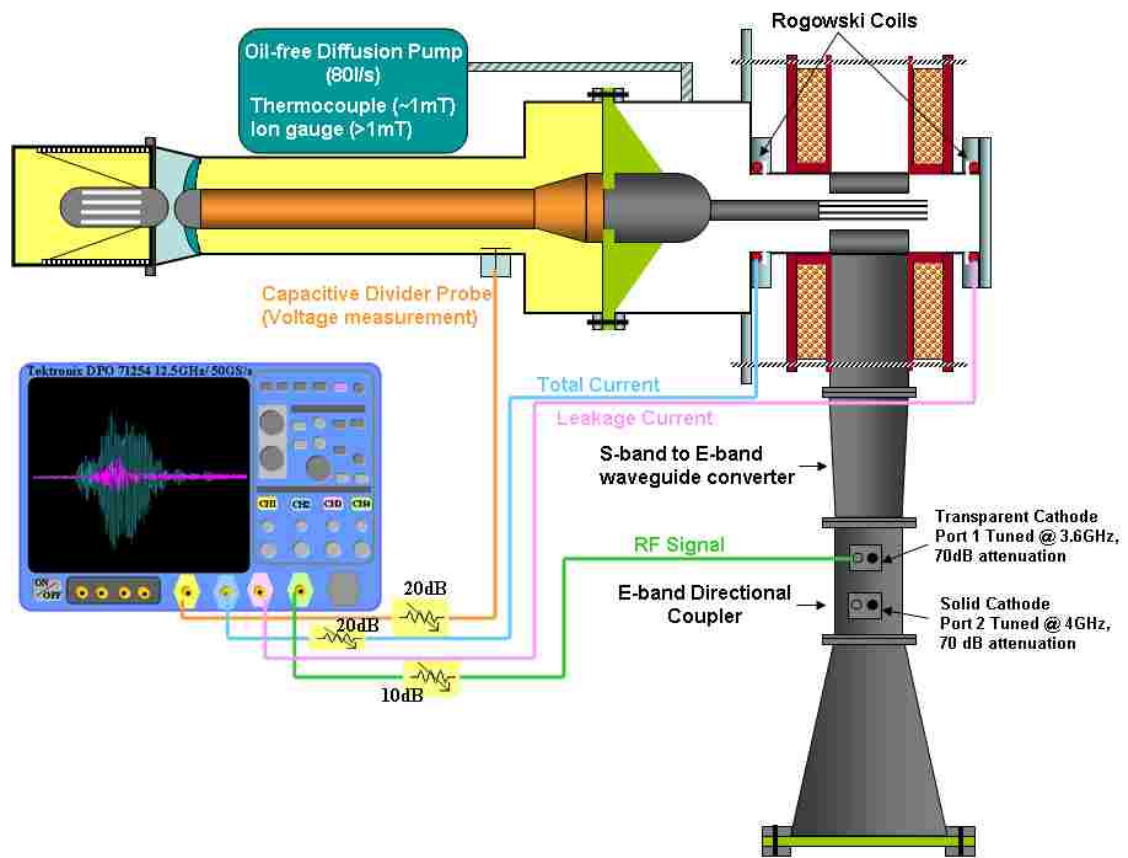


Figure 5-3 A schematic of the experimental setup.



## 5.2 Experimental Results

The experimental results are presented in this section. Provisions are made for removing the metal endcaps which allowed examination of operating characteristics in the presence of endcaps. Experiments conducted without endcaps yielded very small RF signals. Strong RF signals were attained with both endcaps in place as seen in other experiments [7, 35]. All the results presented in this chapter were taken with both endcaps in place for both cathodes.

The experiments conducted with the solid cathode were straightforward. However, since the transparent cathode performance is sensitive to the azimuthal orientation of the cathode strip the first experiments were conducted with the cathode strips located at the optimal angle as predicted by the simulations. Curiously enough the measured microwave power was very small. An azimuthal scan of the cathode strips was conducted in order to find optimal power. It was found that the magnetron with transparent cathode operated most efficiently when the cathode strips were directly under the cavity. This contradicted the initial simulation results and will be explained in the next section.

Figure 5-4 shows the voltage and diode current measurements with respect to the applied magnetic field for the transparent cathode. Similar voltage-current characteristic can be found for the solid cathode in Fig. 5-5. The voltage was kept constant at 260 kV while the magnetic field was varied from 0.35 T to 0.55 T. For each magnetic field value data for 10 shots that fell within  $\pm 5$  kV of 260 kV was recorded. As expected, the anode current decreases with increasing magnetic field. A maximum anode current of 8.4 kA was measured for the transparent cathode while the diode current reached only 3.5 kA for the solid cathode. The very low anode current is due to severe mode competition as will be seen later.

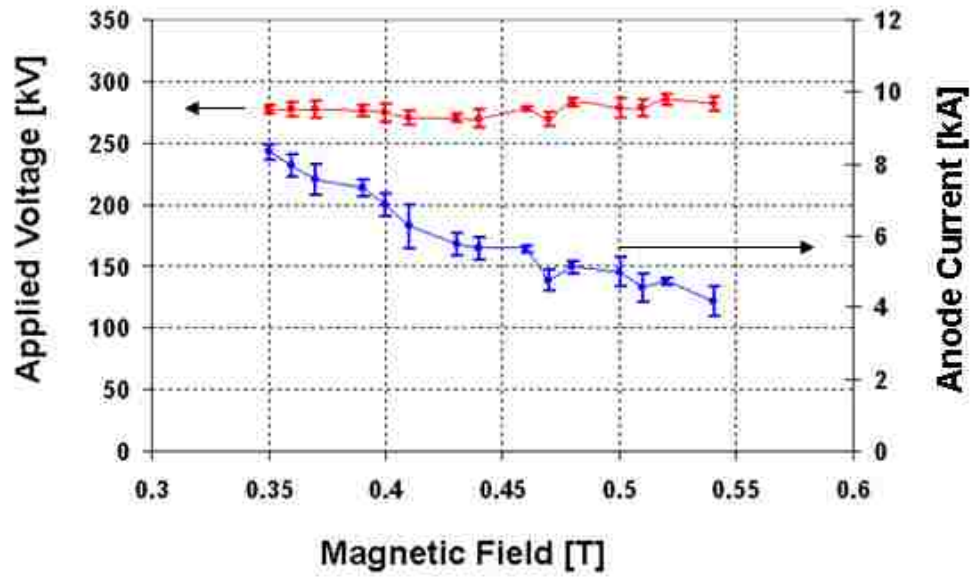


Figure 5-4 Voltage and current measurements with respect to magnetic field for the transparent cathode.

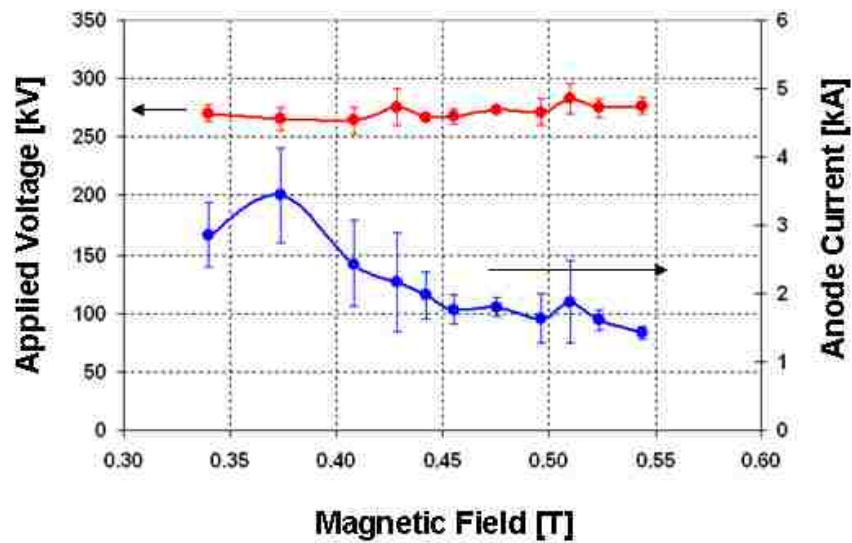


Figure 5-5 Voltage and current measurements with respect to the magnetic field for the solid cathode.

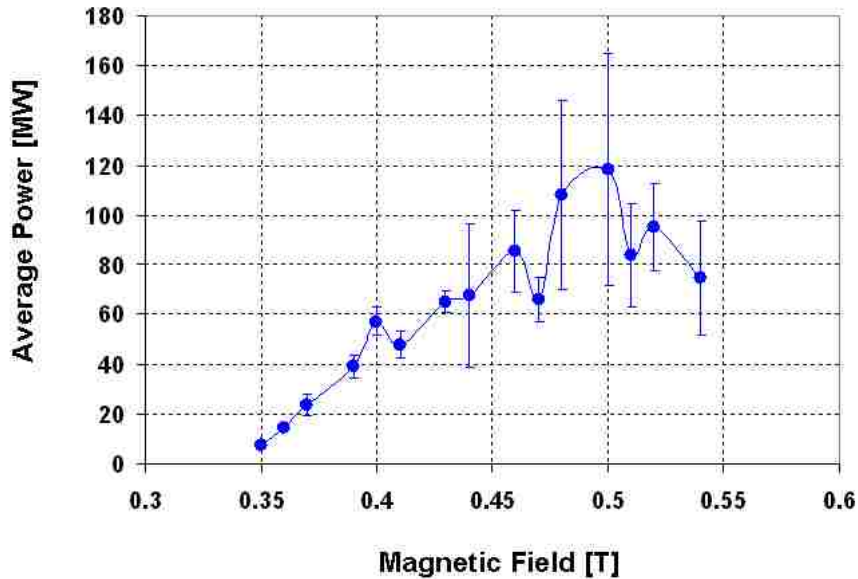


Figure 5-6 Average RMS power as function of magnetic field for the transparent cathode when  $V = 260$  kV.

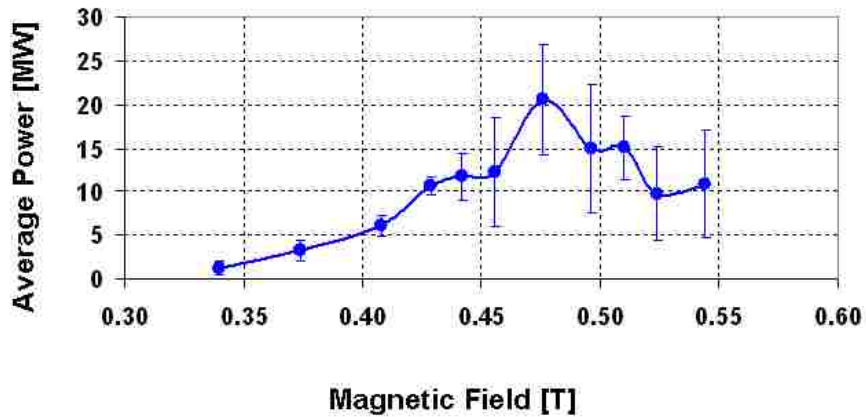
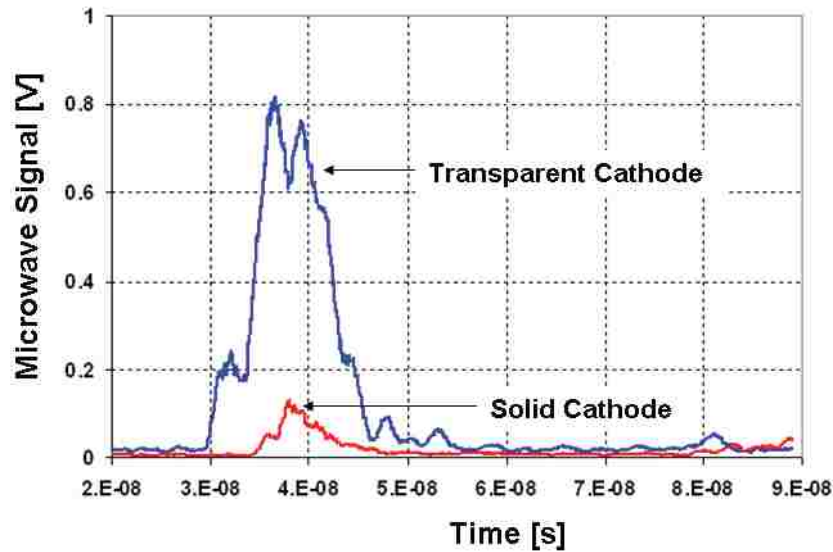


Figure 5-7 Average RMS power as function of magnetic field for the solid cathode when  $V = 260$  kV.

The power measurements tend to be a point of confusion in microwave work. The power levels presented in this work are in general the RMS power for comparison with simulation results. Figures 5-6 and 5-7 show average RMS power as a function of magnetic field for the transparent and solid cathode, respectively. The transparent cathode delivered a maximum average power of 170 MW, while solid cathode reached a maximum of 28 MW. The maximum power occurs at  $B_z = 0.5$  T for the transparent cathode and  $B_z = 0.47$  T for the solid cathode.



**Figure 5-8 Average RF envelopes for the A6 magnetron driven using a transparent and solid cathode.**

Figure 5-8 shows the radiated RF envelope obtained experimentally from the transparent and the solid cathode at the optimal magnetic field discussed above. Fast start and rate of build-up of oscillations are evident in the case of the transparent cathode compared to the traditional solid cathode, as predicted from the simulations. The maximum instantaneous power was 320 MW with an electronic conversion efficiency of 25% was extracted from the transparent cathode. On the other hand solid cathode produced a maximum instantaneous power 52 MW with an electronic conversion efficiency of 11%.

The total energy contained in the pulse is much greater for the transparent cathode compared to the solid cathode. This feature is attributed to the fast and rate of build-up of oscillations in the transparent cathode. For the solid cathode the slow start of oscillations does not give enough time for the microwave pulse to reach a high enough power for the duration of the applied voltage pulse.

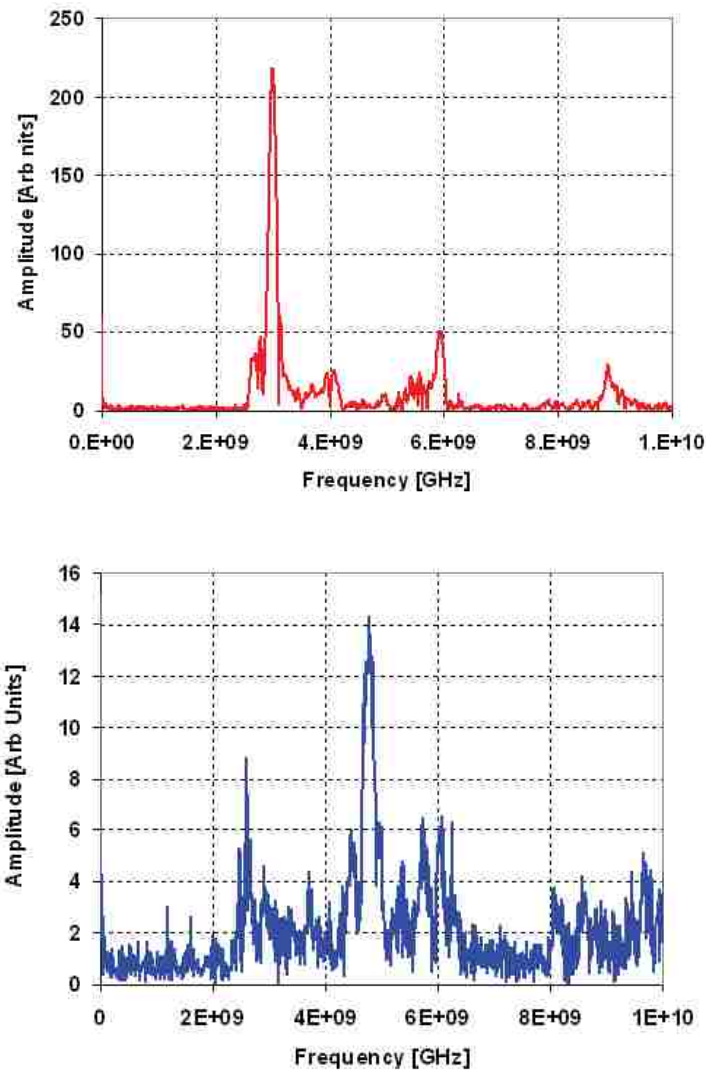


**Figure 5-9 FFT of the RF signal for the A6 magnetron driven by a transparent cathode (top) and a solid cathode (bottom).**

The FFT of the RF signal showed single mode operation at a frequency of 2.9 GHz for the magnetron driven by the transparent cathode whereas several peaks of comparable amplitudes and different frequencies are evident in the case of the solid cathode, indicating severe mode competition. The time frequency analysis provided in Appendix 3 shows a relatively pure field configuration for the transparent cathode while there is clear mode competition in the case of the solid cathode.

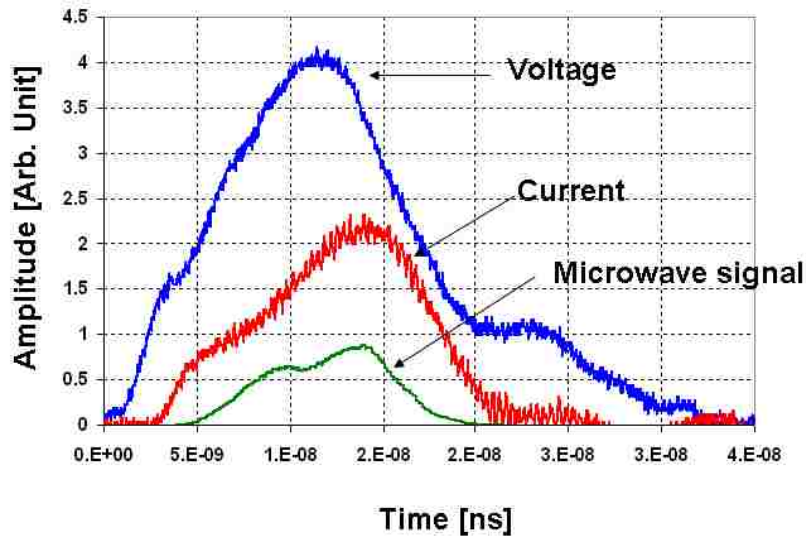


**Figure 5-10 Synchronized voltage, current, and microwave signals for the transparent cathode.**

The information on the applied voltage, current and power could not be measured at the same physical point in the experimental setup. Figure 5-10 shows the synchronized signals. From this graph it can be inferred that the microwave signal starts with a 1ns delay after the onset of current in the circuit for the transparent cathode.

Even though the transparent cathode displayed faster start and build-up of oscillations, single-mode single-frequency oscillations and overall higher output powers compared to the solid cathode, there was a notable difference in some parameters observed experimentally and those predicted by the simulations. Table 5.1 is a summary of the observed differences. The next section is an attempt to explain these differences.

**Table 5.1 Comparison of results predicted by simulations and observed experimentally**

Quantity	Transparent Cathode		Solid Cathode	
	Predicted	Observed	Predicted	Observed
Strip position	5 deg off-centered under vane	Under cavity	-	-
Frequency	4.0 GHz	2.9 GHz	3.6 GHz	Multiple Frequencies
Mode	$2\pi$	$\pi$ (anticipated)	$2\pi$	Mode Competition
Max. Power	600 MW	120 MW	200 MW	28 MW

**5.3 Supplementary MAGIC Simulations**

During the fabrication process the magnetron anode block underwent intense thermal stress due to welding. This resulted in slight magnetron geometry distortion. Supplementary MAGIC simulations were conducted on the distorted geometry in order to clarify the experimental results. Figure 5-11 shows the MAGIC graphics output for the distorted magnetron in the  $r-\theta$  plane. The cathode strips were placed directly under the cavity which was the optimal position from the experiments. The time evolution of spoke formation, shown in Fig. 5-12 shows three-fold symmetry indicative of the  $\pi$ -mode. The frequency of operation was 2.9 GHz, thereby confirming the experimental results.



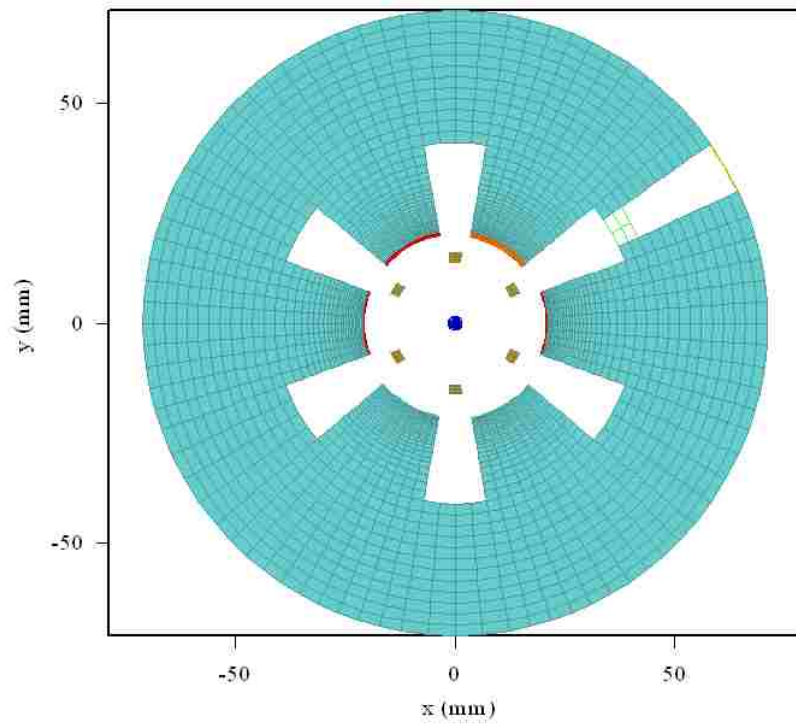


Figure 5-11 The r- $\theta$  view of the distorted magnetron modeled in MAGIC.

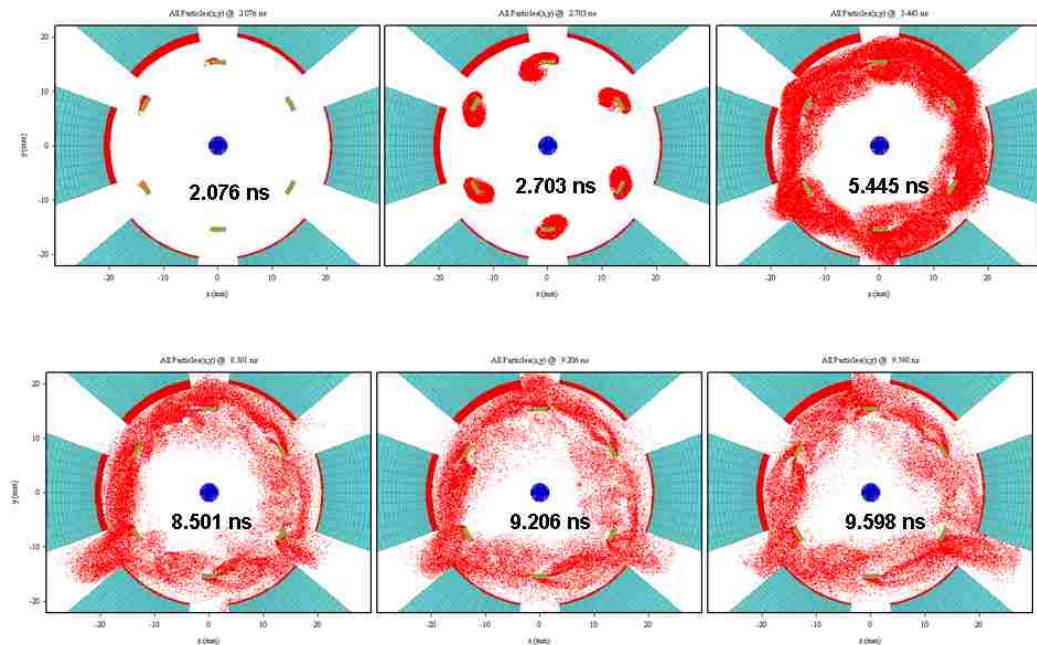


Figure 5-12 Time evolution of spoke formation in the distorted magnetron.



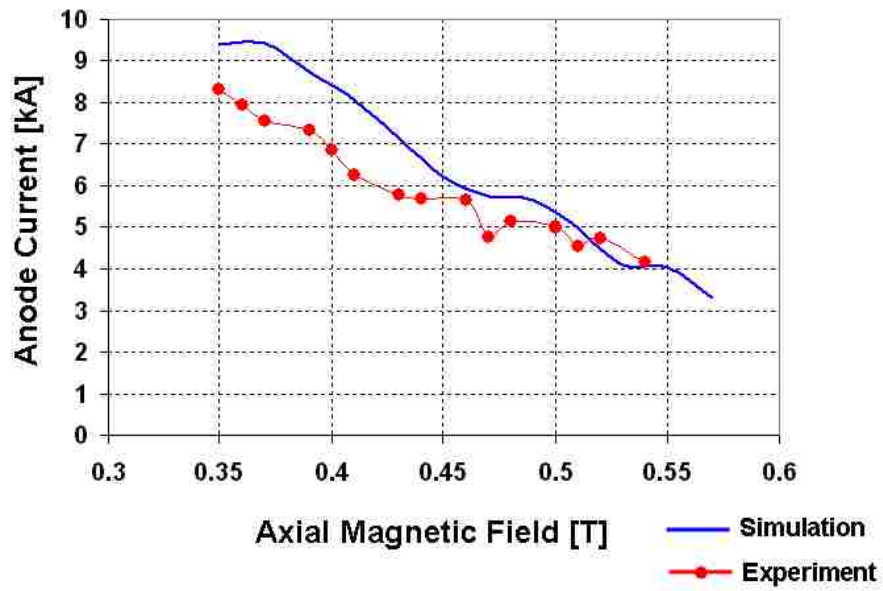


Figure 5-13 Anode current as a function of axial magnetic field.

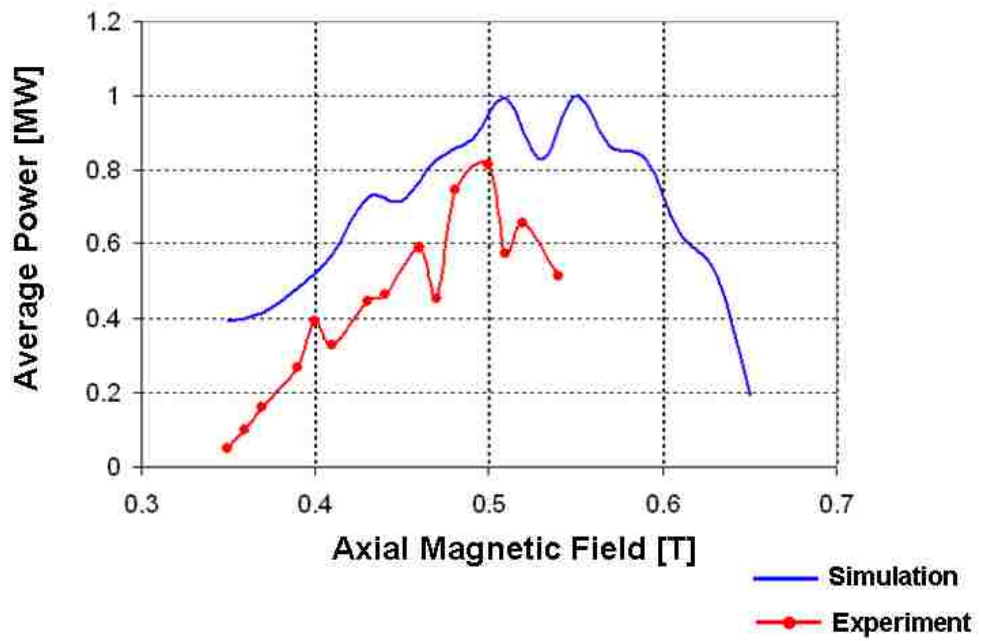


Figure 5-14 Average microwave power as a function of axial magnetic field.

Figure 5-13 is a comparison of experimental and simulation results for the anode current as a function of the applied magnetic field. Figure 5-14 is a comparison of average microwave power as a function of the applied magnetic field for the results obtained experimentally and those generated from the simulations. The results are in good agreement. A maximum average power of 145 MW was achieved at 0.51 T in simulations while the maximum average power of 120 MW was measured at 0.5 T in experiments. This difference could be attributed to the lower anode current measured in the experiments. The low anode current could be the result of the cathode material having a finite conductivity. In simulations the cathode is modeled as a perfect conductor.

It was observed in a magnetron setup which initially favored  $2\pi$ -mode oscillation that a coaxial misalignment of 0.4 mm in the A-K gap leads to mode competition. It can thus be inferred that magnetron oscillation the  $2\pi$ -mode is very sensitive to the A-K gap uniformity. The transparent cathode geometry is such that it would give equal opportunity for the growth of any mode provided its synchronous condition is met. Optimizing the cathode strip position leads to magnetron oscillation the  $\pi$ -mode. The optimal strip position being under the cavity could be explained using the argument presented in [7] which states that for a mode to form there has to be an equal mix of the RF radial and azimuthal electric field. This condition would best be satisfied if the cathode strip were directly under the cavity for the distorted magnetron geometry.

A possible reason for the low power levels in the  $\pi$ -mode is the asymmetric manner in which power is extracted. Since only one resonator is heavily loaded the three-fold symmetry may be partially destroyed.

## Chapter 6

### 6-1 Conclusions

A transparent cathode was proposed to improve the start time and rate of build-up of oscillations in a short-pulse relativistic magnetron. The transparent cathode consists of separate longitudinal metal strips, arranged to form a cylindrical surface that act as individual electron emitters. Favorable prebunching of electrons to excite the desired operating mode is provided by a suitable choice of the number and azimuthal position of the cathode strips. The strong azimuthal RF electric field in the cathode region rapidly captures the prebunched electrons into rotating spokes thereby providing improved conditions for fast conversion of the electrons' potential energy into electromagnetic energy.

The causes of slow start and build-up of oscillations was outlined followed by a conceptual study of transparent cathode geometry. Three-dimensional particle-in-cell simulations were performed on an A6 magnetron with a transparent cathode and a solid cathode for comparison. The A6 magnetron was the first and the most studied relativistic magnetron. The fidelity of the simulation results was justified by choosing simulation variables (e.g. grid resolution, time-step) whose output closely represented the experimental results previously published on the A6 magnetron [7]. Once the simulation parameters were optimized the solid cathode was replaced with a transparent cathode. The simulation results immediately confirmed fast start and rate of build-up of oscillations. These simulations were carried out with a voltage pulse of rise-time 10 ns.

Studies elsewhere have shown that the excitation of oscillations in crossed-field devices depend largely on the characteristic cavity fill-time and the rise time of the applied voltage. It is known from published data that the cavity fill-time for the  $\pi$ -mode and the  $2\pi$ -modes for the A6 magnetron are between 4 ~ 5 ns. Further investigation was conducted on magnetron performance for the two cathodes when the applied voltage pulse had a 1 ns rise-time. The difference between the output performance of the two cathodes was remarkable. The transparent cathode not only displayed faster start and rate of build-up of oscillations, but also produced output power of 1.2 GW where the solid cathode could only offer a maximum power of 600 MW. Furthermore, the magnetron

driven by the transparent cathode oscillated in the  $2\pi$ -mode over a very wide range of magnetic field.

The higher output powers could be explained in the following manner – the initial conditions for magnetron operation state that the electrons achieve an orbit near the cathode and then move at a velocity equal to the phase velocity of the RF field. In this frame of reference, the electrons have a residual drift from the RF field. The flow will drift so as to form two phases: the favorable phase and the unfavorable phase. In favorable phase electrons lose energy to the wave, and move toward the anode. In the unfavorable phase the particles gain energy from the RF wave, move toward the cathode and are reabsorbed; this process is dissipative and leads to overall RF losses. In the case of the transparent cathode due to the large gaps between the strips there is very little cathode surface for electron reabsorption in the unfavorable phase which, may account for higher output powers. The microwave power also depends on the RF volume. Since the transparent cathode geometry accommodates a larger RF volume this could also be stated as another reason for the observed higher output powers.

The reason for wider range of B-field could be attributed to the positioning of the cathode strips. As discussed in chapter 3 there is an optimal position of the cathode strip at which magnetron performance is preeminent. At this optimal position the DC priming effects combined with the DC  $\mathbf{E} \times \mathbf{B}$  drift ensure a constant supply of bunched electrons into favorable phase the RF field. Since the RF field pattern for a particular mode is independent of the applied axial magnetic field by positioning the cathode strip in the manner described above one allows a greater chance of the formation of the particular mode. Power is expected to fall as one deviates from the Hull cut-off and B-H conditions.

Despite the distortions in the magnetron that was tested experimentally the transparent cathode was still capable of showing fast start of oscillations, single-mode operation and higher output powers compared to the solid cathode. The transparent cathode oscillated in the  $\pi$ -mode as was confirmed by MAGIC simulations of the distorted geometry. The optimal cathode strip position for this magnetron was found to be under the cavities. For a magnetron to oscillate in the  $2\pi$ -mode the A-K gap uniformity is very critical [7]. The distortions of the magnetron anode block broke the symmetry and therefore it is reasonable that magnetron oscillation in the  $2\pi$ -mode was not detected.

Furthermore, the transparent cathode geometry is such that it allows an equal opportunity for the development of any mode that could be supported by the slow wave structure. Magnetron oscillation in the  $\pi$ -mode could have been favored as a result. As discussed in chapter 3 the requirement for spoke to form in a particular mode there has to be equal mix of the azimuthal and radial component of the RF electric fields. It can thus be inferred that locating the cathode strips under the cavity would meet this requirement for the  $\pi$ -mode. Furthermore, the difference in the phase velocities of the  $\pi$  and the  $2\pi$ -mode could also account for the optimal cathode strip position being different for the two modes. In order to justify this argument a more detailed analytical study of the different modes and their RF field configurations is necessary. A possible reason for the low power levels in the  $\pi$ -mode is the asymmetric manner in which power is extracted. Since only one resonator is heavily loaded the three-fold symmetry may be partially destroyed leading to low detected power.

## **6-2 Recommendations for Future Work**

The following points are recommended for future studies:

1. The A6 magnetron experiments should be conducted with a symmetric anode block and high degree of coaxial alignment between the anode and cathode.
2. In order to gain a deeper understating of the sensitivity of cathode strip position to the mode of operation analytical study of electron motion in different RF field configurations would be helpful.
3. The transparent cathode could have prospects in long-pulse operation. Its output performance, not being too impressive in the long pulse regime, could be attributed to large spread in electron energy that results during the voltage rise-time [72]. It would be interesting to investigate the electron distribution function of the space charge cloud for different voltage rise-times. Furthermore, simple simulations could be carried out with very high emission thresholds which may lead to a smaller spread in the electron distribution function and thereby improve the performance of the transparent cathode in the long pulse regimes.

## Appendix 1

### Design of Pulsed Magnetic Coil

#### A1-1 Forces Between Coils

It is necessary to calculate the forces between coils, as in the case of a Helmholtz pair with a gap, in which the required amount of support to be provided between the coils must be at least estimated. This can be easily accomplished by calculating the net force from an energy standpoint. The change in stored energy in the system following a virtual displacement of the coils is equal to the force between them times the distance moved; thus

$$\frac{dU}{dx} = F = \frac{c\Delta\left(\frac{1}{2}LI^2\right)}{\Delta x}, \quad (\text{A1-1})$$

where  $F$  = force in kilograms,

$\Delta L$  = change in inductance in Henrys,

$I$  = current in Amperes,

$\Delta x$  = displacement of the coils in centimeters,

$c = 10^2/9.8$ .

The system inductance will be made up of the individual inductances and the mutual inductance, that is,  $L = L_1 + L_2 + 2M$ ; it is the mutual inductance or coupling which changes when coils are moved.

### A1-2 Temperature Rise in Coil, $\Delta T_{\max}$

Near room temperature, the specific heat of conductors is nearly independent of temperature, and the temperature rise is related simply to energy U, the coil density, specific heat and volume v; thus

$$\Delta T_{\max} = \frac{U}{V} \cdot C \quad (\text{A1-2})$$

$\Delta T_{\max}$ : Temperature rise in °C

U : Energy dissipated in Joules

V : Volume of the windings in cm<sup>3</sup>

C : 0.292 for Copper and its alloys

In uniform-wound coils the entire conductor volume is involved and the peak temperatures are generally modest. Energy dissipated during the first half cycle is the energy stored initially minus that returned to the capacitor at the first negative peak.

$$U = \frac{1}{2} C (V_0^2 - V_1^2) \quad (\text{A1-3})$$

where C is the Capacitance,  $V_0$  is the initial charging voltage and  $V_1$  is the first negative peak voltage.

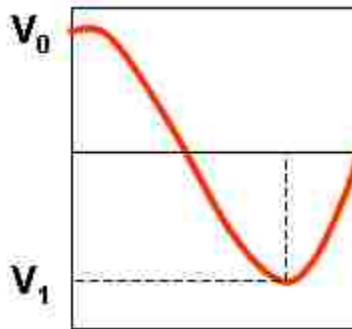


Figure A1 Discharge voltage of the capacitor bank into the coil.

## Appendix 2

### List of Formulas for Calculating Coil Parameters

The coil parameters summarized in Table 4.2 were calculated using the formulas and graphs provided in this section.

#### A2-1 Self Inductance

The self inductance for a coil with cross-section of winding space and homogeneous current distribution can be calculated using equation A2-1-1.

$$L_{self} = N^2 r_1 \Lambda(\alpha, \beta)$$

A2-1

$$\alpha = \frac{r_2}{r_1}, \beta = \frac{d}{r_1}$$

where  $\Lambda(\alpha, \beta)$ : is the self inductance factor and has units of  $10^{-9} \text{H.cm}^{-1}$  [49]. The value of  $\Lambda$  can be read off from Fig. A2-2. Figure A2-1 illustrates the dimensions that are necessary for calculating the geometrical factors  $\alpha$  and  $\beta$ .

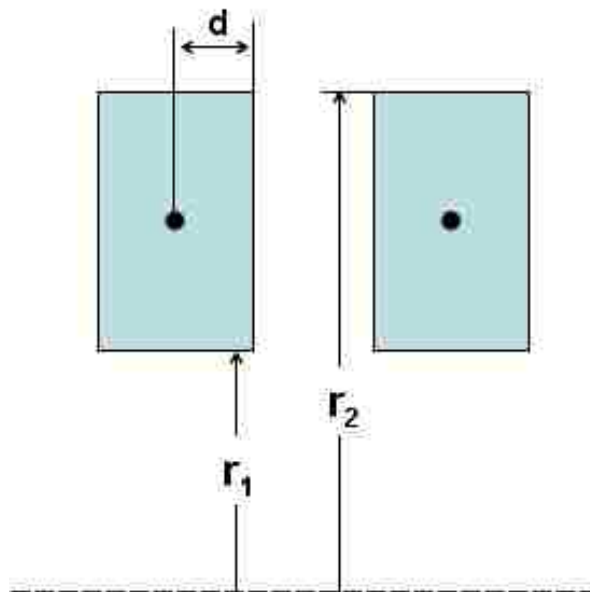


Figure 2A-1 Dimensions required fro calculating self inductance.



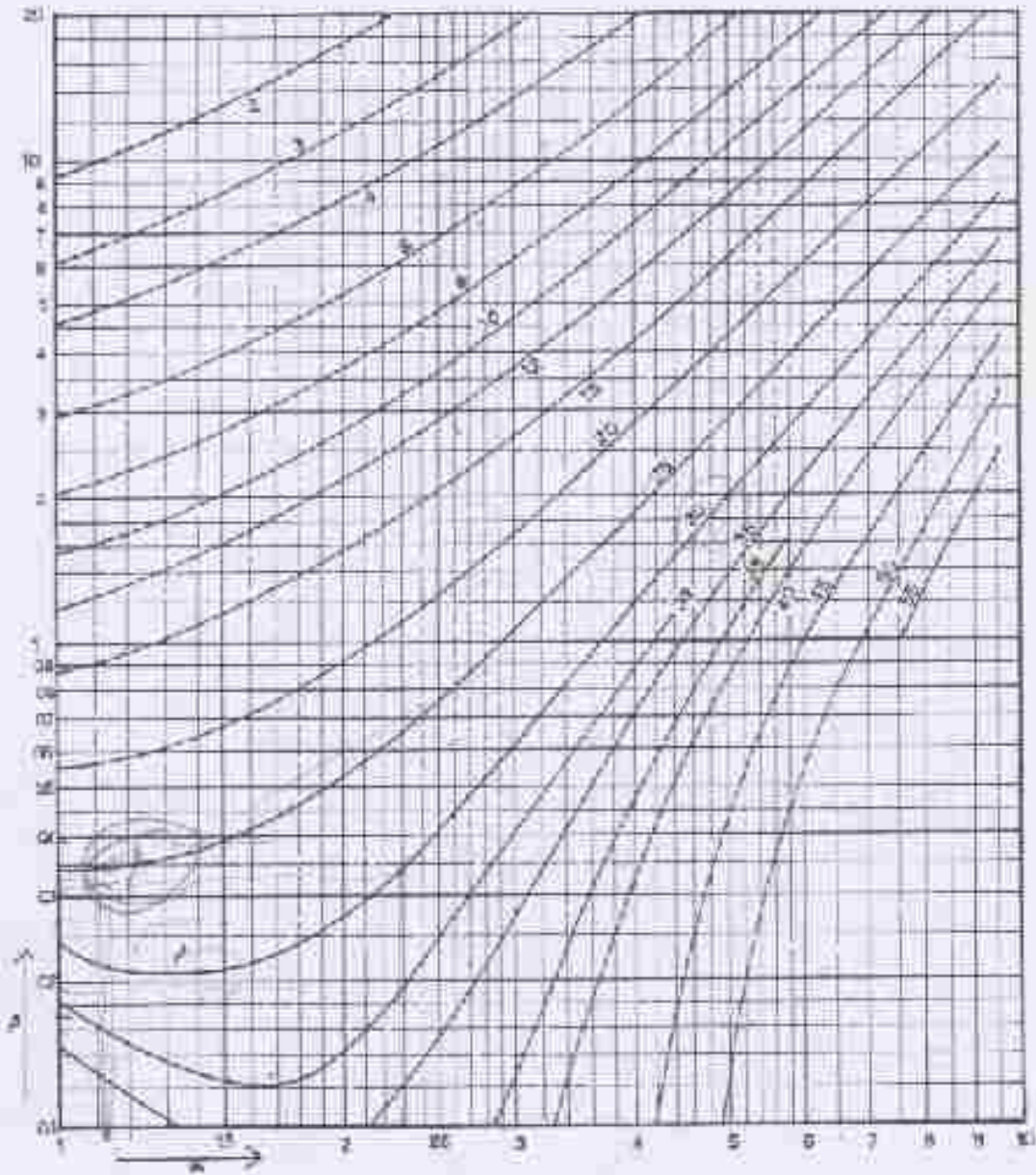


Fig. 86. Self-inductance factor  $A$  plotted against  $\alpha$  and  $\beta$ .  
 $A$  is given in units  $10^{-9}$  henry  $\text{cm}^{-1}$

Figure A2-2 The self-inductance factor plotted against  $\alpha$  and  $\beta$  [73].

## A2-2 Mutual Inductance

The mutual inductance formula was taken from [50]. The factor  $f$  can be obtained from Fig. 2A-4.

$$M = N^2 \cdot r \cdot f\left(\frac{d}{2r}\right) \quad 2A-2$$
$$f\left(\frac{d}{2r}\right):$$

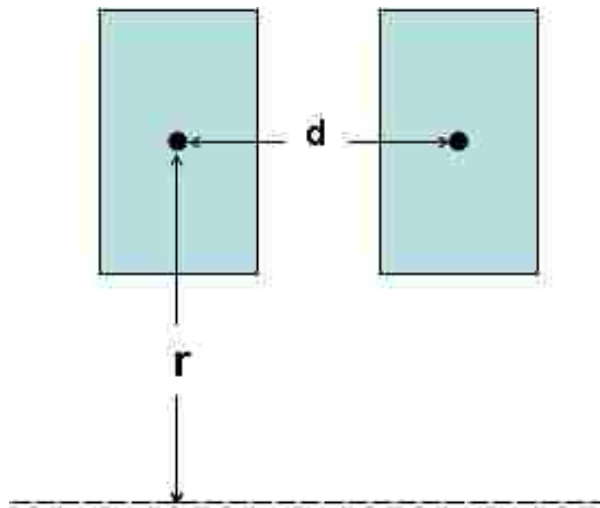


Figure A2-3 Dimensions required for calculating the mutual inductance.

## A2-3 Total Inductance

The formula for calculating the total inductance for two coils connected in series and is given by equation A2-3

$$L_{total} = L_1 + L_2 + 2M . \quad A2-3$$

MUTUAL INDUCTANCE OF COAXIAL CIRCULAR FILAMENTS 83

TABLE 16. VALUES OF  $f$  FOR EQUAL CIRCLES NEAR TOGETHER.

$$\delta = \frac{\text{distance}}{\text{diameter}} \approx 1.$$

$\delta$	$f$	Diff.	$\delta$	$f$	Diff.	$\delta$	$f$	Diff.	$\delta$	$f$	Diff.
0.01	0.05016	- 829	0.26	0.010723	- 383	0.51	0.004800	- 136	0.76	0.0024659	- 599
.02	.04147	- 508	.27	.010340	- 366	.52	.004664	- 132	.77	.0024060	- 581
.03	.03639	- 359	.28	.009974	- 347	.53	.004532	- 127	.78	.0023479	- 563
.04	.03290	- 277	.29	.009627	- 331	.54	.004405	- 122	.79	.0022915	- 547
0.05	0.03003	- 226	0.30	0.009296	- 314	0.55	0.004283	- 118	0.80	0.0022369	- 531
.06	.02777	- 189	.31	.008980	- 301	.56	.004165	- 114	.81	.0021838	- 515
.07	.02588	- 164	.32	.008679	- 289	.57	.004051	- 111	.82	.0021322	- 500
.08	.02424	- 143	.33	.008390	- 276	.58	.003940	- 106	.83	.0020823	- 486
.09	.02281	- 127	.34	.008114	- 264	.59	.003834	- 103	.84	.0020337	- 472
0.10	0.021539	- 1143	0.35	0.007850	- 253	0.60	0.003730	- 99	0.85	0.0019865	- 458
.11	.020396	- 1035	.36	.007597	- 243	.61	.003631	- 97	.86	.0019407	- 445
.12	.019361	- 944	.37	.007354	- 233	.62	.003534	- 93	.87	.0018962	- 432
.13	.018417	- 867	.38	.007121	- 223	.63	.003441	- 90	.88	.0018530	- 421
.14	.017550	- 800	.39	.006898	- 214	.64	.003351	- 88	.89	.0018109	- 408
0.15	0.016750	- 741	0.40	0.006684	- 207	0.65	0.003263	- 84	0.90	0.0017701	- 397
.16	.016009	- 690	.41	.006477	- 198	.66	.003179	- 82	.91	.0017304	- 386
.17	.015319	- 643	.42	.006279	- 190	.67	.003097	- 79	.92	.0016918	- 376
.18	.014676	- 603	.43	.006089	- 183	.68	.003018	- 77	.93	.0016542	- 364
.19	.014073	- 566	.44	.005906	- 176	.69	.002941	- 75	.94	.0016178	- 356
0.20	0.013507	- 532	0.45	0.005730	- 170	0.70	0.002866	- 72	0.95	0.0015822	- 345
.21	.012975	- 502	.46	.005560	- 164	.71	.002794	- 70	.96	.0015477	- 336
.22	.012473	- 473	.47	.005396	- 157	.72	.002725	- 68	.97	.0015141	- 327
.23	.012000	- 449	.48	.005239	- 152	.73	.002657	- 66	.98	.0014814	- 318
.24	.011551	- 425	.49	.005087	- 146	.74	.002591	- 63	0.99	.0014496	- 310
0.25	0.011126	- 403	0.50	0.004941	- 141	0.75	0.002528	- 62	1.00	0.0014188	

Figure A2-4 Values for factor  $f$  [74].

## Appendix 3

### Time Frequency Analysis of Experimental Data

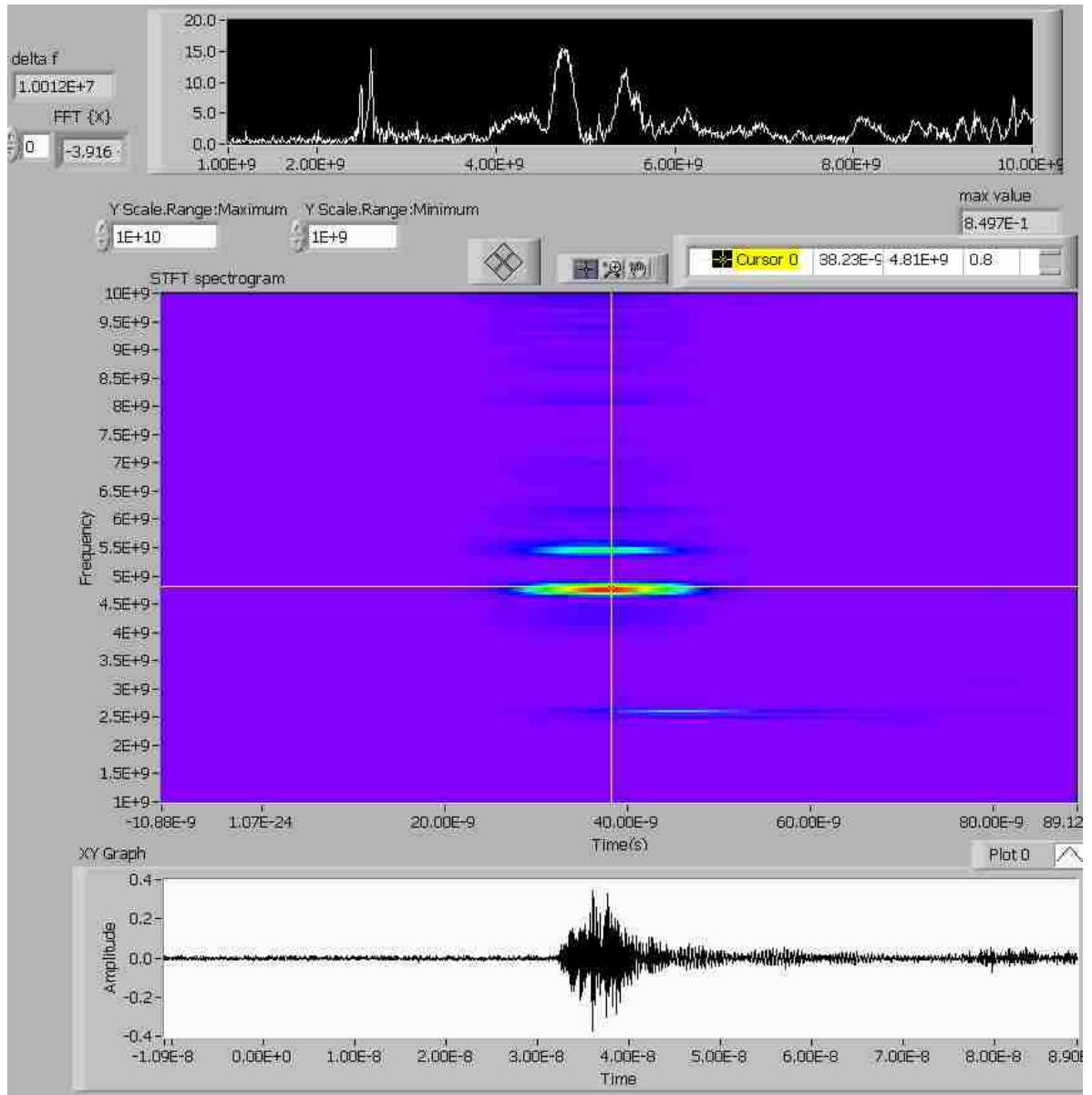
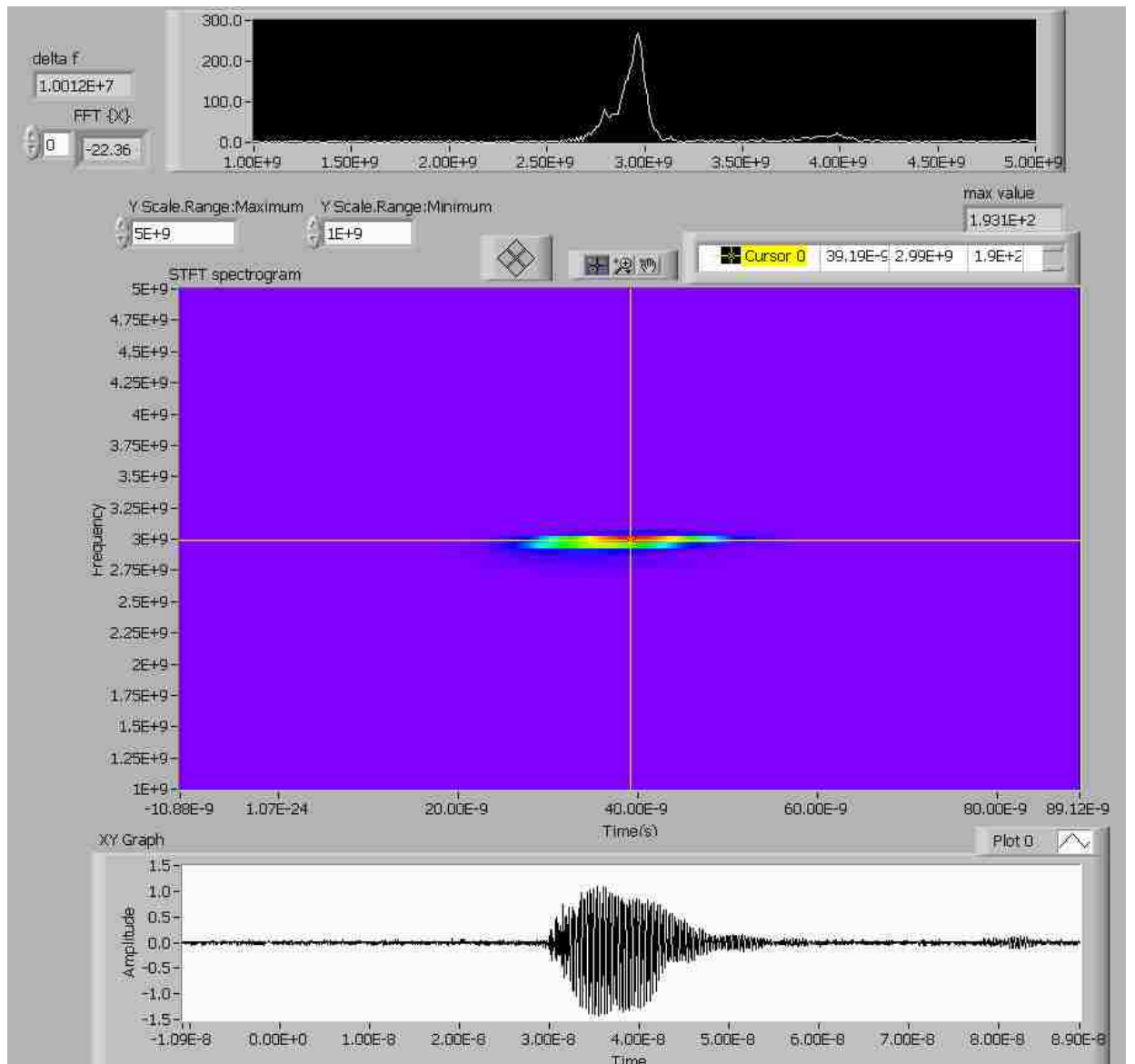


Figure A3-1 Time frequency analysis of experimental data for solid cathode.



**Figure A3-2 Time frequency analysis of experimental data for transparent cathode.**



## Appendix 4

### Calibration Data

#### A4-1 Calibration Data for the Directional Coupler

Figures 1 and 2 are the calibration data of the E-band directional coupler. The calibration was performed with a Vector Network Analyzer.

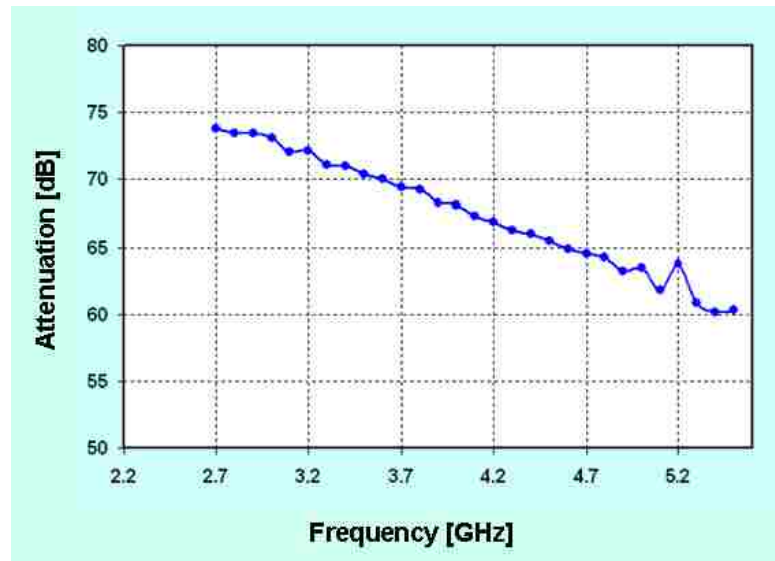


Figure A4-1 Calibration data for Port 1 of the E-band directional coupler. Port 1 was tuned for 70 dB attenuation at 3.6 GHz.

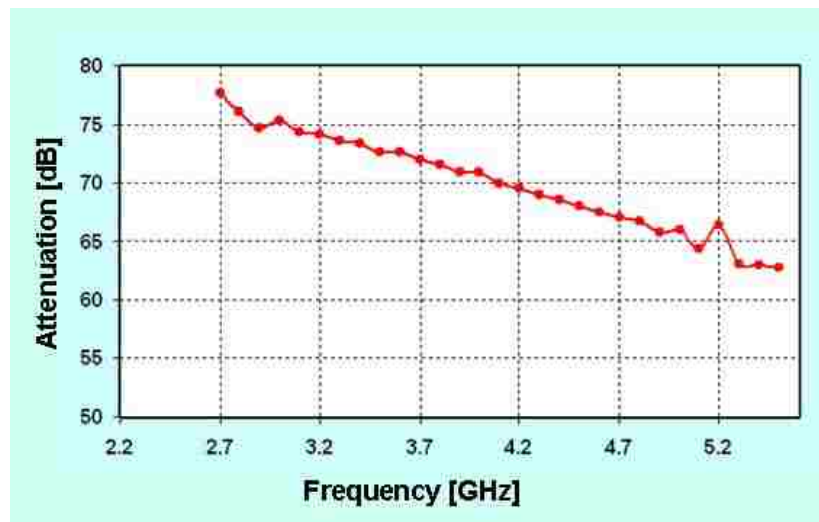
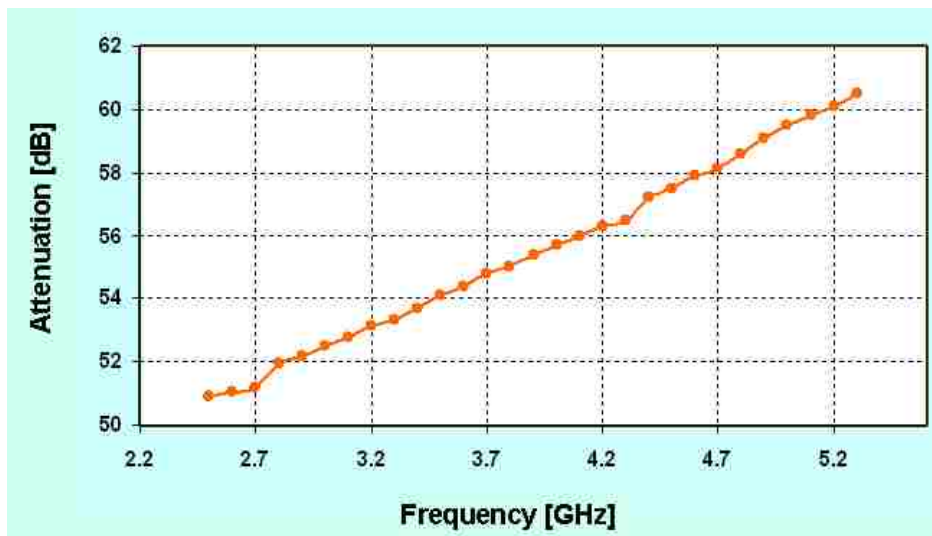


Figure A4-2 Calibration data for port 2 of the E-band directional coupler. Port 2 was tuned for 70 dB attenuation at 4.0 GHz.

## **A4-2 Calibration Data for the RG 213 Cables**

The RG 213 cable was chosen because it is low loss. The total length of the cable used to deliver the data from the directional coupler to the oscilloscope is ~15 ft. To calibrate such long cable the time scale on the network analyzer had to be adjusted to 3 ms.



**Figure A4-3 Calibration data for the RG213 Cable.**

## References

1. J. Benford, J. A. Swegle, and E. Schamiloglu, High Power Microwaves, 2nd Edition, New York:Taylor and Francis, 2007.
2. V. L. Granatstein and I. Alexeff, High-Power Microwave Sources. Norwood, MA: Artech House, 1987.
3. A. S. Gilmour, Jr., Microwave Tubes. Artech House, Inc, 1986, Chap. 13.
4. S. E. Tsimring, Electron Beams and Microwave Vacuum Electronics. John Wiley and Sons Inc., 2007, Chap. 9.
5. E. Okress, Ed., Crossed-Field Microwave Devices. New York: Academic, 1961, vol. 1, Chap. 1.
6. Microwave Magnetrons, G. B. Collins, ed. (Mc Graw-Hill, New York, 1948), Chap. 1.
7. A. Palevsky, "Generation of Intense Microwave Radiation by the e-Beam Magnetron (Experiment and Numerical Simulation)", Dissertation, Massachusetts Institute of Technology, Cambridge, MA 1980.
8. G. Bekefi, and T. J. Orzechowski, "Giant Microwave-Bursts Emitted from a Field-Emission, Relativistic Electron-Beam Magnetron," Physical Review Letters, vol. 37, no. 6, pp. 379-382, 1976.
9. G. Bekefi, and T. J. Orzechowski, "Relativistic Electron-Beam Magnetron," Bulletin of the American Physical Society, vol. 21, no. 4, pp. 571-571, 1976.
10. A.V.Gaponov-Grekhov, V.L. Granatstein, "Applications of High-Power Microwaves", Artech House Boston London, 1994.
11. A. Blyakhman, D. Clunie, R. Harris et al., "Nanosecond gigawatt radar: indication of small targets moving among heavy clutters."
12. R. C. Davidson, Physics of Nonneutral Plasmas, Addison-Wesley, Redwood City, CA, 1990.
13. Y. Y. Lau, in High-Power Microwave Sources, Eds.: V. L. Granatstein and I. Alexeff, ArtechHouse (Norwood, MA, 1987), p. 309.
14. Y. Y. Lau, J. W. Luginsland, K. L. Cartwright, D. H. Simon, W. Tang, B. W. Hoff, and R. M. Gilgenbach, "A re-examination of the Buneman-Hartree condition in a cylindrical smooth-bore relativistic magnetron", Phys, Plasmas 17, 033102 (2010).



15. R. V. Lovelace, and T. F. T. Young, "Relativistic Hartree Condition for Magnetrons - Theory and Comparison with Experiments," *Physics of Fluids*, vol. 28, no. 8, pp. 2450-2452, 1985.
16. Y. P. Blikoh, G. S. Nusinovich, A. G. Shkvarunets, and Y. Garmel, "Self-excitation of microwave oscillations in plasma-assisted slow-wave oscillators by an electron beam with a movable focus", *Phys. Rev. E* vol. 70, pp 046501 - 046509, 2004.
17. Y. M. Saveliev, W. Sibbett, and D. M. Parkes, "Self-excitation and operational characteristics of the crossed-field secondary emission electron source," *Review of Scientific Instruments*, vol. 70, no. 12, pp. 4502-4514, Dec, 1999.
18. M. Fuks and E. Schamiloglu, "Rapid start of oscillations in a magnetron with a "transparent" cathode," *Phys. Rev. Lett.* 95, 205101 (2005).
19. W. P. Ballard, "A Relativistic Magnetron with a Thermionic Cathode," Dissertation, Dept. of Applied Physics, Stanford University, Palo Alto, CA, 1981.
20. M. C. Jones, "Cathode Priming of a Relativistic Magnetron Using Multiple Emission Zones on Projection Ablation Lithography Cathode", Dissertation, Dept. of Nuclear and Radiological Sciences, University of Michigan, Michigan, 2005.
21. M. C. Jones, V. B. Neculaes, Y. Y. Lau, R. M. Gilgenbach, and W. M. White, "Cathode priming of a relativistic magnetron," *Appl. Phys. Lett.*, vol. 85, pp. 6332–6334, 2004.
22. V. B. Neculaes, "Magnetron Magnetic Priming for Rapid Startup and Noise Reduction", Dissertation, Dept. of Nuclear and Radiological Sciences, University of Michigan, Michigan, 2005.
23. V. B. Neculaes, R. M. Gilgenbach, Y. Y. Lau, M. C. Jones, and W. M. White, "Low-noise microwave oven magnetrons with fast start-oscillations by azimuthally varying axial magnetic field," *IEEE Trans. Plasma Sci.*, vol. 32, no. 3, pp. 1152–1159, Jun. 2004.
24. M. C. Jones, V. B. Neculaes, W. M. White, Y. Y. Lau, and R. M. Gilgenbach, "Simulation of rapid startup in microwave magnetrons with azimuthally-varying axial magnetic field," *Appl. Phys. Lett.*, vol. 84, pp. 1016–1018, 2004.
25. V. B. Neculaes, M. C. Jones, R. M. Gilgenbach et al., "Magnetic priming effects on noise, startup, and mode competition in magnetrons," *IEEE Transactions on Plasma Science*, vol. 33, no. 1, pp. 94-102, Feb, 2005.
26. J. I. Kim, J. H. Won, and G. S. Park, "Electron prebunching in microwave magnetron by electric priming using anode shape modification," *Applied Physics Letters*, vol. 86, no. 17, pp. -, Apr 25, 2005.

27. J. I. Kim, J. H. Won, G. S. Park et al., "Reduction of noise in strapped magnetron by electric priming using anode shape modification," *Applied Physics Letters*, vol. 88, no. 22, pp. 355-358, May 29, 2006.
28. J. I. Kim, J. H. Won, G.S. Park H. "Electron prebunching in microwave magnetron by electric priming using anode shape modification", *Appl. Phys. Lett.* 86 171501, 2005.
29. W. M. White, R. M. Gilgenbach, M. C. Jones et al., "Radio frequency priming of a long-pulse relativistic magnetron," *IEEE Transactions on Plasma Science*, vol. 34, no. 3, pp. 627-634, Jun, 2006.
30. H. Bosman, S. Prasad, M. Fuks et al., "Rapid startup in magnetrons using the transparent cathode," 2006 IEEE International Vacuum Electronics Conference held jointly with 2006 IEEE International Vacuum Electron Sources, IVEC/IVESC 2006. pp. 127-128.
31. H. Bosman, M. I. Fuks, S. Prasad and E. Schamiloglu, "Improvement of the Output Characteristics of Magnetrons Using the Transparent Cathode", *IEEE Trans. PlasmaSci.*, vol. 34, no. 3, pp. 606-619, Jun. 2006.
32. T. P. Fleming, P. J. Mardahl, L. Bowers et al., "Virtual prototyping of novel cathode designs for the relativistic magnetron," *Computing in Science and Engineering*, vol. 9, no. 6, pp. 18-28, 2007.
33. T. P. Flemming, P. J. Mardhal, L. A. Bowers, K. L. Cartwright, "Three Dimensional PIC Simulations of Novel Cathodes in the Michigan and AFRL Relativistic Magnetrons", *IEEE Trans.* vol. 1-4244 pp 401- 404, Aug. 2006.
34. T. P. Flemming, P. J. Mardhal, "Performance Improvements in the Relativistic Magnetron: The Effect of DC Field Perturbations", *IEEE Trans. Plasma Sci.*, vol. 37, 11 pp 2128-2138, Nov. 2009.
35. R. W. Lemke, and M. C. Clark, "Operating Characteristics of a Relativistic Magnetron with a Washer Cathode", *IEEE Trans. on Plasma Sci.*, vol. ps-15, no. 3, pp. 327-344, June, 1987.
36. R. W. Lemke, T. C. Genoni, and T. A. Spencer, "Three-dimensional particle-in-cell simulation study of a relativistic magnetron," *Physics of Plasmas*, vol. 6, no. 2, pp. 603-613, Feb, 1999.
37. MAGIC User's Manual, ATK Mission Research, Newington, VA [online] Available: <http://www.mrcwdc.com/Magic/>.
38. M. Daimon, K. Itoh, G. Imada et al., "Experimental demonstration of relativistic magnetron with modified output configuration," *Applied Physics Letters*, vol. 92, no. 19, pp. 191504-191504-3, May 12, 2008.

39. M. Daimon, and W. Jiang, "Modified configuration of relativistic magnetron with diffraction output for efficiency improvement," *Applied Physics Letters*, vol. 91, no. 19, pp. 191503-1 – 191503-3, Nov, 2007.
40. Y. M. Saveliev, W. Sibbett, and D. M. Parkes, "On anode effects in explosive emission diodes," *Journal of Applied Physics*, vol. 94, no. 9, pp. 5776-5781, Nov 1, 2003.
41. S. P. Bougaev, K. A. I. Kim A.A., and K. V.I., "Study of cathode plasma expansion in high-current magnetically insulated diodes," *High-Power Beams*, vol. 81, pp. 401-408, 1981.
42. "Sinus-6 repetitively-pulsed electron beam accelerator & high power microwave source: operation and maintenance manual," High Current Electronics Institute-Tomsk-Russia, pp. 1-41, June 1992, 1992.
43. V. P. Gubanov, and D. Grishin, "'Sinus-6" version 1.1," pp. 1-9, 2001.
44. S. T. Pai and Q. Zhang, "Introduction to High Power Pulse Technology", World Scientific Publishing Co. Pte. Ltd., 2003.
45. K. D. Bergeron, "Theory of Secondary-Electron Avalanche in Vacuum Flashover of Insulators," *Bulletin of the American Physical Society*, vol. 21, no. 9, pp. 1146-1146, 1976.
46. K. D. Bergeron, "Theory of Secondary-Electron Avalanche at Electrically Stressed Insulator-Vacuum Interfaces," *Journal of Applied Physics*, vol. 48, no. 7, pp. 3073-3080, 1977.
47. V. Belyaev, "Model of surface flashover of insulator in vacuum," *IEEE 18th Int. Symp. on Discharges and Electrical Insulation in Vacuum - Eindhoven*, pp. 4, 1998.
48. V. K. Belyaev, "Electric field and the charge distribution on the surface of an insulator in a vacuum," *Technical Physics*, vol. 50, no. 6, pp. 673-679, 2005.
49. J. M. Elizondo, K. Struve, B. Stygar et al., "Vacuum flashover characteristics of solid CL-polystyrene," *International Symposium on Discharges and Electrical Insulation in Vacuum - Tours*, pp. 4, 2002.
50. N. M. Jordan, Y. Y. Lau, D. M. French et al., "Electric field and electron orbits near a triple point," *Journal of Applied Physics*, vol. 102, no. 3, pp. 033301-1 – 033301-10, Aug, 2007.
51. K. R. Prestwich, "Comparison of vacuum insulator designs and of modified sinus accelerator with Marvin's fast rise time accelerator," *priv. comm*, 2007.

52. J. T. Krile, A. A. Neuber, J. C. Dickens et al., "DC flashover of a dielectric surface in atmospheric conditions," IEEE Transactions on Plasma Science, vol. 32, no. 5, pp. 1828-1834, Oct, 2004.
53. J. T. Krile, R. Vela, A. A. Neuber et al., "Pulsed dielectric-surface flashover in an SF<sub>6</sub> environment," IEEE Transactions on Plasma Science, vol. 35, no. 5, pp. 1580-1587, Oct, 2007.
54. W. A. Stygar, H. C. Ives, T. C. Wagoner et al., "Flashover of a vacuum-insulator interface: A statistical model," Physical Review Special Topics-Accelerators and Beams, vol. 7, no. 7, Jul, 2004.
55. W. A. Stygar, J. A. Lott, T. C. Wagoner et al., "Improved design of a high-voltage vacuum-insulator interface," Physical Review Special Topics-Accelerators and Beams, vol. 8, no. 5, May, 2005.
56. R. A. Close, A. Palevsky, and G. Bekefi, "Radiation measurements from an inverted relativistic magnetron", J. Appl. Phys., vol 54, p 4147, 1983
57. H. Sze, B. Hartneck, J. Benford, and T. S. T. Young, " Operating Characteristics of a Relativistic Magnetron with a Washer Cathode", IEEE Trans. PlasmaSci., vol. PS-15, no. 3, pp. 327–334, Jun. 1987.
58. D. Pellinen and V. Staggs, "A Technique to measure high-power electron beam currents", Rev. Sci Instrum 44, no 1, pp 46 – 49, Jan 1973.
59. R. Liu, X. Wang, X. Zou, J. Yuan, N. Zou, L. He, "Method for calibrating a Rogowski coil of fast time response", Rev. Sci Instrum 78, 084702, 2007.
60. P. N. Murgatroyd, A. K. Y. Chu, G. K. Richardson, D. West, G. A. Yearley, and A. J. Spencer, "Making Rogowski Coils", Meas. Sci. Technol. 2, pp 1218 -1219, 1991.
61. W. F. Ray and C. R. Hewson, "Practical aspects of Rogowski current transducer performance", Power Electronic Measurements Ltd, [info@pemuk.com](mailto:info@pemuk.com)
62. J. D. Ramboz, "Machinable Rogowski coil, design, and calibration," IEEE Transactions on Instrumentation and Measurement, vol. 45, no. 2, pp. 511-515, Apr, 1996.
63. D. G. Pellinen, M. S. Di Capua, S. E. Sampayan, H. Gerbacht, and M. Wang, "Rogowski coil for measuring fast, high-level pulsed currents", Rev. Sci Instrum 51, no. 11, pp 1535 – 1540, Nov. 1980.
64. G. R. Turner, "Rogowski Coils for Short Duration (<10 μs) pulsed current (>10 kA) measurements", IEEE Trans. 0-7803-5546, pp 759- 764, 1999.

65. V. Nassisi and A. Luches, "Rogowski coils: theory and experimental results", *Rev. Sci. Instrum.* Vol 50, no. 7, pp 900 – 902, July 1979.
66. K. Wong and T. Chen, "Studies of a slow wave Rogowski coil", *IEEE Trans. Plasma. Sci.* vol 18, no. 2, pp 219 – 222, Apr. 1990.
67. L. A. Bessonova, S. Y. London, and S. V. Tomashevich, "A Broad-Band Directional Coupler," *Telecommunications and Radio Engineering*, vol. 45, no. 3, pp. 23-28, Mar, 1990.
68. H. M. Cronson, "Wideband Directional Coupler for Time-Domain Measurements," *IEEE Trans., on Instrumentation and Measurement*, vol. 25, no. 1, pp. 15-17, 1976.
69. L. M. Earley, and W. P. Ballard, "New Directional-Couplers for Multimode Circular Wave-Guides Applied to Intense Pulsed Microwave Systems," *IEEE Trans., on Nuclear Science*, vol. 32, no. 5, pp. 2921-2923, 1985.
70. H. C. Early, "A Wide-Band Directional Coupler for Wave Guide," *Proceedings of the Institute of Radio Engineers*, vol. 34, no. 11, pp. 883-886, 1946.
71. Y.Y. Lau, priv. comm., NERS 673, Lecture 7, Feb 2004.
72. R. Gilgenbach, University of Michigan, (priv. comm, 2007).
73. D. de. Klerk, "The construction of high-field electromagnets", Newport Pagnell, Newport Instruments, 1965.
74. F. W. Grover, "Inductance Calculations: working formulas and tables", New York, D. Van Nostrand, 1946.